

SHIBAURA MACHINE ENGINEERING REVIEW

Mar. 2023

vol. **29**

Special Feature

Energy and
Environment



■ Introductory Note	2	Introductory Note	
■ Special Article	4	Challenge Higher Stage	
	6	Electrification of Industrial Machinery and Future Prospects	
	11	Sustainable Development Goals through CSR Activities	
■ Technical Paper	13	Controlled Degradation of Commercial Resin for Meltblown Nonwoven Fabric Sheet Production	
	26	On-Machine Measurement for Ultra-Precision Machining in the Field of Automotive Products	
	31	Three-Dimensional Observation of Graphite Structure of Thick-Walled Spheroidal Graphite Cast Iron with X-Ray CT	
	37	Application of a Surface Reforming Systems Using High-Speed Plasma Treatment to the Next Generation Printed Wiring Board Circuit Formation Process	
	42	Autonomization of Robots in the Stage of Transformation from Sustainability to Viability	
	■ Technical Report	50	Exploration of Foam Molding Technology to Improve the Functionality and Performance of Molded Products
55		Energy-Saving Measures for Die Casting Machines	
61		Approach to Implementing Digital Transformation in Twin-Screw Extruders	
67		Development of Grease Lubricated High-Speed Spindle	
71		Using Direct Cutting to Reduce Energy Usage in Cemented Carbide	
76		Efforts to Save Energy in Control Equipment Development	
81		Approach to Reduction of Environmental Impact in SCARA Robot Development	
86		Injection Molding Machine Upgradation from Induction to Energy Efficient Servo System	
■ New Product Introduction		88	Introduction of the Electric Sub-Injection Unit EC PLUS+
		90	Introduction of the DC400R2 Die Casting Machine
	93	Introduction of the High-End Model MP-2620(U), a Double-Column 5-Axis Multitasking Machine	
	95	Introduction of the High-Speed Rotating Work Spindle for High-Precision Aspheric Surface Grinders	
	97	Introduction of the TCmini Series TC11-03 Temperature Control PLC	
	98	Introduction of the Robot Controller TS5000-EMS	
	100	Shibaura Machine NC System Development History	
■ Series			
■ Column	54	Learning from Children	
	66	Experience with VR Games	
	80	Lessons Learned from Failure	
	85	Use the Five Senses! Machining Technical Support for Overseas Plants	
	92	Language Processing and Internationalization	
■ Patent News	109	Introduction to Patents	
■ Prepared Critique	113	Prepared Critique	



Shigetomo SAKAMOTO

President,
Chief Executive Officer and
Chief Operating Officer

With the publication of the 29th issue of this Engineering Review, we hope more of our stakeholders will be able to see the results of our technological developments.

We have established our “Basic Sustainability Policy” and announced our commitment to continuously realize a sustainable society and improve our corporate value. Based on that policy, this issue focuses on the theme of “Energy and Environment” and includes topics which have been attracting much attention in recent years.

In February 2020, we announced our “Management Reform Plan,” which focuses on business structural reforms, and we are currently in the process of vigorously promoting the plan on a company-wide basis. As part of this plan, we have made a major organizational change by abolishing the existing business division system and adopting a company system which allows us to rapidly respond to each market. Furthermore, we have established the R&D Center as a technology control division to ensure R&D for product development, necessary for the next generation and company-wide digital transformation strategies, is carried out in a totally optimized manner.

The R&D Center assumes the leadership and control to respond to megatrends from a global perspective.

Each of the three companies, the Metal & Plastics Industrial Machine Company, the Machine Tools Company, and the Control Systems Company, independently develops its own products, but the R&D Center is now promoting technological development based on the company-wide technology policy of “responding to the megatrends which the global manufacturing industry faces with outstanding technological innovations to both solve social issues and enhance corporate value”, thus shifting from the conventional

era of mass production and mass consumption.

In recent years, the needs of our customers have dramatically changed as the global environment has been changing: the COVID-19 pandemic changed people’s attitudes toward behavior, and Russia’s invasion of Ukraine has had a major impact on the energy and high-tech industries.

Geopolitically, the environment surrounding the manufacturing industry is also dramatically changing as social issues in developed and emerging countries become more apparent.

At the same time, global warming and environmental problems are becoming an urgent issue, and we are required to respond to the SDGs by promoting clean energy, energy conservation, reduction of environmental impact, automation, and unmanned operations. In addition, as ESG issues become more important in corporate activities, we recognize it is very important for us to develop technologies and establish a system which can appropriately respond.

This Engineering Review summarizes some of the results of the development of technologies and functions which add value to “energy and environment” in our businesses and products.

The Metal & Plastics Industrial Machinery Company reports on; the use of foam molding technology in injection molding machines for automotive and other applications to reduce weight, energy saving in die casting machines, and new products. As for extrusion molding machines, we are also strengthening our efforts in high-performance materials, and in this issue, our efforts toward digital transformation are introduced. In the area of extrusion molding machines, we are the only manufacturer in the world capable of producing a full line of separator manufacturing equipment for lithium-ion batteries, which are especially attracting attention as a

contribution to energy and the environment. We believe this will become a pillar of our business by demonstrating our competitiveness and contributing to society.

The Machine Tools Company introduces the complex large machine tools which are strong in the energy and infrastructure industries, and the reduction of energy consumption of ultra-precision machine tools capable of precision machining of optical components such as sensors and lenses, which are essential for automation and manpower saving.

In addition, in the robotics business, the focus of our Control Systems Company, approaches to and controllers for reducing environmental impact are introduced.

This issue introduces details of our technologies and products which address these social issues and provide added value to help our customers win in their respective markets through productivity, high functionality, differentiation, and so on.

We hope you will read this issue to learn about our technological evolution and our future initiatives and trust it will be helpful to you.

Challenge Higher Stage



Yukio IIMURA
Chairman

Foreword

“Keep developing technologies which satisfy potential customer needs and promoting basic research” are the words of Mr. Kametaro Fujishima, the founder of our company.

With these words, he is reproving engineers for their tendency to take the easy way out and telling them not to forget their pioneering spirit as development engineers.

Development includes different processes, such as; “R&D”, “development of fundamental technologies”, and “product development”.

The more upstream the process is, the less it contributes to immediate business results. However, upstream development processes are necessary for the future. Conducting upstream development is like navigating a vast ocean without a map, using only your pioneering spirit.

The more downstream the process is, the more directly it is linked to business results. By achieving downstream development, satisfying the customers, and contributing to an increase in company profits, downstream development can provide a source for carrying on business operations.

From a management perspective, it is very important to consider how to assign resources to each development process.

Recently, a management theory advocating “ambidexterity” has been popular. Ambidexterity refers to achieving “exploration” and “exploitation” at the same time.

“Exploration” is about creating a new business or sailing into the sea without a map.

“Exploitation” is about digging deep into existing businesses, maximizing profits, and investing in “exploration” without hesitation.

We live in an age of rapid change. To avoid game-changing events

which may adversely affect our business, executives including myself, managers, and engineers should always try to maximize the results of “exploration” × “exploitation”.

Good is good, bad is bad

It was about 37 years ago. I was working as a production design engineer in the injection molding machine engineering department and was transferred to work in the US. The mission given to me was “to be a service engineer stationed in the US”. My boss told me this is the chance for me to visit customers and feel how badly our product is designed. The experience in the US smashed my flimsy pride of being a design engineer and evoked a feeling of self-esteem as a representative of our company. I believe the experience of working in the US for about seven years had a great impact on me in the early stages of my career. I visited customers in the western part of the US to repair their machines from morning to night. Except for obvious failure, when customers reported something felt wrong with their machines, there were almost always problems with the machines. People who leave their customers saying things like “Let’s see how it works” are virtually conceding defeat. I learned that everything happening in the field is true.

There was an unforgettable event during my life in the US. A problem occurred in the screw, the most important part of an injection molding machine.

The screw, which is a shaft with a spiral groove, rotates in a cylinder wrapped with heaters called a barrel. For easy understanding, imagine a screw pump. Although the screw length in L/D varies depending on the application (18 to 28), all screws work in the same manner. The screw rotates while granular resin called pellets are injected from the base of the spiral groove and heated. The screw

moves backward as it pushes pellets forward. Due to external heating and shear heating, pellets are completely melted at the tip of the spiral groove. After the screw moves backward to the predefined position for measurement of the shot volume, the screw moves forward and injects molten resin into the mold. As resin becomes non-Newtonian fluid in the barrel, it is very difficult to design a screw which works properly.

The problem reported by a customer was abnormal wear of the screw (diameter: 100 mm). This customer used high-speed molding to produce a bucket with a lid from high-density polyethylene. In this process, measurement should be completed within eight seconds. Abnormal wear of the screw occurred within half a day from the start of the molding process, with chromium plating coming off the screw, mixing with the resin, and shining in the molded bucket. We pulled out the screw from the barrel, tentatively repaired damage on the screw in millimeters, honed the inside of the barrel with a simple honing machine, and then inserted the screw back into the barrel to resume production. However, the problem occurred again and we had to repeat the same repair procedure. We worked around the clock and the customer was still not satisfied.

We reported the problem to headquarters in Japan, but they only gave us useless advice such as "Check if the screw shaft is centered" or "Raise the temperature". We determined wear in the screw was caused by abnormal lateral pressure and reported the necessity of improving the melting process. Prototype screws shipped from Japan by air arrived one after another, but with just one look at them, I knew by intuition they are not good. The result was as I imagined. It was like treating the symptoms instead of the cause. Although two of my superiors in Japan came to the US in turn, neither of them were able to propose any solution and went back to Japan saying things like "Let's see how it works".

I consulted with my boss in the US and we decided to develop a dedicated screw in collaboration with a screw manufacturer in the US. We agreed to manufacture a prototype screw by physically separating the solid layer from the liquid layer at a long distance to improve melting efficiency.

Upon seeing the completed prototype screw, I knew it was good. With this screw, the problem disappeared like magic. It was the moment when a screw with high plasticating capacities for high-density polyethylene was born. This experience made me realize the awesome potential of development and design.

After returning from the US, I put a piece of quartz glass at five locations over the barrel for the same 100-mm screw and used a high-speed camera to observe the difference in the melting process between the screw manufactured in the US and the old screw. There was an obvious difference in the melting process between them.

While "breakup", in which large pieces of unmelted resin float in melted resin, occurred with the old screw, the melting process was extremely improved with the screw manufactured in the US, with no abnormal lateral pressure generated.

These techniques and findings were not new to our company. They were broadly recognized in the extrusion molding machine division located next to the injection molding machine division.

Fellow engineers, let's ensure you are not a big fish in a small pond. Let's not forget to discuss problems with others and make certain your goal is not set too low.

Let's set a higher goal and aim to achieve it!

Michelangelo's words:

"The greatest danger for most of us is not that our aim is too high and we miss it, but that it is too low and we reach it."

Electrification of Industrial Machinery and Future Prospects



Jun KOIKE

Senior Managing Executive Officer

1 Introduction

In the summer of 2022, the world experienced extreme heat, forest fires, flood damage, and droughts which killed many people. Although this was viewed as abnormal weather caused by global warming, this is now being considered as the normal state of affairs. Thus, efforts for the reduction of CO₂ emissions and decarbonization as a countermeasure against global warming have become a top priority for all mankind.

Under these circumstances, the automotive industry is switching from internal combustion engines to electric vehicles at an accelerating pace. The automotive industry is undergoing a once-in-a-century revolution as indicated by CASE (Connected, Autonomous, Shared and Electric). As batteries evolve and problems of range and service life are overcome, the E (Electric) segment of this revolution is expanding into a market which advocates zero emissions. Although there is now a move back to thermal power generation due to energy supply problems caused by the Ukraine conflict, the electrification of mobility is expected to expand along with the spread of power generation which will drive renewable energy in the future.

Shibaura Machine manufactures industrial machines such as machine tools, injection molding machines, die-casting machines, and extrusion molding machines. Since these industrial machines are not movable like automobiles, they have been powered by electricity. However, injection molding machines and die-casting machines require large loads for mold clamping and injection forces, so hydraulic pressure has been traditionally used as the control transmission medium, resulting in large losses in terms of efficiency and adversely affecting power consumption.

On the other hand, machine tools have shifted to numerical control (NC) to improve control accuracy. In 1977, we took over the NC business from Toshiba Corporation, and have been refining our servo control technology in-house since then. Through the accumulation of these efforts, we have established, together with the controller development, servo motors and servo drive systems as our core technology in terms of both their hardware and software, and are continuing development to achieve ever higher precision.

Under such circumstances, the electrification of injection molding machines progressed in the 1990s, due to the increase in the size of servo motors and the evolution of linear motion components such as ball screws. This hydraulic-to-electric shift began with small-sized injection molding machines, not only because of reduced power consumption, but also because of the advantages of better reproducibility of molding conditions. However, all-electric injection molding machines at that time were regarded as underpowered, and there were many cases where thick-walled products which required prolonged pressure holding could not be molded. Realistically, it was difficult for such machines to simultaneously achieve their maximum specification speed and maximum specification pressure in the injection process. We recognized this issue and now provide all-electric injection molding machines which can simultaneously achieve their maximum speed and maximum pressure by optimizing the servo motor design according to the specifications and the servo control to increase torque in the high-speed range.

Since then, we have developed a series of all-electric injection molding machines with mold clamping forces up to 2,500 tons. While overseas manufacturers are offering inexpensive hydraulic injection molding machines, in recent years there has been an

increase in demand for all-electric injection molding machines up to the ultra-large range from users who are working on decarbonization. In addition, we are also developing environmentally friendly die-casting machines for casting aluminum parts for engines and other components. This paper introduces the effects and prospects for the environmental friendliness of injection molding and die-casting machines up to the ultra-large range, with “electrification” as the key word.

2 Energy-saving performance of all-electric injection molding machines

Injection molding machines can be classified into three types: the long-established “hydraulic type”; the “hydraulic servo type”, which replaces the three-phase induction motor used by “hydraulic type” as its drive source with a servomotor; and the “all-electric type”, in which all drive actuators are entirely electrically driven. In the case of the hydraulic type, the efficiency depends on the three-phase induction motor and hydraulic pump, and there are pressure losses in the piping and losses in the hydraulic circuit due to the use of hydraulic valves and other components. In the case of the “hydraulic servo type”, which uses the servomotor as the drive source, the hydraulic pump is allowed to stop or slow down when it is not working, resulting in a reduction of losses. In contrast, in the case of the “all-electric type,” the servomotor, bearings, and ball screw, which constitute the drive mechanism, are highly efficient, enabling a significant reduction in power consumption.

Figure 1 compares the power consumption of hydraulic and all-electric types from small to ultra-large machines. Figure 2 compares the power consumption at a clamping force of 1300 tons between the two plus the hydraulic servo type.

Although power consumption to some extent depends on

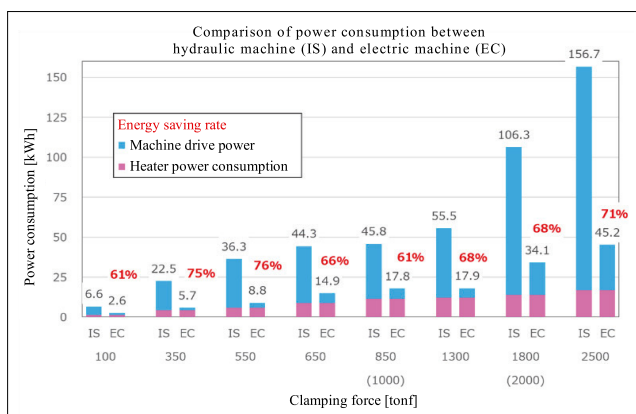


Fig. 1 Comparison of power consumption between hydraulic and all-electric types

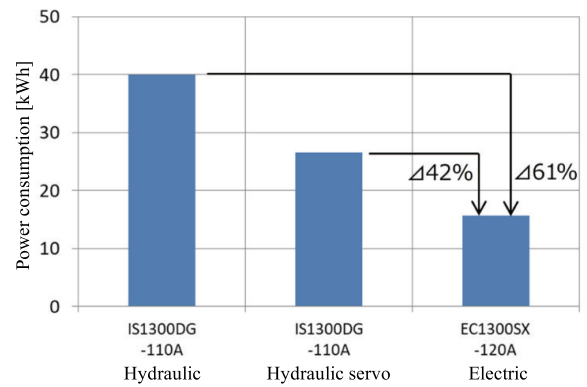


Fig. 2 Comparison of power consumption between three drive types

molding conditions, the power consumption of the all-electric type is about 60% to 70% lower compared to that of the hydraulic type, and about 40% lower compared to that of the hydraulic servo type as shown in these figures. In addition, the all-electric type eliminates the need for hydraulic oil and cooling water (for cooling the hydraulic oil), and also reduces the load on the factory’s air conditioning system.

By converting the reduction in power consumption at a clamping force of 1300 tons into CO₂, the replacement of the hydraulic type with the electric type results in a reduction of 69.1 tons of CO₂ per year (Figure 3).

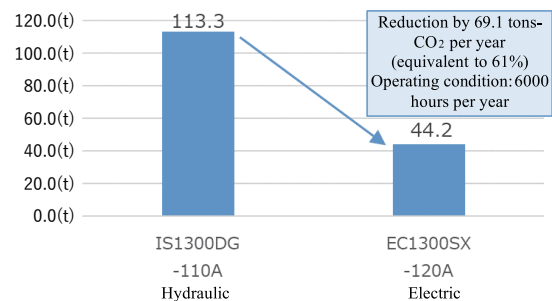


Fig. 3 Comparison of annual CO₂ emissions [tons-CO₂/year]

*Calculated assuming 1 kWh of power consumption generates 0.472 kg of CO₂.

3 Controllability of all-electric injection molding machine

The word “servomotor” is said to have originally come from the word “servant”. The all-electric type does its job faithfully to commands and has the advantages of its high control accuracy and repeatability in addition to lower power consumption (Figure 4). In the case of the hydraulic type, changes in viscosity due to changes in oil temperature, leaks of hydraulic oil, and compressibility of the hydraulic oil cause fluctuations in operation.

	Hydraulic type	Electric type
Distribution rate (%)	0.1430	0.1051
Standard deviation	0.0119	0.0092

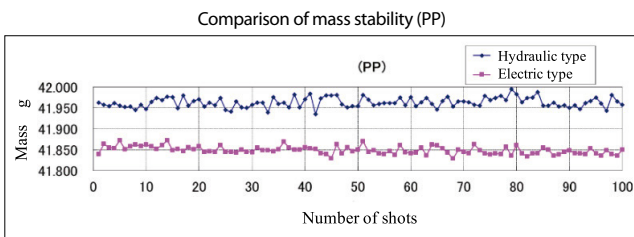


Fig. 4 Comparison of molded product weight variation between hydraulic and all-electric types

In addition, the state-of-the-art controller INJECTVISOR-V70, taking advantage of its controllability, is equipped with a variety of special controls which enable stable production of high value-added molded products.

Classification	Control name	Purpose
Injection	NATURAL PACK	Low-pressure, fixed-quantity filling eliminates burrs, shorts, and product variation
	PRESTROL	Stabilization of filling volume by uniform resin density and precise filling resin volume
	DST-Fill	Molding quality is maintained by detecting resin changes due to lot differences and automatically changing molding conditions
Mold clamping	PRESTROL	Reduces internal stress in molded products through precision compression control with multi-step control of mold clamping force
	PRECISION CORE BACK	Realizes high quality/stability of foam molding and high foam magnification by precise coreback operation which slightly opens the mold after injection filling

Table 1. Example of INJECTVISOR-V70 molding control

4 Electrification of die casting machines

In the 2000s, the all-electric type was also developed for die casting machines. However, the all-electric type die casting machines have not been valued nor widely used. Die casting machines which mold aluminum, a molten material which quickly solidifies, are required to inject molten aluminum instantaneously into the mold. Therefore, it must be able to handle injection speeds of 7 to 10 m/s, about 50 times that of an injection molding machine, and the acceleration to reach its maximum speed in a few milliseconds is required. It is difficult to achieve this instantaneous force with an electric system, in terms of both technology and cost. Therefore, hydraulic accumulators are used to drive the injection system.

In recent years, with the aim of improving productivity and reducing power consumption of die-casting machines, we have developed a lineup of electric clamping die-casting machines with the electric die open/close mechanism, ranging from small to ultra-large sizes. Their features are high-cycle, space-saving, and maintenance-saving. The electric clamping system realizes high-

acceleration operation without shocks due to its good controllability. The good reproducibility also makes it possible to set conditions to the limit and minimize the low-speed range, leading to shorter cycle time (Figure 5).

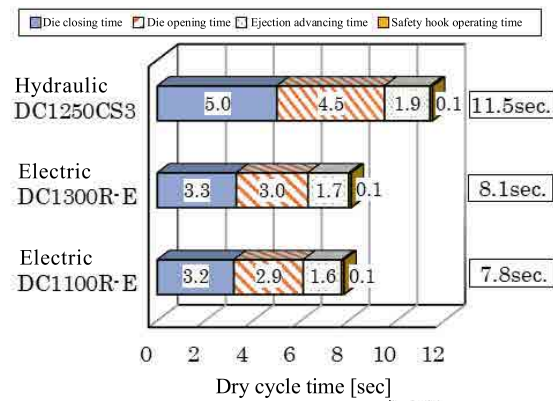


Fig. 5 DC1100/1300R-E dry cycle time

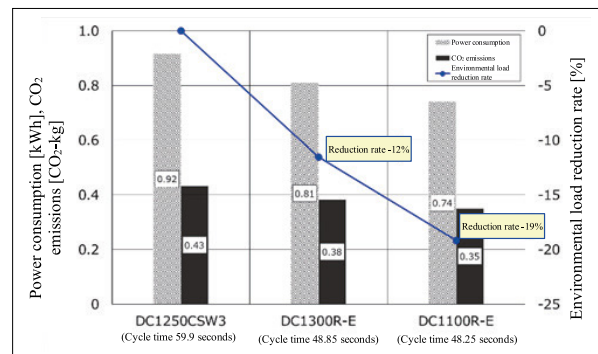


Fig. 6 Power consumption and CO₂ emissions per cycle

*Calculated assuming that 1 kWh of power consumption generates 0.472 kg of CO₂.

Figure 6 shows the reduction in power consumption and CO₂ emissions with electric clamping units at a clamping force of 1300 tons compared to the hydraulic clamping unit. The ladling time is 6 seconds, the spray time is 18 seconds, the product take-out time is 5 seconds, the extrusion stroke is 100 mm, and the die timer setting is 10 seconds. The electric clamping unit enables die opening/closing operation and core operation in an overlapping manner, thereby shortening the cycle time. As a result of estimation, the DC1300R-E and DC1100R-E are expected to reduce environmental impact per cycle by approximately 12% and 19%, respectively, compared to conventional hydraulic toggle machines.

As part of the electrification of die-casting machines, we are currently developing hybrid core devices and hybrid extrusion devices which primarily use electric power and only employ hydraulic power during mold release, which requires more power. With these devices, which enable further higher-cycle operation and reduction of hydraulic oil consumption, we will provide

environmentally friendly die-casting machines with excellent productivity.

5 Future prospect - providing new value

In recent years, efforts to address the SDGs have become a common theme throughout the world. We, as a manufacturer of industrial machines, will work on environment-friendly technologies and anti-overwork high-productivity technologies, such as automation and systemization for energy-savings, defect rate reduction, productivity improvement, and substitution of overloaded labor, to contribute to the SDGs. The approach to these challenges has become even more important due to recent labor shortages.

As above described, the electrification of industrial machines has effectively contributed to productivity improvement and CO₂ reduction through energy-savings, maintenance reduction, and high-cycle operation. In the future, the use of IoT and AI technologies is expected to further advance this trend. One of the technologies which can create new added value to increase productivity in the future is digital transformation which makes use of various data, and in Europe efforts toward INDUSTRY 4.0 are gaining momentum.

We have four policies regarding IoT objectives:

- (1) production improvement to compensate for human resource shortages through automation and intelligence,
- (2) prevention of sudden machine stoppages through predictive maintenance and planned maintenance,
- (3) quality improvement/stabilization through AI utilization for analysis and reflection of its results, and
- (4) dealing with dispersed production sites through centralized management and monitoring.

The electrification of industrial machines will particularly benefit the automation and intelligence in (1), the predictive maintenance in (2), and the AI utilization in (3). These are the equivalent of C (Connected) and A (Autonomous) of the CASE of the automotive industry. Electrification allows for precise machine operation faithful to commands, high precision, and visualization of operating conditions such as torque and speed.

- (1) Production improvement to compensate for human resource shortages

In recent years, there have been few applicants to engage in dirty,

dangerous, and demanding jobs. In addition, reducing fixed costs and increasing productivity are important issues for machine users. Therefore, in addition to the automation of individual machines such as injection molding machines and die-casting machines, batch management of the processes before and after is also required. We focus on system engineering for this purpose.

As an example, Figure 7 shows a stamping system for composite materials, which has recently been attracting attention for automotive weight reduction.

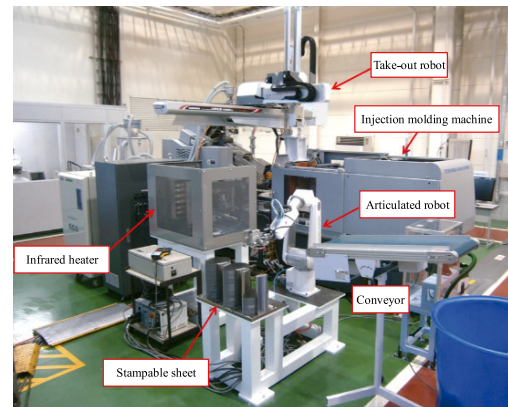


Fig. 7 GFRP sheet stamping system

There are great advantages to electrification in a series of motion control, accurate condition monitoring, and so on.

- (2) Prevention of sudden machine stoppages through predictive maintenance and planned maintenance

When an automated system is employed, a sudden breakdown somewhere in the line will cause the entire line to stop. In the current trend of reducing inventory, line stoppages are fatal accidents. Therefore, predictive maintenance is important to prevent machine stoppages.

It is easier to grasp changes in machine operating conditions of electric-type injection molding machines than those of conventional hydraulic-type machines. For example, an increase in sliding friction due to the surface stripping of a ball screw or bearing will appear as a change in servo motor torque. In addition, the accumulated load on a servo power supply or servo amplifier can also be detected from the voltage and current. This information is useful for predicting the service life of electrical components. In other words, by continuously detecting the state of the servo motor, it is possible to detect changes in the state of the ball screw and the life of the servo amplifier. By recognizing such changes are signs a part is about to break, and proactively replacing it with a spare part, it is possible to prevent sudden accidents. By identifying necessary contingencies,

such as setting thresholds for changes during mass production and utilizing data from sensors installed around the machine (vibration sensor, temperature sensor, AE sensor, etc.), we will establish predictive maintenance for the system as a whole.

(3) Quality improvement/stabilization through AI utilization for analysis and reflection of its results

Machine users are aiming for zero-defect production. For both injection molding machines and die-casting machines, a wide variety of quality data has been recorded, but it was difficult to capture correlations between good product conditions and multiple data sets. However, with the evolution of AI and other analysis technologies, it is now possible to determine which combination of data has the highest percentage of good products among the various combinations of data from the quality data of good product production. The future goal is autonomous control, in which the machine itself corrects the molding conditions to produce the best possible products. To achieve this, it will be necessary to link the quality data for each shot with the output good/defect result. To this end, automatic inspection technology, which leads to manpower saving, as mentioned in (1) above, will also play an important role. We would like to realize autonomous control of machines through analysis of good product data, thereby contributing to the achievement of zero-defect for users. The DST-Fill (Dynamic Self-Tuning) control (Table 1) which we employ in our injection molding machines is one of the molding condition compensation approaches. We believe electrification will become an increasingly important factor for the accuracy of quality data and the linkage of automation technology.

6 Conclusion

In various fields, notably in the automotive industry, electrification occupies an important position in current efforts for decarbonization and contribution to the SDGs set forth by the United Nations. In the industrial machine field, electrification has been long promoted, not only from the viewpoint of energy-saving, but also as an important factor in improving productivity. Electrification is expected to evolve further in the future as it is integrated with digital transformation. We will accelerate the development of electrification, recognizing it will contribute to users and the global environment.

Sustainable Development Goals through CSR Activities



B. Ramesh

Head - Human Resource & Administration
SHIBAURA MACHINE INDIA PRIVATE LIMITED

Shibaura Machine India(SMI) is a frontrunner to cater to the Sustainable Development Goals through its Corporate Social Responsibility (CSR) activities.

Under the CSR rules mandated by The Companies Act, 2013, SMI has constructed class rooms in nearby government schools and water tank for Chembarambakkam Village. As per rule, CSR amount can also be deposited in Prime Minister/Chief Minister Relief fund. Instead SMI took the option of spending on social developments allowed as per the rule.

The classroom construction process begins with receipt of approval request from the School Head Master along with Parents Teacher's Association's request. SMI then proceeds with obtaining approvals from all relevant Government authorities and the construction of classrooms begins through an authorized contractor.



Classroom building at Chembarambakkam



Classroom building at Nanganallur

The construction process is monitored regularly and the fully constructed classroom is handed over to the school management. By this, SMI has achieved SDG Goal No.2 – Quality Education & Goal No.9 – Industry, Innovation & Infrastructure.

A water tank of capacity 60,000 litres was constructed by SMI at Chembarambakkam village which is towards achieving the SDG goal 6 – Clean water & sanitation. About 100 families are being benefited.



Water Tank inauguration at Chembarambakkam



Food packets distribution for poor & needy people

In addition to the CSR activities, SMI is also serving 50 packets of food prepared for employees to the needy people in the nearby areas for the past 145 days, which is aimed towards SDG Goal 2 – Zero hunger.

Shibaura Machine BTP (Basic Training Provider) :-Our endeavour

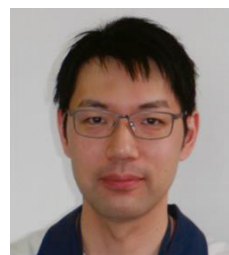


BTP was established in 2014 after obtaining permission from Government to help the down trodden students in the society who cannot pursue higher education because of their poor family background. After 1 year of class room training and 1 year of on job training, students have to write an exam conducted by central

government. Once qualified, they are given Certificate from government and are employable as machinist or fitter. As on date about 100 students trained in the trade machinist and fitter. From this year onwards fitter trade is being changed to Injection Moulding Machine operator trade. This would help customer to employ them in their workshop. SMI plan to absorb some of the machinist trade students after passing the examination, to operate high precision Machining centre.

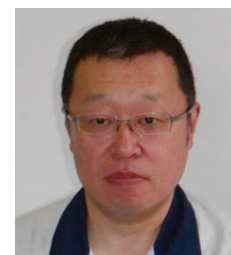
Controlled Degradation of Commercial Resin for Meltblown Nonwoven Fabric Sheet Production

This article was reprinted from the academic paper, *Polymers* 2021, 13 (22), 3892. Manufacturing meltblown nonwoven fabrics requires special grades of resin with very low viscosity, which are not dealt with so much on market and cost quite high compared to the standard grades. We propose a high-shear rate processing method that can quickly and easily produce such low-viscosity resin from the commercial one without using organic peroxides. In this method, we apply high-shear stress to molten resin by using a high-shear extruder, which is a single screw extruder with high screw rotation speed, and the resin is thermally decomposed of its shear-induced heat which is quickly generated. We found that polypropylene with a value of melt flow rate over a thousand, which was required for the meltblown process, was produced from the standard grade with the high-shear extruder at the screw rotation speed of 3600 min^{-1} and the barrel temperature over 300°C . Using the degraded polypropylene, a meltblown nonwoven fabric sheet was successfully fabricated. We also developed a numerical simulator of the high-shear extruder which can handle a wide range of the screw rotation speed and barrel temperature by the Nusselt number modulated with the operational conditions. The experimental values of the zero-shear viscosity and temperature at the exit of the extruder agreed well with the simulation results. Our high-shear rate processing method will enable us to quickly and easily produce various meltblown nonwoven fabric sheets at low costs.



Yuya SASAI

Metal & Plastics Industrial Machine Company,
Extrusion Machine Engineering Department



Yoshio IIZUKA

Metal & Plastics Industrial Machine Company,
Extrusion Machine Engineering Department



Kaho OSADA

Metal & Plastics Industrial Machine Company,
Extrusion Machine Engineering Department

collective writing :

Kentaro TAKI

School of Mechanical Engineering,
Kanazawa University

1 Introduction

Meltblown nonwoven fabrics are widely used as filtration media, medical fabrics, sound-absorbing and cushioning materials, and so on. Fine fibers are produced by pumping molten resin through a die with tiny holes whose size is of the order of 0.1 mm, thus low viscosity grades of resin with quite a high value of melt flow rate (MFR) are chosen as the raw materials [1]. For polypropylene (PP), the value of MFR around a thousand is required for the meltblown process. For example, low-viscosity PP with MFR of 1550 g/10 min at 230°C was used for investigating unstable behavior of melt-blowing process [2]. However, such special grades of resin are not dealt with so much on market and they cost quite high compared to the standard grades. It could be useful and economical that those special grades of resin are controllably produced from the commercial ones which are always available anywhere at low costs.

One of the methods, which is well known, is to degrade resin by using organic peroxides. In this method, a resin and an organic peroxide are compounded by a twin-screw extruder and the peroxide radicals chemically decompose the polymers during the mixing process. Numerical simulation of the peroxide-induced degradation was also developed so far. The molecular weight loss and change in viscosity of PP in a modular self-wiping corotating twin-screw extruder was studied by coupling a global one-dimensional flow model of the twin-screw extrusion process with kinetic equations of the evolution of molecular mass in the peroxide-induced degradation of PP [3]. To evaluate the viscosity reduction, the relationship between the molecular weight and the rheological parameters, which were given in [4], were used. However, it is generally hard to treat such highly reactive additives and to control the degradation. The molecular weight distribution of PP during the peroxide-induced degradation in a continuous stirred tank reactor

was calculated and it was argued that imperfect mixing of the peroxide with PP could lead to a broadening of the molecular weight distribution [5]. The broadening of the molecular weight distribution was explained by spatially inhomogeneous degradation which occurred around the peroxide particles because of the fast dissociation reaction and relatively slow diffusion of the peroxide [6]. Recent developments of the modeling of the reactive extrusion were summarized in [7]. In addition, due to residues that are caused by the decomposition with peroxides, the degraded resins by this method are not suitable for medical and hygiene products. Moreover, organic peroxides are specified as hazardous materials which must be carefully treated and stored.

Here, we propose another method without using peroxides, which we call a high-shear rate processing method. To date, the high-shear rate processing was mainly applied to the compounding of immiscible polymers and the dispersion of inorganic fillers in a polymer matrix. A high-shear processed poly(vinylidene fluoride) (PVDF)/polyamide11 (PA11) blend was studied and it was shown that PA11 could be dispersed in the PVDF phase with a domain size of several tens of nanometers by using a high-shear extruder [8]. The rotational speed of the extruder was 1200 min^{-1} . Unmodified multiwalled carbon nanotubes (CNT) were compounded with poly(styrene-*b*-butadiene-*co*-butylene-*b*-styrene) (SBBS) using a high-shear extruder and the dispersion of CNTs was greatly improved upon increasing the exerted shear rate and a homogeneous dispersion was successfully achieved with the screw rotation speed of 2000 min^{-1} [9]. The structures and properties of polycarbonate (PC)/poly(methyl methacrylate) (PMMA) blends fabricated using their high-shear extruder were investigated and it was shown that nanostructured PC/PMMA blends with high transparency and improved mechanical properties were obtained at the screw rotation speed of 2250 min^{-1} [10]. On the other hand, a reduction of mechanical properties of compounds with the high-shear rate processing was also reported. The effect of high-shear rate processing on the compatibilization of high impact PP/ethylene propylene rubber/high density polyethylene (PP/EPR)/PE blends was investigated by using a co-rotating twin-screw high shear extruder and a decrease of the size of PE core encapsulated by EPR shell was observed when increasing the screw rotation speed from 300 to 600 min^{-1} [11]. However, as the screw speed was increased to 800 min^{-1} and 1200 min^{-1} , a noticeable reduction of the mechanical properties of (PP/EPR)/PE blends was found due to the thermal

degradation. Polyamide 6(PA6)/PP blends were produced by a high-shear rotational processing machine and PA6/PP alloy fabricated under the screw rotation speed of 3000 min^{-1} with a mixing time of 30 s showed considerably lower breaking strain and yield strength than that of neat PA6, which was caused by the reduction of the molecular weight due to the high-shear rotation [12].

In this paper, we positively use the ability of the degradation with the high-shear rate processing to fabricate the low-viscosity polymers without using peroxides. Our high-shear extruder is a type of single screw extruder with a maximum rotational speed of 3600 min^{-1} . Similar to a twin-screw extruder, the screw is composed of multiple screw elements so that we can realize different screw configurations. We apply high-shear stress to molten resin by using a single screw extruder with high screw rotation speed. The molten resin is thermally decomposed of its own shear-induced heat. Of course, we could decompose resin only by heat conduction from the barrel with high temperature, but it costs much time to heat or cool the barrels. Furthermore, there is usually an upper limit of barrel temperature which is not so high. Our method utilizes the shear-induced heat which is quickly generated in the bulk of resin and makes the resin at a higher temperature than the barrel temperature. In addition, as the major operating condition to adjust the degradation is only the screw rotational speed, different grades of resin are quickly and easily available. With the screw rotational speed of 3600 min^{-1} and the barrel temperature over 300°C , we have produced low-viscosity PP with a value of MFR over a thousand from standard grades of PP which are commercially available. The meltblown nonwoven fabric sheet which is made of the degraded PP has been also produced. To our best knowledge, this is the first example to fabricate the low-viscosity PP for the meltblown process with the high-shear rate processing without using any peroxides.

We have also developed a numerical simulator which can predict the zero-shear viscosity of the degraded resin during the high-shear rate processing. The simulation of thermal degradation in a modular corotating twin-screw extruder was firstly developed in [13]. They calculated the molecular weight loss of PP along the screw axis by coupling a two dimensional flow model with the kinetic equations of the thermal degradation. Since the maximum screw rotation speed of their study was 300 min^{-1} , the effect of the shear-induced heat was considered to be small. Thermal and mechanical degradation of polystyrene in an ultra-high speed twin-screw extruder and the predictions of the molecular weight loss

were studied [14]. However, the viscosity reduction due to the molecular weight loss during the extrusion process and the back reactions to the physical quantities such as pressure and temperature were not considered. In our simulation, we used the simplest kinetic equation of the viscosity reduction and coupled it with a one dimensional non-Newtonian flow model in a single screw extruder. Our kinetic model of viscosity reduction could be easily derived by assuming that a resin was composed of linear polymers and thermal decomposition of polymers followed the random scission process. The model took the similar form to the kinetic equation of MFR described in [15], however we determined the order of reaction of the kinetic equation for the zero-shear viscosity theoretically. Residence time distributions (RTD) of PP in a high-shear twin-screw extruder was measured by an on-line UV fluorescence device, and they found that deviations between the experimental results and the simulation results of RTD were observed at a high screw speed more than 800 min⁻¹ and a small flow rate less than 4 kg/h [16]. They also found that at a high screw speed of 1200 min⁻¹ and a barrel temperature of 200°C, the calculated exit temperature overestimated the experimental result by around 30°C. They concluded that this difference occurred because the dependence of the heat transfer coefficient on the screw speed was not treated and the resin was not cooled by the barrel in the simulation [16]. Therefore, we decided to evaluate the global Nusselt number by solving a one dimensional transient heat conduction equation in the case of the simple shear flow. The calculated Nusselt number was dependent on the operational conditions such as the screw rotation speed and the barrel temperature. We found that our simulation results agreed well with the experimental results for the degradation using the high-shear extruder. To our best knowledge, no one simulates and investigates the viscosity reduction in the high-shear extruder over the screw rotation speed of 2000 min⁻¹.

2 Introduction

2.1 Flow in a Single Screw Extruder

We review a one dimensional non-Newtonian fluid flow model in a single screw extruder. We assume that the flow is steady-state and fully developed. Since the ratio of inner diameter to outer diameter of screw is close to one, the channel curvature of the screw is negligible. The SI units are implicitly assumed in this section. The nomenclature and the definition of symbols are summarized in the Appendix A.

2.1.1 Screw

Fig. 1 shows an unwound geometry of a single screw extruder. The screw is modeled by a rectangular channel with a height H and a width W , and the barrel is modeled by a moving flat plate covering the screw channel. The velocity of the plate is $V = \pi DN$, where D is the inner diameter of the barrel and N is the screw rotational speed.

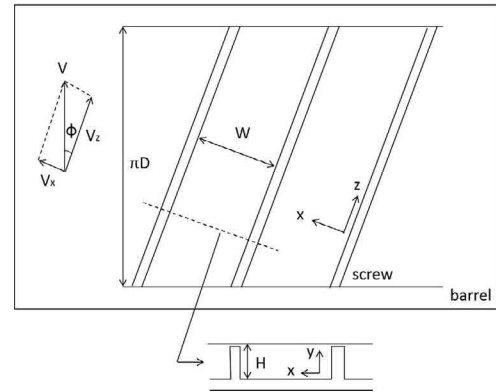


Fig. 1 Geometry of unwound screw and barrel in screw extruder.

We only consider one dimensional flow in the down-channel direction z . In the case of shallow and wide channels, the velocity component of fluid v^z can be approximated as a function only of the channel depth direction y . Then, the equation of continuity becomes trivial.

The equation of motion is

$$\frac{\partial}{\partial y} \left(\eta \frac{\partial v^z}{\partial y} \right) = \frac{\partial p}{\partial z}, \quad (1)$$

where p is the pressure and η is the viscosity of the fluid. The boundary conditions are

$$v^z|_{y=0} = 0, \quad v^z|_{y=H} = V \cos \phi \equiv V^z, \quad (2)$$

where ϕ is the screw angle. When the fluid is fully filled in the screw, the pressure gradient has a finite value, which we denote by α . Since the fluid velocity v^z is a function of the pressure gradient, α is determined by the equality for the flow rate,

$$Q = W \int_0^H dy v^z(\alpha). \quad (3)$$

When the fluid is partially filled in the screw, the pressure gradient vanishes. Thus, from Eq.(1), the flow in the partially filled region is represented by the simple shear flow with

$$v^z = V^z y / H. \quad (4)$$

The fill ratio is defined by

$$f = \frac{Q}{W \int_0^H dy v^z}. \quad (5)$$

The viscosity of molten resin is generically a function of shear rate $\dot{\gamma} = |\partial v^z / \partial y|$. In this paper, we adopt the Cross model:

$$\eta = \frac{\eta_0}{1 + (\eta_0 \dot{\gamma} / \tau_*)^{1-n}}, \quad (6)$$

where η_0 , τ_* , and n are the model parameters. In the case of non-

isothermal problems, the zero-shear viscosity η_0 depends on the temperature T . We assume that η_0 follows the Arrhenius law:

$$\eta_0 = \eta_r \exp\left(T_* \left(\frac{1}{T} - \frac{1}{T_r}\right)\right), \quad (7)$$

where T_* is the model parameter and η_r is the zero-shear viscosity at the reference temperature T_r .

The energy equation is

$$\rho C_p v^z \frac{\partial T}{\partial z} = -\frac{\partial q}{\partial y} + \eta \dot{\gamma}^2, \quad (8)$$

where ρ , C_p are the melt density and the heat capacity of the fluid, respectively, and

$$q = -\kappa \frac{\partial T}{\partial y}, \quad (9)$$

is the heat flux, where κ is the thermal conductivity of the fluid. The initial condition is

$$T|_{z=0} = T_i, \quad (10)$$

where T_i is the initial temperature. The boundary conditions are

$$q|_{y=0} = 0, \quad (11)$$

$$T|_{y=H} = T_b, \quad (12)$$

where T_b is the barrel temperature.

Integrating the energy equation over y by part and using Eq.(1), we obtain

$$\rho C_p Q \frac{\partial T}{\partial z} = -fWq|_{y=H} + fWV^z \tau|_{y=H} - Q \frac{\partial p}{\partial z}, \quad (13)$$

where $\tau = \eta \partial v^z / \partial y$ is the shear stress. Strictly speaking, the temperature in Eq.(13) is the average temperature which is defined by

$$\bar{T} = \frac{\int_0^H dy v^z T}{\int_0^H dy v^z}, \quad (14)$$

as described in [17]. The second and last terms of the right hand side in Eq.(13) come from the shear-induced heat generation. The first term of the right hand side in Eq.(13) represents the heat conduction of the fluid to the barrel and usually modeled in one dimensional problems by

$$q|_{y=H} = \frac{\kappa Nu}{2H} (T - T_b), \quad (15)$$

where Nu is the Nusselt number.

In the experiments of the high-shear rate processing, the screw rotational speed and the barrel temperature are chosen in a wide range of values. Thus, we can not set the Nusselt number as a constant value in all experiments. To estimate the Nusselt number for each experiment, we numerically solve the energy equation Eq.(8) with the boundary conditions Eqs.(11) and (12) in the case of the simple shear flow with a homogeneous initial temperature Eq.(10), and the distributions of temperature and heat current in the y and z directions are calculated. Then, the local Nusselt number [17]

is obtained by

$$Nu_z = \frac{2Hq(z)|_{y=H}}{\kappa(\bar{T}(z) - T_b)}. \quad (16)$$

In our simulation, we use the average Nusselt number,

$$Nu = \frac{1}{L_p} \int_0^{L_p} dz Nu_z, \quad (17)$$

where L_p is the path length of the screw.

2.1.2 | Die

In our experiments, a circular die was used. The equation of motion is

$$\frac{1}{r} \frac{\partial}{\partial r} \left(r \eta \frac{\partial v^z}{\partial r} \right) = \frac{\partial p}{\partial z}, \quad (18)$$

where r , z are the radial and axial coordinates, respectively. The boundary conditions are

$$\frac{\partial v^z}{\partial r} \Big|_{r=0} = 0, \quad v^z \Big|_{r=R} = 0, \quad (19)$$

where R is the radius of the die. As in the previous subsection, the pressure gradient $\partial p / \partial z \equiv \alpha$ is determined by the equality for the flow rate,

$$Q = 2\pi \int_0^R dr (rv^z(\alpha)). \quad (20)$$

The energy equation is

$$\rho C_p Q \frac{\partial T}{\partial z} = -2\pi R q|_{r=R} - Q \frac{\partial p}{\partial z}, \quad (21)$$

where

$$q|_{r=R} = \frac{\kappa Nu}{2R} (T - T_w), \quad (22)$$

is the heat flux at the wall of cylinder and T_w is the temperature of the die. For the Nusselt number, we use the average Nusselt number for the case of power-law fluid,

$$Nu = 1.615 \left(\frac{(3+1/n)\rho C_p Q}{\pi \kappa l} \right)^{1/3}, \quad (23)$$

where l is the length of the die.

2.2 | Model of Viscosity Reduction

For a large rotational speed and a high barrel temperature, shear heating and heat conduction become so large that polymers are thermally decomposed. Although the complete kinetic equations of the thermal decomposition of polymers were described in [13], here we consider the simplest model. We assume that a resin is composed of linear polymers and thermal decomposition of polymers follows the random scission process.

A polymer is modeled by a long chain with \mathcal{N} number of nodes, which represent the backbone carbon atoms [18]. The number of polymers with \mathcal{N} number of nodes is denoted by $n_{\mathcal{N}}$. Then, the number of all bonds in the polymers is given by $\sum_{\mathcal{N}=1}^{\infty} (\mathcal{N}-1)n_{\mathcal{N}}$. If breaks of the bonds follow the first order reaction with a reaction rate k and the repolymerization does not occur, we find

$$\frac{d}{dt} \left(\sum_{\mathcal{N}=1}^{\infty} (\mathcal{N}-1)n_{\mathcal{N}} \right) = -k \sum_{\mathcal{N}=1}^{\infty} (\mathcal{N}-1)n_{\mathcal{N}} \quad (24)$$

where t is time. The reaction rate follows the Arrhenius law,

$$k \approx Ae^{-\frac{E}{R_g T}}, \quad (25)$$

where A is the frequency factor, E is the activation energy, and R_g is the gas constant. The number of all nodes in the resin, $\sum_{\mathcal{N}=1}^{\infty} \mathcal{N} \bar{n}_{\mathcal{N}}$, does not change in time if the amount of evaporation of polymers is neglected. Since the number average degree of polymerization is defined by

$$\bar{\mathcal{N}} = \frac{\sum_{\mathcal{N}=1}^{\infty} \mathcal{N} \bar{n}_{\mathcal{N}}}{\sum_{\mathcal{N}=1}^{\infty} \bar{n}_{\mathcal{N}}}, \quad (26)$$

we obtain

$$\frac{d}{dt} \left(\frac{1}{\bar{\mathcal{N}}} \right) = k \left(1 - \frac{1}{\bar{\mathcal{N}}} \right), \quad (27)$$

which was described in [19]. For large $\bar{\mathcal{N}}$, this formula becomes

$$\frac{d\bar{\mathcal{N}}}{dt} = -k\bar{\mathcal{N}}^2. \quad (28)$$

Since the zero-shear viscosity is empirically proportional to $\bar{\mathcal{N}}^{3.4}$, we find

$$\frac{d\eta_r}{dt} \approx -k\eta_r^{1.3}, \quad (29)$$

where the proportionality was absorbed into A .

In [15], a semi-empirical kinetic model of the peroxide-induced degradation for a value of MFR,

$$\frac{d[MFR]}{dt} = K[MFR]^a,$$

was introduced, where K is the reaction constant and a is the order of reaction. This expression is essentially the same as Eq.(29) because the MFR is proportional to some power of the zero-shear viscosity. However, we estimated the order of reaction from $\eta_r \propto \bar{\mathcal{N}}^{3.4}$ without experiments. As a result, the model parameters for the viscosity reduction were reduced.

The time derivative is replaced by the material derivative, thus in the steady-state case, we find

$$\frac{\partial \eta_r}{\partial z} = -\frac{fSk}{Q} \eta_r^{1.3}, \quad (30)$$

where S is the cross-sectional area of the screw channel or die.

2.3 Numerical Calculation

Fig. 2 shows the flowchart of our numerical calculation. Our goal is to obtain pressure p , temperature T , and zero-shear viscosity at a reference temperature η_r for all axial positions of the extruder when an initial temperature T_i and an initial zero-shear viscosity at a reference temperature η_{ri} are given. From now on, we denote z as the axial coordinate of the extruder.

Firstly, we evaluate the Nusselt number of the screw Eq.(17). Next, we give initial guesses for temperature and zero-shear viscosity at the exit of the extruder $z = z_f$. The pressure at $z = z_f$ is the atmospheric pressure, which is set to zero. The distributions of p , T , and η_r along

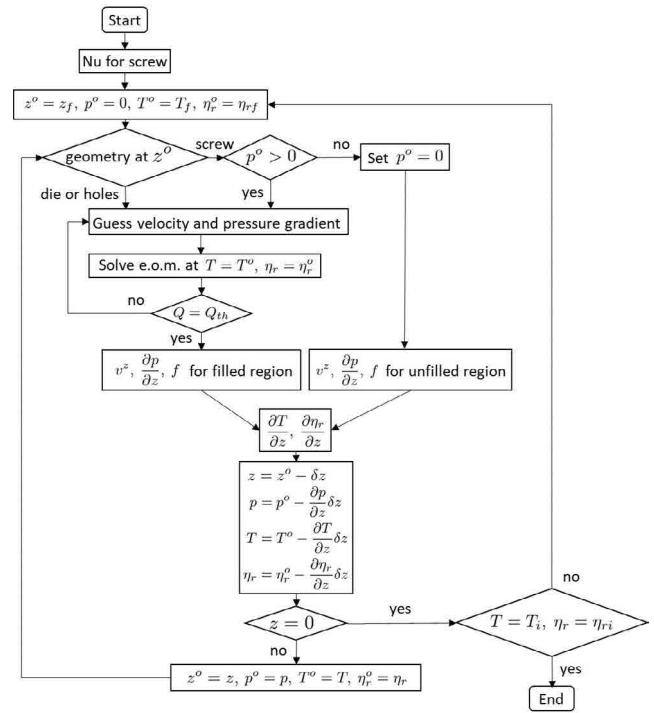


Fig. 2 Flowchart of numerical calculation. The Q_{th} is defined by the right hand side of Eq.(3) or Eq.(20)

the axial direction are calculated in reverse order from the values at $z = z_f$.

If a geometry at an axial position $z = z^0$ is a cylinder, we solve the equations Eqs.(18) and (20) by an iterative method with appropriate initial guesses for velocity $v^z = \hat{v}^z$ and pressure gradient $\partial p / \partial z = \hat{a}$. We choose \hat{v}^z and \hat{a} to the analytic solutions in the case of power-law fluid. If a geometry at $z = z^0$ is a screw and the pressure p^0 is positive, the screw is fully filled with resin. The Eqs.(1) and (3) are solved in the same way as the case of cylinder. If $p^0 \leq 0$, the screw is partially filled with resin and p^0 is reset to zero. In the unfilled regions, the velocity is given by Eq.(4) and the pressure gradient vanishes. We used the finite volume method to solve Eqs.(1) and (18).

Then, the temperature gradient $\partial T / \partial z$ and the gradient for the zero-shear viscosity $\partial \eta_r / \partial z$ at $z = z^0$ are evaluated by using Eqs.(13) and (30). Then, the pressure, temperature, and zero-shear viscosity at $z^0 - \delta z$ are calculated, where δz is a size of discretization for z axis. Repeating the calculations, we obtain p , T , η_r at $z = 0$. The temperature and zero-shear viscosity at the exit are updated iteratively so that the calculated values of the temperature and zero-shear viscosity at $z = 0$ are close enough to T_i and η_{ri} . After the iterative calculations, we obtain p , T , η_r for all z which satisfy the initial conditions.

3 Experiment

3.1 System

The total system of our experiments is shown in Fig. 3. Two different extruders were used, which were tandemly connected. The first one was a self-wiping co-rotating twin-screw extruder ($L/D = 48.5$, $D = 26$ mm, Shibaura Machine, Shizuoka, Japan), which was just used for melting resin. The screw configuration, the barrel temperatures and the screw rotation speeds used in the following experiments are shown in the Appendix B. The resin temperature at the exit of the twin-screw extruder was 195°C in all experiments. The second one was a high-shear extruder, which was a single screw extruder with a maximum rotational speed of 3600 min^{-1} . The inner diameter of barrel was 48 mm. In the high-shear extruder, the resin was thermally decomposed by the shear-induced heat. The screw was composed of multiple different screw elements such as a usual twin-screw extruder. The high-shear extruder possessed a screw element with circular through-holes, which is shown in Fig. 4. The resin was dammed by the reverse flighted screw element and flowed into the through-holes. The role of this element was to make the

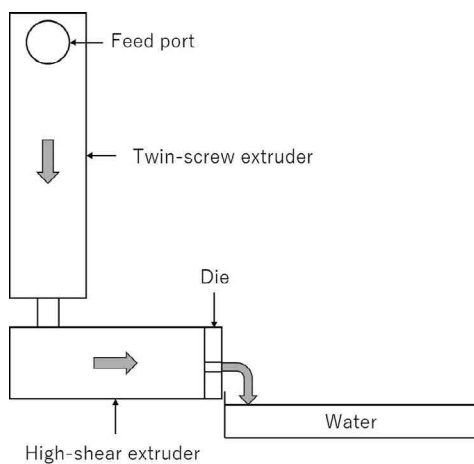


Fig. 3 Total system of our experiments. The twin-screw extruder and the high-shear extruder were connected by a circular single tube with the diameter of 10 mm and the length of 150 mm. The resin was fed from the feed port, and flows in the twin-screw extruder, followed by the high-shear extruder.

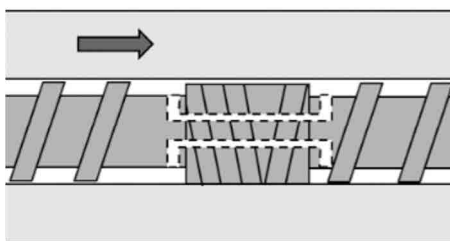


Fig. 4 Screw elements with through-holes. The arrow indicates the flow direction of resin.

fully filled region in front of the reverse flighted screw, but not to give too much shear stress to the resin to prevent the excessive degradation. The discharged resin from the die of the high-shear extruder was immediately cooled by water and dried appropriately.

3.2 Materials

Two different grades of homo-polypropylene (F-704NP and J107G, Prime Polymer, Tokyo, Japan) were used. The melt flow rates were 7.0 and 30 g/10min, respectively, measured in accordance with the ISO 1133:97 standard. In the following, we denote F-704NP as PP1 and J107G as PP2. To determine the parameters of the viscosity model Eqs.(6) and (7), the shear viscosity was measured by a modular compact rheometer (MCR 102, Anton Paar, Graz, Austria). The steady shear rate ranged from 0.01 to 100 s^{-1} and the measurement temperatures were 190, 200, and 210°C . The reference temperature was set to 200°C . The resultant model parameters of PP1 and PP2 by curve fitting were given in Table 1. The viscosity data and curves are shown in Fig. 5 and 6.

Table 1 Parameters of Cross model for PP1 and PP2 with $T_r = 473\text{K}$.

Sample	η_r [Pa·S]	T_r [K]	τ_r [Pa]	n
PP1	5.15×10^3	6.87×10^3	6.87×10^3	0.403
PP2	9.47×10^2	6.80×10^3	9.26×10^3	0.324

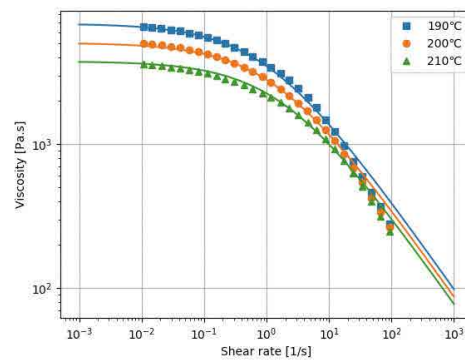


Fig. 5 Viscosity data and curves for PP1.

To determine the activation energy of PP, the Kissinger's method was used, which was reviewed in [20]. To obtain the weight loss data for thermal degradation of PP, the simultaneous thermogravimetric analyzer (STA7200, Hitachi High-Tech Science, Tokyo, Japan) was used. For samples, PP1 was used. The samples were purged with the air at a flow rate of 30 mL/min because the air was expected to exist in the high-shear extruder. Constant heating rates of 2, 4, and $8^\circ\text{C}/\text{min}$ were used. For each case, the sample weight was approximately 10 mg. The results of the thermogravimetric analysis (TGA) are shown in Fig. 7. The temperature T at a given weight fraction of

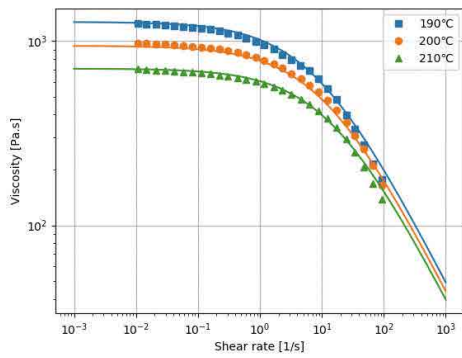


Fig. 6 Viscosity data and curves for PP2.

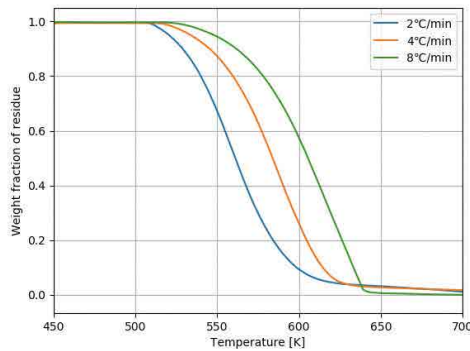


Fig. 7 TGA curves with different constant heating rates for PP1.

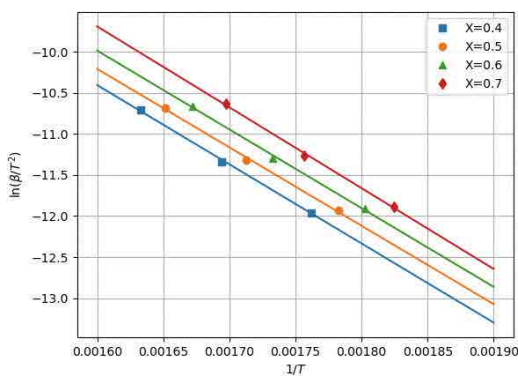


Fig. 8 Sets of data ($1/T, \ln(\beta/T^2)$) at a fixed X and fitting curves.

residue X was found for each heating rate β . The Kissinger's method uses the following equation:

$$\ln\left(\frac{\beta}{T^2}\right) = -\frac{E}{R_g T} + \text{const.} \quad (\text{at a fixed } X), \quad (31)$$

where E [J/mol] is the activation energy and R_g is the gas constant. Fig. 8 shows the sets of data ($1/T, \ln(\beta/T^2)$) and the fitting curves for $X = 0.4, 0.5, 0.6,$ and 0.7 . The values of E at $X = 0.4, 0.5, 0.6, 0.7$ were $E = 8.006 \times 10^4, 7.930 \times 10^4, 7.964 \times 10^4, 8.175 \times 10^4$, respectively. Thus, we obtained $E = 80.2 \pm 0.94$ [kJ/mol]. This value will be valid because the activation energy of PP at temperatures of less than 404 to 421°C was found to be 98.3 ± 3.1 kJ/mol by TGA under argon atmosphere in [20]. Our result was smaller than that of [20] because of the oxidative degradation. In the following, we set $E = 80.2$ kJ/mol.

3.3 Investigation of Nusselt Number

The screw configuration of the high-shear extruder is shown in Fig. 9. The screw elements with a channel depth of 3 mm, a lead of 15 mm, and a length of 45 mm were used. The die with a diameter of 4 mm and a length of 25 mm was used. The flow rate was 4.8 kg/h. The barrel temperature was set to 195°C and 300°C. The screw rotational speeds of 100, 1000, and 2000 min^{-1} were chosen. For resin, PP1 was used. The temperature of PP at the exit of the die was measured.

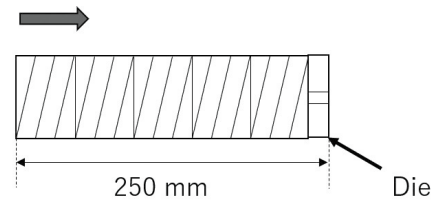


Fig. 9 Screw configuration to investigate Nusselt number. The arrow indicates the direction of flow.

3.4 Degradation of PP with High-Shear Extruder

3.4.1 Experiment 1

The screw configuration of the high-shear extruder is shown in Fig. 10. The screw was mainly composed of screw elements with a channel depth of 3 mm, a lead of 22.5 mm, and a length of 45 mm. The last screw element had the same channel depth as the previous ones with a different lead of 15 mm and a different length of 30 mm. The shaded region in Fig. 10 represents the reverse flighted screw element with through-holes which was shown in Fig. 4. This element possessed four through-holes with a diameter of 2 mm and a length of 45 mm. The die of the high-shear extruder had the diameter of 2 mm and the length of 25 mm. The barrel temperature was set to 195°C. The flow rate was 4.8 kg/h. The screw rotational speeds of 2000, 2500, 3000, and 3600 min^{-1} were used. For resin, PP1 was used. The temperature of PP was measured at the point P in Fig. 10 and the exit of the die. The zero-shear viscosity of the processed PP was measured at the reference temperature 200°C.

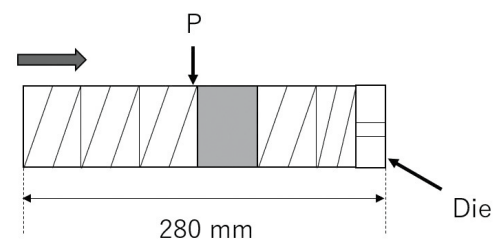


Fig. 10 Screw configuration of experiment 1. The arrow indicates the direction of flow.

3.4.2 | Experiment 2

The screw configuration of the high-shear extruder is shown in Fig. 11. The screw elements with a channel depth of 3 mm, a lead of 15 mm, and a length of 45 mm were used. The shaded regions were the same as that of experiment 1. The die with a diameter of 3 mm and a length of 25 mm was used. For resin, PP2 was used. The flow rate and the screw rotational speed were fixed to 10 kg/h and 3600 min⁻¹, respectively, but the barrel temperatures were set to 300 and 350°C. The resin temperature was measured at the exit of the die. The zero-shear viscosity of the processed samples was measured at the reference temperature 200°C.

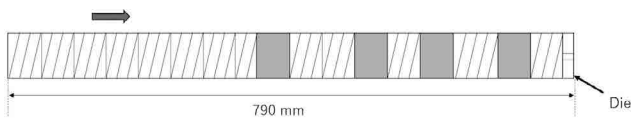


Fig. 11 Screw configuration of experiment 2. The arrow indicates the direction of flow.

4 Results

4.1 | Investigation of Nusselt Number

Table 2 shows the simulation and experimental results described in section 3.3. When the barrel temperature was raised from 195°C to 300°C with the fixed screw rotation speed of 100 min⁻¹, the calculated Nusselt number was a little bit increased. Therefore, the calculated temperature at the exit of the high-shear extruder T_f in our simulation was also changed compared to the calculated value of T_f with $Nu = 8.92$, which was the Nusselt number evaluated at $N = 100$ min⁻¹ and $T_b = 195$ °C. With the modification of the Nusselt number, the simulation result approached the experimental result.

When the screw rotation speed was increased from 100 min⁻¹ to more than 1000 min⁻¹ with the fixed barrel temperature of 195°C, the calculated Nusselt number was largely increased. This was because a heat transfer coefficient in a forced convection depends on the

Table 2 Simulation and experimental results of the experiments described in Section 3.3. The outlet temperature is denoted by T_f . The values of T_f in parentheses were the calculated values at $Nu = 8.92$.

N [min ⁻¹]	T_b [°C]	Nu	T_f [°C]	
			Sim.	Exp.
100	195	8.92	216	213
100	300	10.9 (8.92)	280 (274)	290
1000	195	15.1 (8.92)	318 (328)	287
2000	195	17.2 (8.92)	375 (393)	307

fluid velocity so that the resin with a high velocity was much cooled by the barrel. As a result, the predicted values of T_f in our simulation largely decreased compared to the calculated values of T_f with $Nu = 8.92$. Thus, we found that our simulation surely took into account the dependence of the screw rotational speed and the barrel temperature on the Nusselt number, which was not considered in [16]. The large discrepancies of T_f between the simulations and the experiments at $N = 1000$ and 2000 min⁻¹ were caused by the viscosity reduction due to the thermal decomposition.

4.2 | Degradation of PP with High-Shear Extruder

Fig. 12 shows the simulation results and experimental results of experiment 1 when the screw rotational speed was 3600 min⁻¹. If the frequency factor A was equal to zero, the prediction of temperature at the exit of the high-shear extruder did not agree with the experimental result because the reference zero-shear viscosity η_r did not decrease and the shear-induced heat was overestimated. Setting $A = 5.7 \times 10^5$, the simulation result agreed well with the experimental results. In the following, A was fixed to this value.

The numerical values of simulation results and experimental results in experiment 1 were summarized in Table 3. For all screw rotational speeds, the predictions of T_p and η_r quite matched with the experimental results, but the outlet temperatures T_f in the simulation were smaller than the experimental ones. This issue will be explained later.

Fig. 13 shows the simulation results of the distributions of temperature and reference zero-shear viscosity in experiment 1. As the

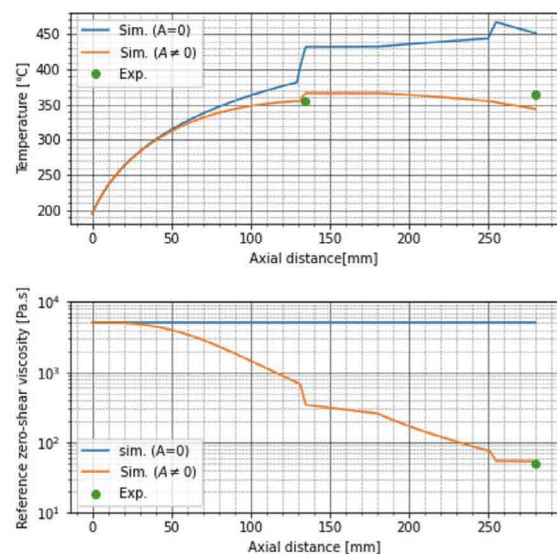


Fig. 12 Comparison of simulation results and experimental results in experiment 1 when screw rotational speed was 3600 min⁻¹.

screw rotational speed increased, the temperature increased and the reference zero-shear viscosity decreased because of the thermal decomposition. The zero-shear viscosity greatly decreased in front of the through-holes and the die because the screw was fully filled with resin here and the maximum shear stress and the residence time became large. Inside the through-holes and the die, the degradation was suppressed because the shear stress and the residence time were small. The through-holes were not cooled or warmed, so the temperature did not change so much. However, the temperature decreased in the die because the die was kept at 195°C. After the resin was discharged from the through-holes, the temperature gradually decreased despite of the high screw rotational speeds. This is because the shear-induced heat was reduced due to the viscosity reduction in front of the through-holes and the heat conduction to the barrel became dominant. However, as we saw in Table 3, the experimental outlet temperatures were higher than those of our simulation. We do not see the reason clearly yet, however one of the possible reasons is that we treated the Nusselt number as a global value. Generally, the Nusselt number depends on the distance of the system. In our case, the Nusselt

Table 3 Simulation and experimental results of temperature at point P , denoted by T_p , outlet temperature T_f , and outlet reference zero-shear viscosity η_{rf} in experiment 1.

N [min^{-1}]	T_p [$^{\circ}\text{C}$]		T_f [$^{\circ}\text{C}$]		η_{rf} [$\text{Pa}\cdot\text{S}$]	
	Sim.	Exp.	Sim.	Exp.	Sim.	Exp.
2000	337	343	322	351	162	143
2500	348	352	330	360	109	113
3000	356	346	337	364	78.6	76.1
3600	366	355	344	365	53.8	48.2

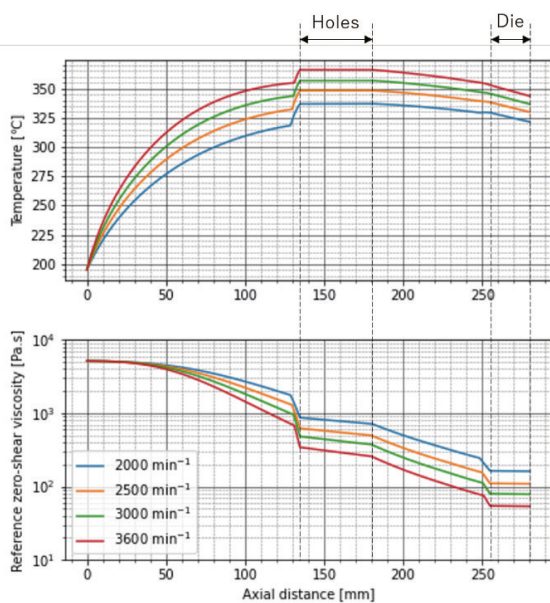


Fig. 13 Predictions of temperature distribution and distribution of reference zero-shear viscosity in experiment 1.

number around the exit of the extruder will be smaller than that around the entrance. Then, the heat conduction from the barrel after the through-holes becomes smaller and the temperature decrease in the simulation will be suppressed. However, to accommodate the local heat transfer in the simulation will be difficult because the heat conduction equation Eq.8 must be solved backwards in the axial direction. It seems to be impossible to set a good initial guess of the temperature distribution at the exit of the extruder so as to converge the calculation.

Table 4 Simulation and experimental results of outlet temperature T_f , and outlet reference zero-shear viscosity η_{rf} when barrel temperature T_b was 300 and 350°C in experiment 2.

T_b [$^{\circ}\text{C}$]	T_f [$^{\circ}\text{C}$]		η_{rf} [$\text{Pa}\cdot\text{S}$]	
	Sim.	Exp.	Sim.	Exp.
300	341	375	12.8	16.9
350	365	380	5.25	5.51

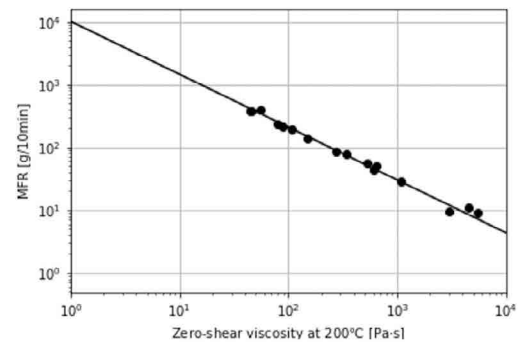


Fig. 14 Calibration curve of MFR for homo-PP.

To make PP with a value of MFR over 1000 g/10min, the experiment 2 was performed. Since a high resin temperature and a long residence time were necessary to reduce the zero-shear viscosity, the barrel temperature was changed to a value more than 300°C. The screw rotational speed was fixed to the maximum value of 3600 min^{-1} . The long screw was used and four dams with the through-holes were inserted.

The simulation and the experimental results of the outlet temperature and the outlet reference zero-shear viscosity in the experiment 2 were summarized in Table 4. Although the outlet temperatures of the simulation were lower than the experimental ones as was expected from experiment 1, the simulation results of the reference zero-shear viscosity were in agreement with the experimental ones. The viscosity of both samples were too low to measure the value of MFR directly using a melt indexer. However, a logarithm of a reference zero-shear viscosity of PP was almost proportional to a logarithm of the value of MFR, so we created a

calibration curve of MFR which is shown in Fig. 14. Using this calibration curve, the values of MFR for $T_b = 300^\circ\text{C}$ and 350°C were 938 g/10min and 2411 g/10min, respectively. Thus, we could produce the degraded PP with a value of MFR over 1000 g/10min using our high-shear extruder.

5 Conclusions

In general, to manufacture melt-blown nonwoven fabric sheets of PP, we need a low viscosity grade of PP with the value of MFR around 1000. We demonstrated that we could produce the degraded PP with the value of MFR over 1000 g/10min from the commercial PP (MFR = 30 g/10min) by the high-shear extruder without using the peroxides. To fabricate the PP with the value of MFR over 1000 g/10min, the maximum screw rotation speed of 3600 min^{-1} and the barrel temperature over 300°C were used. From the TGA analysis shown in Fig. 7, the thermal decomposition of PP started at around 250°C in the air. The temperature of PP in the high-shear extruder exceeded the thermal decomposition temperature by 100°C . By varying the screw rotation speed from 2000 min^{-1} to 3600 min^{-1} with the fixed barrel temperature of 195°C , the outlet zero-shear viscosity decreased by around $100\text{ Pa}\cdot\text{s}$. This shows that the viscosity of polymers can be adjusted easily and quickly only by the screw rotation speed of the high-shear extruder.

Using the degraded PP, a meltblown nonwoven fabric sheet was really produced, which is shown in Fig. 15. The value of MFR of the degraded PP was 1148 g/10min, and the yellow index was 5.68, which was a little bit higher than that before high-shear rate processing, 3.71. As can be seen in Fig. 15, the appearance of the sheet was white enough. The feeling of touch was also good. In fact, no shot (agglomerates of polymers that are larger than fibers) was confirmed in the image of the scanning electron microscope (SEM) which is shown in Fig. 16. The average fiber diameter was $1.6\text{ }\mu\text{m}$.

It is interesting to apply the high-shear rate processing to fabricate low-viscosity engineering plastics for the meltblown process because those raw materials are less commonly available in market than low-viscosity PP. The meltblown nonwoven fabrics made of the engineering plastics are applied to the heat-resistant air filters, etc. However, it is challenging to degrade any engineering plastics by the high-shear extruder sufficiently because those materials are obviously hard to decompose thermally. In the high-shear extruder, the shear-induced heat becomes gradually small as the resin is



Fig. 15 Meltblown nonwoven fabric sheet which was made of degraded PP by high shear extruder. We used PP2 as the raw material because no talc was included as the additives.

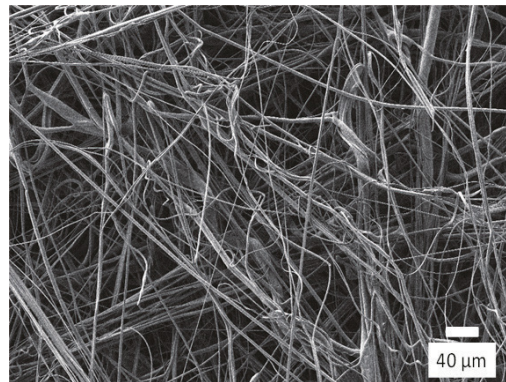


Fig. 16 SEM image of meltblown nonwoven fabric sheet in Fig. 15.

thermally decomposed because the shear stress is proportional to the viscosity. Then, the heat conduction to the barrel becomes dominant compared to the heat generation. In fact, in the simulation of the experiment 1, the resin was cooled by the barrels as we saw in Fig. 13. This will suppress the thermal decomposition of resin with a high thermal decomposition temperature. This issue might be solved by replacing the barrels to adiabatic walls.

The viscosity of the degraded PP in our experiments was too low to extrude in a strand shape. Thus, small lumps of the extruded PP were crushed and the particles, whose size was of the order of 1 mm, were obtained to be fed into the meltblown equipment. To pelletize such low-viscosity PP, we have to use an under water cutter, which is hard to manage. A low-viscosity grade of resin for the meltblown process is sometimes only available in powder forms, and feeding the powders to the meltblown equipment is awkward because powders generally tend to be cohesive and also tend to entrap air. However, if the high-shear extruder is combined tandemly

with the meltblown equipment, we can manufacture the meltblown nonwoven fabric sheets from the standard grades of resin, which are supplied in pellet form and always available anywhere at low cost. Furthermore, various meltblown nonwoven fabric sheets with different physical properties will be easily produced by changing the screw rotational speed of the high-shear extruder. We are now developing the integrated manufacturing process of meltblown nonwoven fabrics.

We also developed the simulation of the shear-induced thermal decomposition of resin in the high-shear extruder. By the nature of the high screw rotation speed and the wide range of the operational conditions, the simulation of the high-shear rate processing was not so easy. In fact, as described in [16], the heat transfer coefficient should be modulated by the screw rotation speed to predict the resin temperature at high-shear rates. Of course, we need to take into account the effect of the viscosity reduction by the thermal decomposition. In our one dimensional flow model, the global Nusselt number in the screw was estimated by solving the heat conduction equation Eq.8 in the case of the simple shear flow. We found that the Nusselt number did not change so much as the barrel temperature was increased from 195°C to 300°C, but the large deviations occurred by changing the screw rotation speed from 100 min⁻¹ to more than 1000 min⁻¹. By coupling the flow model to the kinetic equation of the viscosity reduction, which was derived in section 2.2, we found that our simulation results agreed well with the experimental results even when the operational conditions were widely changed. The simulation predicted that the large viscosity reduction occurred in front of the dams such as the through-holes and the die because the shear stress and the residence time were expected to be large in the fully filled regions of screw. Therefore, we installed many dams in the screw to obtain the low-viscosity PP with MFR over 1000 g/10min in the experiment 2.

The numerical simulation to predict the number-average molecular weight and weight-average molecular weight under the thermal degradation in a twin-screw extruder were developed [13]. Using their kinetic equations of the molecular weights, we will be able to predict the polydispersity index during the high-shear rate processing. In the meltblown process, the polydispersity index of the raw material will affect the variance of the fiber diameters. Since the high-shear rate processing utilizes the thermal decomposition of polymers, which is the random scission process, the polydispersity index tends to be small. However, the quantitative prediction during

the high-shear rate processing is missing. It will be interesting to see how to change the polydispersity index with the screw configurations and the operational conditions of the high-shear extruder.

In our simulation, the resin temperatures at the exit of the high-shear extruder were a little lower than the experimental results. The possible reason is that the dependence of the Nusselt number on the distance in the system was not considered in our model. However, obtaining the full local Nusselt number is difficult. This is because the heat conduction equation is usually solved forwards with a homogeneous initial condition, but we have to proceed the calculations backwards to specify the unfilled regions. If the barrels of the high-shear extruder were adiabatic, consideration of the heat conduction would not be appeared.

Appendix A. Nomenclature and Definition of Symbols

A	frequency factor in the kinetic model of viscosity reduction [Pa ^{0.3} ·s ^{-1.3}]
C_p	heat capacity of resin [J/(kg·K)]
D	inner diameter of the barrel [m]
E	activation energy of thermal decomposition [J/mol]
f	fill ratio [-]
H	height of the screw channel [m]
k	reaction rate of thermal decomposition [1/s]
l	length of the die [m]
L_p	path length of the screw [m]
L/D	ratio of total length of screw to inner diameter of barrel in an extruder [-]
n	exponent in the Cross model [-]
$n_{\mathcal{N}}$	number of polymers with \mathcal{N} number of nodes [-]
N	screw rotational speed [1/s]
\mathcal{N}	number of nodes of a linear polymer [-]
$\bar{\mathcal{N}}$	number average degree of polymerization [-]
Nu	average Nusselt number [-]
Nu_z	local Nusselt number at z [-]
p	pressure of resin [Pa]
q	heat flux [W/m ²]
Q	flow rate [m ³ /s]
r	radial coordinate of the die [m]
R	radius of the die [m]
R_g	gas constant = 8.31 J/(mol·K)
S	cross-sectional area of the screw channel or die [m ²]
t	time [s]

T	temperature of resin [K]
T_b	barrel temperature [K]
T_f	exit temperature of the high-shear extruder [K]
T_r	reference temperature [K]
T_w	temperature of the die [K]
T_*	model parameter of the zero-shear viscosity [K]
v^z	z-component of the fluid velocity [m/s]
V	velocity of the barrel with respect to an observer on the screw [m/s]
V^z	z-component of V [m/s]
W	width of the screw channel [m]
x	coordinate of the channel width direction of the screw [m]
X	weight fraction in TGA analysis [-]
y	coordinate of the channel depth direction of the screw [m]
z	coordinate for down-channel direction or axial direction of the screw [m]
α	pressure gradient [Pa/m]
β	heating rate in TGA analysis [°C/min]
$\dot{\gamma}$	shear rate of resin [1/s]
η	non-Newtonian viscosity of resin [Pa·s]
η_0	zero-shear viscosity in the Cross model [Pa·s]
η_r	zero-shear viscosity at T_r [Pa·s]
η_{rf}	value of η_r at the exit of the high-shear extruder [Pa·s]
κ	thermal conductivity of resin [W/(m·K)]
ρ	melt density of resin [kg/m ³]
τ	shear stress of resin [Pa]
τ_*	characteristic shear stress in the Cross model [Pa]
ϕ	screw angle [rad]

Appendix B. Setup of Twin-Screw Extruder

The screw configuration and the barrel temperatures of the twin-screw extruder in the experiments are shown in Fig. A1. The total length was 1260 mm and the inner diameter of the barrel was 26 mm. The flow rate and the screw rotation speed used in the experiments were summarized in Table A1.

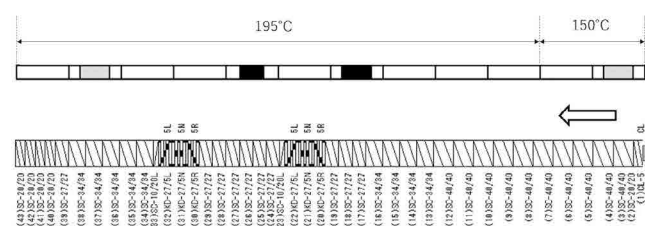


Fig. A1 Screw configuration and barrel temperature of twin-screw extruder. The arrow indicates the flow direction. Names of the screw elements are as defined in the catalog of SHIBAURA MACHINE CO., LTD.

Table A1 The flow rate Q and the screw rotation speed N of the twin-screw extruder in the experiments.

Q [kg/h]	N [min ⁻¹]
4.8	80
10	100

References

- Dutton, K. C. Overview and analysis of the meltblown process and parameters. *J. Text. Apparel, Technol. Manage.*, 2009, 6, 1–25.
- Takarada, W.; Hatano, S.; Kikutani, T.; Experimental and Numerical Analysis of Unstable Behavior of Melt Blowing Process. *J. Fiber Sci. Technol.*, 2020, 76, 208-216.
- Berzin, F.; Vergnes, B.; Dufossé, P.; Delamare, L. Modeling of peroxide initiated controlled degradation of polypropylene in a twin screw extruder. *Polym. Eng. Sci.*, 2000, 40, 344-356.
- Vergnes, B.; Berzin, F.; Peroxide-controlled Degradation of Poly(propylene): Rheological Behaviour and Process Modelling. *Macromol. Symp.*, 2000, 158, 77-90.
- Iedema, P. D.; Willems, C.; van Vliet, G.; Bunge, W.; Mutsers, S.; Hoefsloot, H.; Using molecular weight distributions to determine the kinetics of peroxide-induced degradation of polypropylene. *Chem. Eng. Sci.*, 2001, 56, 3659-3669.
- Iedema, P. D.; Remerie, K.; van der Ham, M.; Biemond, E.; Tack, J. Controlled peroxide-induced degradation of polypropylene in a twin-screw extruder: Change of molecular weight distribution under conditions controlled by micromixing. *Chem. Eng. Sci.*, 2011, 66, 5474.
- Cassagnau, P.; Bounor-Legaré, V.; Vergnes, B.; Experimental and modelling aspects of the reactive extrusion process. *Mech. Ind.*, 2019, 20, 803.
- Shimizu, H.; Li, Y.; Kaito, A.; Sano, H.; Formation of Nanostructured PVDF/PA11 Blends Using High-Shear Processing. *Macromolecules*, 2005, 38, 7880-7883.
- Li, Y.; Shimizu, H.; High-shear processing induced homogeneous dispersion of pristine multiwalled carbon nanotubes in a thermoplastic elastomer. *Polymer*, 2007, 48, 2203-2207.
- Li, Y.; Shimizu, H.; Fabrication of Nanostructured Polycarbonate/ Poly(methyl methacrylate) Blends With Improved Optical and Mechanical Properties by High-Shear Processing. *Polym. Eng. Sci.*, 2011, 51, 1437.
- Louizi, M.; Massardier, V.; Cassagnau, P.; Contribution of High-shear Processing to the Compatibilization of (PP/EPR)/PE Ternary

Blends. *Macromol. Mater. Eng.*, 2014, 299, 674-688.

- 12) Ishigami, A.; Kodama, Y.; Suenaga, H.; Inoue, T.; Ito, H.; Mechanical Properties and Structure of Novel Polymer Blends and Composites Fabricated by Reactive and High-shear Rotational Processing. *Energy Procedia*, 2016, 89, 30-37.
- 13) Kim, B.; White, J. L.; Simulation of Thermal Degradation, Peroxide Induced Degradation, and Maleation of Polypropylene in a Modular Co-Rotating Twin Screw Extruder. *Polym. Eng. Sci.*, 1997, 37, 576.
- 14) Farahanchi, A.; Sobkowicz, M.J. Kinetic and process modeling of thermal and mechanical degradation in ultrahigh speed twin screw extrusion. *Polym. Degrad. Stab.* 2017, 138, 40-46.
- 15) Blancas, C.; Vargas, L.; Modeling of the industrial process of peroxide-initiated polypropylene (homopolymers) controlled degradation. *J. Macromol. Sci.*, 2001, B40, 315-326.
- 16) Fel, E.; Massardier, V.; Mélis, F.; Vergnes, B.; Cassagnau, P.; Residence Time Distribution in a High Shear Twin Screw Extruder. *Int. Polym. Proc.* 2014, 29, 71-80.
- 17) Bird, R.B.; Armstrong, R.C.; Hassager, O. *Fluid Mechanics. Dynamics of Polymeric Liquids.* 2nd ed.; John Wiley and Sons Inc: New York, NY, USA, 1987; Volume 1.
- 18) Rubinstein, M.; Colby, R.H. *Polymer Physics*; Oxford University Press Inc.: New York, NY, USA, 2003.
- 19) Suehiro, T.; O'shima, E. A kinetic study on the random scission of a polymer; *Kobunshi Ronbunshu.* 1977, 34, 241-248.
- 20) Chan, J. H.; Balke, S. T. The thermal degradation kinetics of polypropylene: Part III. Thermogravimetric analyses. *Polym. Degrad. Stab.* 1997, 57, 135-149.

On-Machine Measurement for Ultra-Precision Machining in the Field of Automotive Products

This report content is a partially revised version of a technical paper published in the Journal of the Japan Society for Precision Engineering, Vol. 85, Issue 7, p. 628, published by the Japan Society for Precision Engineering.



Masahiko FUKUTA
Machine Tools Company, Machine Tools Engineering Department

1 Introduction

The mass production of aspheric lenses and a variety of other ultra-precision optical parts has significantly contributed to the performance improvement and cost reduction of optical and information equipment. These include aspheric plastic lenses used in digital cameras, pickup lenses used in optical disk devices, fθ lenses in laser printers, and free-form mirrors used in projectors and head-up displays. In particular, the mold machining quality for plastic optical parts mass-produced by the injection molding method has improved remarkably. The requirement for machining accuracy of molds for aspheric lenses was around 0.1 to 0.2 μmPV about 15 years ago, but in recent years it has become around 0.05 μmPV, and a surface roughness of 1 nmRa or less can also be attained.

Ultra-precision optical parts are increasingly being applied to automotive optical products. A typical example is headlights using LED light sources, which offer flexibility in design in addition to low power consumption and long life. However, the required optical performance is not limited to smooth optical surfaces but may involve the formation of minute irregularities on optical surfaces to satisfy light distribution characteristics.

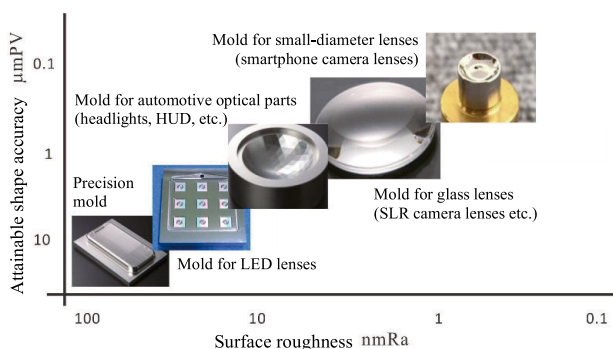


Fig. 1 Fields where ultra-precision machining is used.

Currently, ultra-precision optical components are produced mainly in the fields shown in Fig. 1, and machining methods such as cutting, grinding, and milling are selected based on the required machining shape and quality. However, there are many issues which cannot be addressed by machining tools and machining technology alone, so peripheral technologies such as tools and measuring instruments need to be considered or developed additionally. In such circumstances, on-machine measurement is often developed based on strong market demand for difficult issues.

In this paper, we first explain the basic elements of on-machine measurement. Next, we focus on the ultra-precision machining of automotive precision parts and introduce some examples of its application.

2 Development history of on-machine measurement system

On-machine measurement for ultra-precision machining was first considered in earnest when the demand for aspheric lenses increased with the spread of digital cameras. Most of these plastic lenses are produced by the injection molding method using stainless steel molds with electroless NiP plating which are turned with single-crystal diamond tools. Although this can obtain reproducible machining quality in a relatively short time, Tanaka discussed the importance of measurement stability for post-machining shape evaluation from the viewpoint of mass production¹⁾. However, measuring instruments which could provide sufficient measurement accuracy were not widely available, so study of on-machine measurement was conducted for the purpose of high-precision measurement. The measurement probe developed at that time was equipped with a mechanism which could adjust the measurement

pressure by air pressure control, realizing extremely low pressure measurement from 0 to 500 mgf and enabling highly accurate measurement ²⁾.

The next time the demand for on-machine measurement increased was when the machining of free-form surfaces on molds for laser printer fθ lenses attracted attention. These molds were machined by raster scanning a fly cut tool with a single-crystal diamond attached. The accuracy requirements for mold machining were high, and the machining could take several tens of hours. Air cuts caused by workpiece mounting errors were a major factor in the reduction of mass-productivity. Therefore, on-machine measurement which evaluates and corrects the shape without removing the workpiece from the machine was studied. This measurement requires not only conventional cross-sectional scanning through the center utilizing the rotational symmetry of the shape, but also evaluation of the entire mold surface. Therefore, the system's functions were enhanced by utilizing high-speed intercommunication with the NC and reflecting the calculation results of the measurement data in the scanning trajectory.

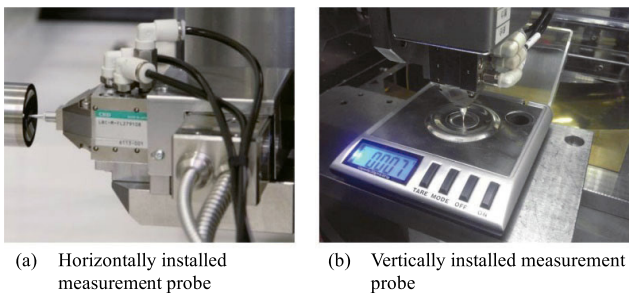


Fig. 2 On-machine measurement probe

About 10 years ago, on-machine measurement for the machining of molds for pickup lenses attracted attention. Glass was selected as the lens material from the viewpoint of optical characteristics, and the glass molding method was used. Therefore, high-hardness materials such as heat-resistant cemented carbide and SiC were used as mold materials, and the grinding method was selected for mold machining. On the other hand, since the shape is compatible with high NA, a difficult mold machining was needed, which required high shape accuracy with deep inclined surfaces. For these reasons, the study of on-machine measurement, which enables measurement and evaluation without removing the workpiece, was promoted. Furthermore, the accuracy of measurement was improved by establishing traceability, such as correction of stylus radius using

a reference sphere.

In the past four to five years, there has been an increasing demand for high-precision machining of relatively large free-form surfaces such as head-up displays. In such cases, vertical turning setups are sometimes used for machining stability, and conventional measurement systems which use the horizontal probe could not accommodate this, leading to the development of an on-machine measurement system which can be installed vertically ³⁾.

After the development process described above, the on-machine measurement system shown in Fig. 2 is now proposed. The probe consists of; (1) a stylus with a standard ruby sphere whose sphericity is guaranteed to be within 0.1 μmPV, (2) a lightweight air slider, (3) a mechanism to set extremely low measuring force, and (4) a displacement meter to detect the amount of air slider movement. This probe can be used not only for horizontal measurement as shown in (a), but also for vertical measurement as shown in (b) by setting the measuring pressure, including the probe's own weight, to 10 mgf or less.

3 Issues for on-machine measurement

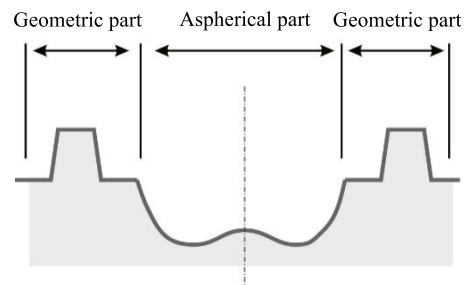
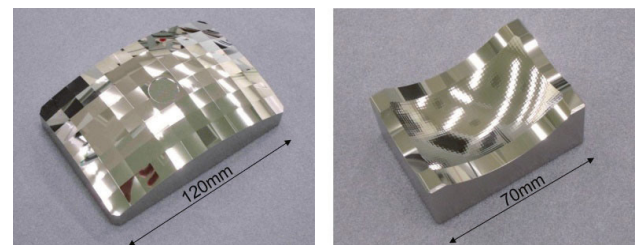


Fig. 3 Aspherical shape mold with peripheral geometry



(a) Mold for thick-walled lens with diffusion pattern (b) Mold for multi-reflector

Fig. 4 Examples of automotive optical part mold machining

There appear new issues for on-machine measurement due to the diversification of machining shapes in ultra-precision machining. In particular, it is challenging to deal with molds which combine complex optical shapes, molds with additional geometric shapes

around the lens, and molds for automotive and other applications where the machining shape is provided by defined CAD data. These are not only complex, but the details of the shape are often unclear, making it difficult to predefine probe scanning. For example, in measuring the shape of a mold for a mobile lens as shown in Fig. 3, the center of the mold is aspherical, which is defined using a mathematical formula, so the scanning trajectory can be accurately predefined, but in the peripheral geometric part, excessive travel of the slider beyond the probe stroke may occur depending on the setting error of the scanning reference point. A method to command the next scanning position based on the previous measurement data using high-speed intercommunication with the NC is also possible, but the process from data acquisition, calculation, and buffering to the NC for a large number of data points tends to increase the measurement time. On the other hand, it is difficult to evaluate the measured shape on a submicron order for complex shapes, and the measurement of CAD-defined models is limited to partial measurement with a 3D measuring instrument.

Next, with regard to dealing with the complex shapes found in automotive precision parts, high-speed cutting with small-diameter end mills, which has been developing remarkably in recent years, has improved dimensional and roughness accuracy, and the emergence of ultra-precision vertical machining centers which utilize aerostatic bearing and linear motor drive control technologies has made it possible to eliminate the need for, or minimize, polishing to attain the precision mold finish expected for ultra-precision machining⁴⁾. In the field of automotive optical parts employing LED light sources, there are increasing demands for "high quality" and "fineness" in terms of downsizing the lamp unit, increasing the brightness, improving the directivity, and expanding the designability, and there is a strong demand to eliminate mold polishing or minimize the mold polishing finish. Fig. 4 shows examples of automotive optical part mold machining using an ultra-precision vertical machining center. Fig. 4 (a) shows a mold for a thick-walled headlamp lens with a fly-eye diffusion pattern for projecting light in a diffused manner, and Fig. 4 (b) shows a mold for a multi-reflector. Both molds are made from a stainless steel mold with electroless NiP plating by milling with a single-crystal diamond tool to attain a machining quality of 10 nmRa. However, because high machining accuracy is required, there are many manual operations involved, and not much consideration has been given to labor saving and automation. Therefore, there are many issues to be

addressed to reduce manufacturing costs and ensure machining accuracy reproducibility, including the reduction of the lead time.

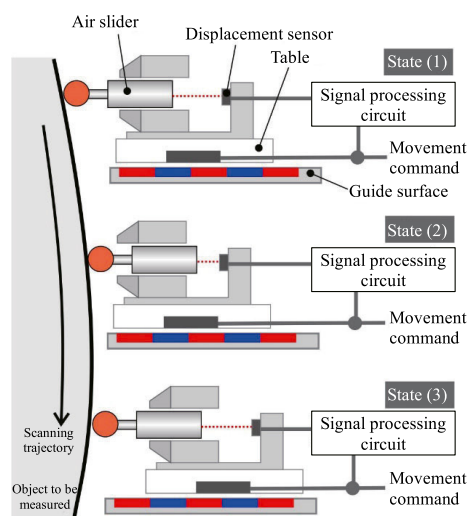


Fig. 5 Movement of servo scanning measurement probe

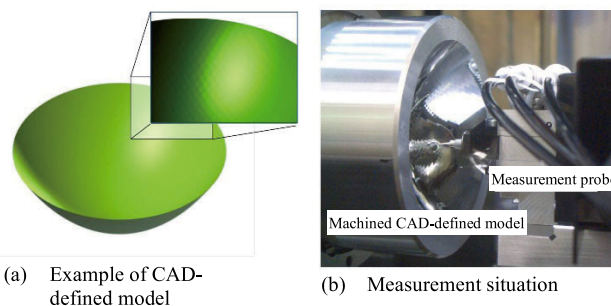


Fig. 6 Measurement of CAD model

4 Dealing with CAD-defined model

4.1 Servo scanning on-machine measurement system

A servo scanning on-machine measurement system which performs probe scanning along the measurement surface of a measurement shape on which measurement probe scanning cannot be predefined has been proposed. This system employs the conventionally used air probe which can perform scanning with an extremely low measuring force, and, as shown in Fig. 5, performs scanning by moving the table so the air slider is always kept in the same position by feeding back the detected travel to the positioning servo system of the machine. In the example shown in the figure, the measurement probe scans an uneven measurement object, and the air slider moves according to the measurement shape. Based on this moving amount detected by the displacement sensor and signal-processed, a command is given to move the table so the air

slider is kept in the same position. As a result, the scanning trajectory no longer needs to be predefined, and highly accurate measurement is now possible regardless of the shape of the object to be measured.

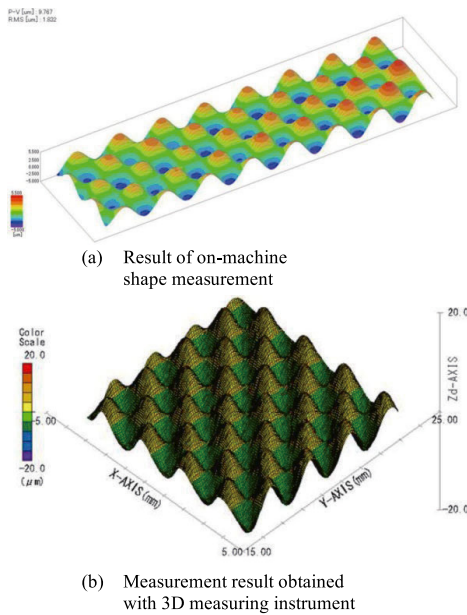


Fig. 7 Result of servo scanning measurement

4.2 Measurement example of CAD-defined model

Fig. 6 shows a CAD-defined model of an automobile part and the measurement situation. When overviewed, this model has fine irregularities distributed on a part of the near rotationally symmetric aspheric surface. However, the symmetry and irregularities can only be visually recognized on the PC screen, and the details are unclear. It is difficult for general-purpose CAM to generate highly accurate tool trajectories for such a shape in terms of tolerance and calculation accuracy. However, this system can generate tool trajectories suitable for machining with its own algorithm⁵⁾. This system has a feature which allows it to be dynamically linked, so necessary information can also be obtained from on-machine measurement software. Here, using this system, a machined CAD-defined model was measured and evaluated with the setup shown in the figure. A shape with a diameter of approximately 64 mm and a maximum inclination angle of approximately 53° was directly mirror-cut by the elliptical oscillating cutting method⁶⁾ using a single-crystal diamond tool ($R = 2$ mm). Despite the fact the details of the shape of the object to be measured were unclear, shape measurement was realized by servo scanning. Fig. 7(a) shows the evaluation result, in which irregularities on the surface can be recognized. In addition, the validation using a high-precision 3D measuring instrument

shown in Fig. 7(b) indicates the measurement results obtained by the on-machine measurement are valid.

5 Operator assistance through on-machine measurements

In most milling processes in automotive precision part machining, the tool trajectories are calculated using CAD/CAM. Machining shape accuracy is affected by tool wear, tool mounting errors, and errors caused by machine operation, and the tool trajectory is required to be corrected when errors exceed acceptable values. However, for ultra-precision machining the tolerance of which is very small, it is difficult to identify the error factors and recalculation takes a large amount of calculation time. Therefore, the application of the process described in the previous chapter, in which the machined shape is measured and evaluated using a measurement probe and then the tool trajectory is corrected, causes a significant decrease in productivity.

5.1 On-machine measurement and correction functions for milling

As a means of simultaneously achieving automation and high accuracy, an on-machine measurement and correction function as shown in Fig. 8 has been proposed. This function uses an optical line sensor to dynamically measure the shape of the tool cutting edge, and continuously acquires information on the contour of the rotating cutting edge, enabling acquisition of not only the tool diameter, but also detailed errors in the shape of the tool cutting edge and the approximate radius value of the arc cutting edge, as shown in Fig. 8(a). Furthermore, based on the measurement results of the tool cutting edge shape before and after machining, detailed measurement of the tool cutting edge wear condition is possible as shown in Fig. 8(b), and this information can be used to improve the dimensional accuracy of 3D shape machining.

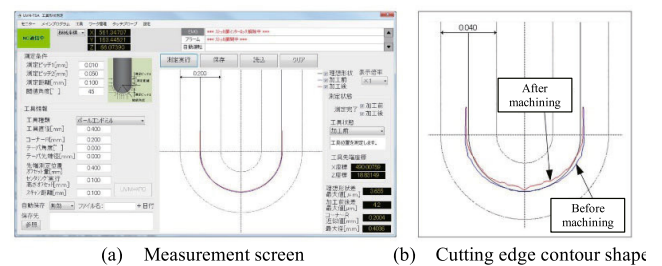


Fig. 8 Measurement example of tool cutting edge shape

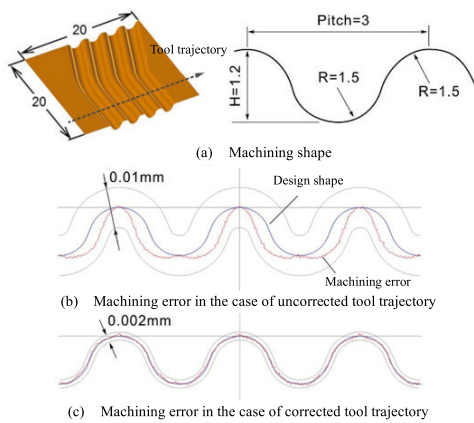


Fig. 9 Example of machining considering tool cutting edge shape

5.2 | Example of milling considering tool cutting edge shape

In the case of a CBN tool used for heat-treated stainless steel shown in Fig. 9, when the tool trajectory calculated based on the tool information provided in the product catalog and the workpiece shape is used for machining, a shape error of a few microns occurs due to the shape error of the tool cutting edge and deflection caused by cutting resistance. However, by generating a tool trajectory which accounts for the dynamic tool cutting edge shape and expected tool deflection, a shape accuracy of 0.002 mm or better can be obtained. In this process, error correction at the machining point is incorporated into the tool trajectory as a vector notation, so gradually changing error factors such as tool wear can be dealt with by changing common variables on the NC screen, eliminating the need for recalculation using CAD/CAM.

6 Conclusion

The target market of ultra-precision machining is expanding year by year, requiring process studies for transcending the framework of conventional viewpoints and ideas. In particular, the automotive precision parts field, which was thought to be less dependent upon ultra-precision machining, is expected to develop significantly in the future. In this context, on-machine measurement is an important element for obtaining reproducible machining quality and is considered a strong tool for establishing high value-added products. This paper introduces two types of on-machine measurement: one conducted after machining using a probe, and the other using an optical line sensor to check the tool cutting edge shape before machining. In this way, we hope machining and process will be developed continuously from new perspectives.

References

- 1) Katsutoshi Tanaka: Ultra-precision machining and measurement for curved surfaces and precise form parts, Proceedings of JSPE Semestrial Meeting, The Japan Society for Precision Engineering, (2009) 239-240
- 2) Sei Moriyasu: Characteristics evaluation of compact stylus-type shape measurement probe for on-machine measurement, Proceedings of JSPE Semestrial Meeting, The Japan Society for Precision Engineering, (1999) 330
- 3) Sei Moriyasu, Yutaka Yamagata, Shin-ya Morita, Hitoshi Omori, Weimin Lin, and Akitake Makinouchi: Development of vertical-type on-machine measuring probe, The Proceedings of Conference of Tohoku Branch, (2000) 111-112
- 4) Akira Amano: High value-added machining of small and precision molds using ultra-precision vertical machining center, Mechanical Engineering, 59, 1 (2011) 38-39
- 5) Kouji Tsuchiya, Masahiko Fukuta: Development of the optical components processing technology for the application of the CAD modeling profiles, Proceedings of JSPE Semestrial Meeting, The Japan Society for Precision Engineering, (2015) 213-214
- 6) Shamoto, Morimoto, Moriwaki: Elliptical vibration cutting (1st report), Journal of the Japan Society for Precision Engineering, 62, 8 (1996) 1127-1131

Three-Dimensional Observation of Graphite Structure of Thick-Walled Spheroidal Graphite Cast Iron with X-Ray CT

In thick-walled spheroidal graphite cast iron, various abnormal graphite forms not found in thin-walled structures are observed. For example, chunky graphite, which crystallizes as a result of prolonged eutectic solidification time, is a typical example of abnormal graphite structure and is known to deteriorate fatigue strength, tensile strength, and elongation. These abnormal graphite structures have been reported in many two-dimensional cross-sectional observations using optical microscopy, but there have been few reports which detect them throughout the whole of a three-dimensional structure. The purpose of this study is to present a fuller understanding of graphite distribution of graphite with complex geometries, such as chunky graphite, by imaging thick-walled graphite cast iron with different wall thicknesses using high-resolution X-ray CT and observing the three-dimensional structure of graphite. It has been found from the results of three-dimensional observation of graphite that coarse graphite increases as the eutectic solidification time increases, increasing the volume ratio of the coarse graphite. It has also been confirmed the graphite shape becomes more complex as the graphite grain size becomes greater than 60 to 67 μm . This report is a reprint of a technical paper published in "Journal of Japan Foundry Engineering Society, Vol. 93, Issue 10, p. 612", published by the Japan Foundry Engineering Society.



Ryosuke FUJIMOTO

Production Center,
Machinery & Production
Engineering Department

collective writing :

Masami TOMIZAWA

Toshiba IT & Control Systems
Corporation

Takumi HARA

Toshiba IT & Control Systems
Corporation

Katsuhiko TAKI

Nihon Visual Science, Inc.

1 Introduction

In the metal structure of thick-wall spheroidal graphite cast iron, various graphite structures are observed which are not observed in thin-walled spheroidal graphite cast iron. For example, chunky graphite, which crystallizes in large castings as the eutectic solidification time increases with thicker walls, is a typical example of such graphite structure. Besides chunky graphite, various low-melting-point elements and gas components are concentrated near the final solidification zone in the latter half of eutectic solidification, and various abnormal forms of graphite are observed under the influence of these elements.

In general, it is known mechanical properties such as fatigue strength, tensile strength, and elongation, required for spheroidal graphite cast iron used as mechanical structural parts, which deteriorate by the formation of abnormal graphite. The mechanical properties are affected by the size of the area which forms abnormal graphite. Since the abnormal graphite crystallizes in complex

shapes, it is difficult to understand the extent and range of this phenomena solely by two-dimensional cross-sectional observation. A frequent cause of part failure, especially in mechanical structural parts, is fatigue fracture, where fatigue crack propagation proceeds by fracture of the weakest continuous metallographic section. It is therefore important to understand the three-dimensional continuous graphite distribution and shape of graphite. Although there have been many reports on the results of two-dimensional observation of the graphite structure of cast iron, there are few reports which offer a clear picture of three-dimensional graphite distribution and shapes within the whole structure.¹⁻³⁾

Meanwhile, recent improvements in microscope precision and image analysis technology have made it possible to visualize the tissues inherent in various materials in three dimensions¹⁾. Three-dimensional tissue observation is often used to grasp complex tissue geometries which cannot be predicted by two-dimensional tissue observation. There have been reported results of three-dimensional tissue observation using serial sectioning 3D

microscopes⁴, SEM, TEM mirrors⁵, and X-ray computed tomography (X-ray CT) combined with an image analysis mirror¹). In particular, observation by X-ray CT, which is widely employed in nondestructive analysis in general, can analyze graphite microstructures in a wide area and in a short time, and is an effective tool for predicting the quality and mechanical properties of materials.

In thick-walled spheroidal graphite cast irons, the formation of abnormal graphite can be suppressed by appropriate casting methods, chemical composition, and molten metal treatments such as post inoculation. However, abnormal graphite may be formed due to various restrictions and factors at the manufacturing site. The objective of this study is to clarify the relationship between eutectic solidification time and the generation of coarse abnormal graphite by imaging thick-walled graphite cast iron with different wall thicknesses using high-resolution X-ray CT and by observing the three-dimensional structure of graphite. The study also aims to examine whether the material is good or bad and whether the mechanical properties can be predicted by determining the presence or absence of abnormal graphite such as chunky graphite.

2 Method of the Experiment

2.1 Sample materials

The chemical composition of sample materials is shown in Table 1. Pig iron, scrap steel, carburizer, Fe-Si, and Fe-Mn were melted in a 10-ton low-frequency melting furnace (50 Hz), and the molten metal was treated with a spheroidizing agent (Fe-Si-Mg-RE (Ce + La)) in a ladle using the sandwich method. The final target composition was C: 3.3 mass% (hereafter referred to as %), Si: 2.7%, Mn: 0.3%, P: 0.03%, S: 0.01%, Mg: 0.04%, and RE: 0.02%. The molten metal was then poured into molds of three different sizes. The names and dimensions in each thick-walled casting test piece were TP-300: 300 x 300 x 500 mm, TP-500: 500 x 500 x 500 mm, and TP-1500: 1500 x 1500 x 400 mm. Since graphite shape varies with eutectic solidification time, the eutectic solidification time of each specimen was measured; 12 ks for TP-300, 20 ks for TP-500, and 47 ks for TP-1500. Material was cut from the center of each thick-walled casting, from which a 2 x 2 x 30 mm test piece was made for X-ray CT observation.

(mass%)							
C	Si	Mn	P	S	RE	Mg	Fe
3.5	2.7	0.3	0.03	0.01	0.02	0.04	Bal.

Table 1 Chemical composition of sample materials (mass%)

2.2 Test piece observation by X-ray CT

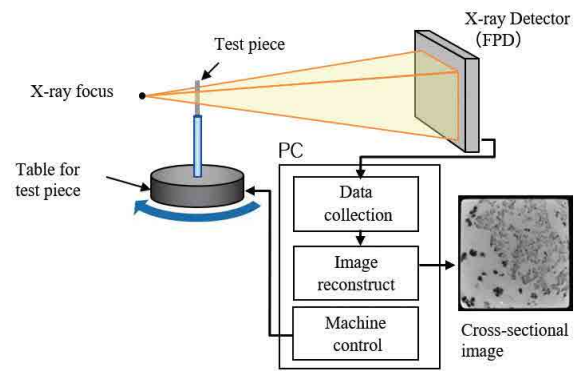


Fig. 1 Schematic of test piece observation by X-ray CT

The TOSCANER-32300 μ FD was used as the high-resolution X-ray CT. This system is a microfocus X-ray generator with a maximum tube voltage of 230 kV and a flat panel X-ray detector (FPD) with an effective field of view of 200 x 200 mm. To achieve the highest resolution for the spheroidal graphite cast iron test piece, the tube voltage was set to 200 kV, the tube current to 50 μ A, and the sampling time per view to 166 ms. A cone beam scan was performed at the rate of 3000 views/scan in the longitudinal direction of the test piece to obtain a tomographic image of 600 slices. Fig. 1 shows a schematic of test piece observation by X-ray CT. A series of X-ray CT images were loaded and the graphite structure within an area of 2.9 x 2.9 x 3.0 μ m/picture (voxel) and a visual field size of 1.74 x 1.74 x 1.80 mm was imaged in three dimensions. Three-dimensional image analysis software (ExFact VR 2.0 with the void analysis option) was used to classify and color-code the graphite structure and perform image analysis and visualization in three dimensions. The number of pixels in the image was set to 600 per side of the visual field size. The three-dimensional graphite structure was classified into five levels in terms of the effective diameter of the equivalent sphere (hereafter referred to as the graphite grain diameter): 15 to less than 50 μ m, 50 to less than 100 μ m, 100 to less than 200 μ m, 200 to less than 300 μ m, and 300 to 1000 μ m. The number of graphite nodules in one visual field (n/view), graphite volume, and volume ratio were calculated from the three-dimensional graphite structure, and the distribution of graphite structure for each classified graphite grain size was investigated. Fig. 2 shows an example of shape recognition by image processing for graphite with a graphite size of 300 to 1000 μ m. In Fig. 2, portions which appear discontinuous in the two-dimensional cross-section can be recognized as a single graphite structure if they are continuous in three-dimensional observation.

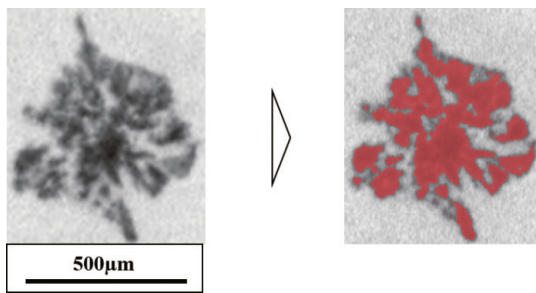


Fig. 2 Shape recognition by image processing

In addition, due to the limitation of the resolution with this system, it is not possible to perfectly extract the structure of the terminal fine graphite. Therefore, in this study, we decided to evaluate the type of graphite by relatively comparing graphite shapes using image processing under the same conditions.

3 Results and Discussion

3.1 Three-dimensional observation using X-ray CT

Fig. 3 shows the two-dimensional X, Y, and Z cross-sectional images read from an X-ray CT image of the medium-size TP-500. The spherical graphite structure surrounded by the dotted line in the Y cross-section is slightly out of shape but cannot be determined to be abnormal graphite structure. However, when the areas enclosed by the dotted lines in Fig. 3 are observed in the X- and Z-section, they are found to be chunky graphite. In two-dimensional structural observation of spheroidal graphite cast iron, the purpose is to investigate the graphite spheroidization ratio, graphite nodule count, and pearlite ratio to guarantee mechanical properties. However, in thick-walled spheroidal graphite cast irons as in this

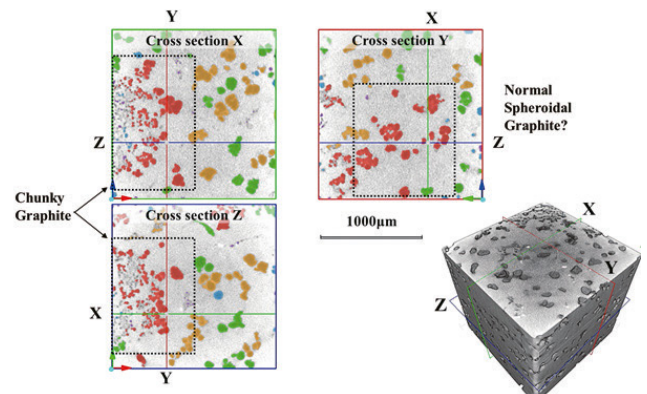


Fig. 3 Three-dimensional observation of abnormal graphite structures

study, it is difficult to grasp the complete picture of a graphite structure only by two-dimensional observation, as shown in the dotted line in the Y cross-section of Fig. 3, and there is a possibility an incorrect evaluation will be made.

Table 2 shows the graphite nodule count, graphite volume, and graphite volume ratio for each graphite grain diameter determined by three-dimensional observation which are inherent in each of the TP-300, TP-500, and TP-1500 test pieces. As the wall thickness increases and the eutectic solidification time increases from 12 ks to 20 ks, the graphite nodule count decreases from 1041 to 717 nodules/view and further decreases to 267 nodules/view at 47 ks. In Table 2, when focused on graphite with a grain diameter of 15 to 50 µm, the graphite nodule count increases from 14.7 to 60.3 as the TP size increases, but the ratio of graphite volume to the graphite nodule count in this range decreases from 1.2% to 0.4%. In previous studies by the authors, it has been confirmed the eutectic solidification time is less than 1 ks and most of the graphite grain diameters are 50 µm or less for small separately cast test pieces with

Specimen name		TP-300	TP-500	TP-1500
Eutectic solidification Time (ks)		12	20	47
Nodule count (n/view)		1041	717	267
Nodule count ratio of each size (%) (n/view)	15-50 µm	14.7 (153/1041)	50.3 (361/717)	60.3 (161/267)
	50-100	62.9 (654/1041)	24.4 (175/717)	20.6 (55/267)
	100-200	22.2 (231/1041)	21.2 (152/717)	10.2 (27/267)
	200-300	0.2 (2/1041)	3.8 (27/717)	5.2 (14/267)
	300-1000	0.0 (0/1041)	0.4 (3/717)	3.8 (10/267)
Graphite volume (mm ³)		0.43	0.78	0.68
Graphite volume ratio (%)		7.9	14.4	12.6
Graphite volume ratio of each size (%)	15-50 µm	1.2 (0.005/0.430)	0.9 (0.007/0.780)	0.4 (0.003/0.680)
	50-100	40.3 (0.173/0.430)	5.2 (0.406/0.780)	1.5 (0.102/0.680)
	100-200	56.2 (0.242/0.430)	29.3 (0.229/0.780)	7.4 (0.050/0.680)
	200-300	2.3 (0.098/0.430)	26.1 (0.203/0.780)	13.6 (0.092/0.680)
	300-1000	0	38.5 (0.300/0.780)	77.1 (0.524/0.680)

Table 2 Nodule count and volume of graphite structures

25 mm dia. x 250 mm (JIS G 5502 knock-off type) and 100 x 100 x 500 mm test pieces.⁴⁾ From this, it can be inferred the graphite grain diameter increases as the eutectic solidification time increases.

Table 2 shows graphite with a grain diameter of 50 to 200 μm is predominant when the eutectic solidification time is 12 ks, graphite with a grain diameter of 100 μm or larger is predominant when the eutectic solidification time is 20 ks, and graphite with a grain diameter of 300 to 1000 μm is predominant when the eutectic solidification time is 47 ks. It has been reported the graphite grain diameter coarsens as the eutectic solidification time increases, resulting in chunky graphite⁷⁻⁹⁾. Similarly for the graphite structures in this report, the relationship between coarsening of graphite structures and chunky graphite is established, and some of the structures of graphite with a graphite grain diameter of 200 to 300 μm and the graphite structures classified as 300 to 1000 μm are chunky graphite.

Fig. 4 shows the relationship between graphite volume and graphite nodule count for each eutectic solidification time, which represents the detail of the data presented in Table 2, along with the

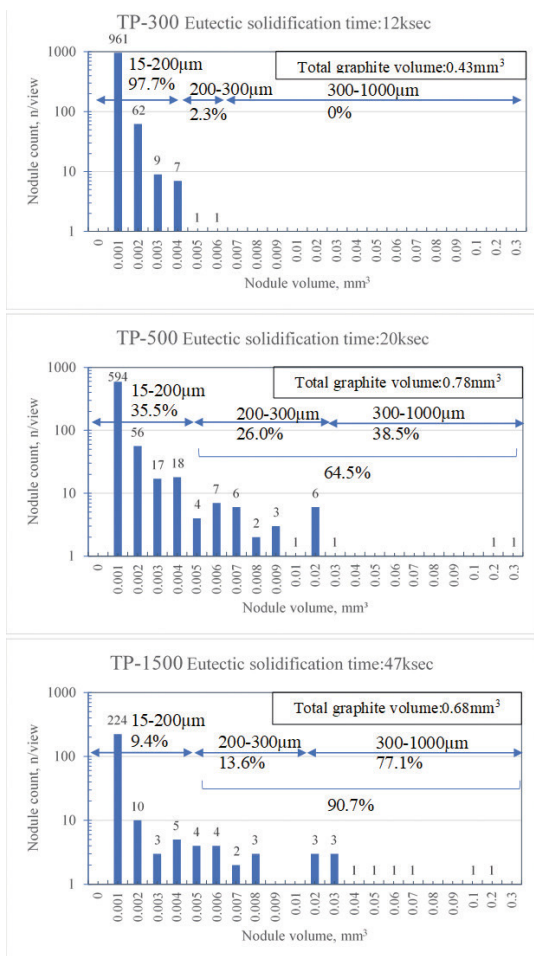


Fig. 4 Eutectic solidification time and graphite volume distribution

corresponding graphite grain diameters. At a eutectic solidification time of 12 ks, the volume ratio of graphite with a graphite grain diameter of 15 to 200 μm accounts for 97.7%. The volume ratio of graphite with a graphite grain diameter of 200 μm or larger is only 2.3%, and there is no graphite with a graphite grain diameter of 300 to 1000 μm .

Similarly, Table 2 and Fig. 4 show there are only three graphite nodules of coarse graphite with a graphite grain diameter of 300 to 1000 μm at a eutectic solidification time of 20 ks. However, the volume of graphite with a graphite grain diameter of 300 to 1000 μm accounts for 38.5% of the total graphite volume. Also, the graphite with a graphite grain diameter of 200 μm or larger accounts for as many as 64.5% of the total volume of graphite.

At a eutectic solidification time of 47 ks, graphite with a grain diameter of 300 to 1000 μm accounts for as many as 77.1% of the total graphite volume, and graphite with a grain diameter of 200 μm or larger accounts for 90.7%. As the eutectic solidification time increases, the volume ratio of graphite with a grain diameter of 200 μm or larger increases to 2.3%, 64.5%, and 90.7%. This indicates as the eutectic solidification time increases, the number of graphite nodules decreases and the volume of coarse graphite increases. In other words, the longer the solidification time, the larger the volume of a single coarse graphite nodule.

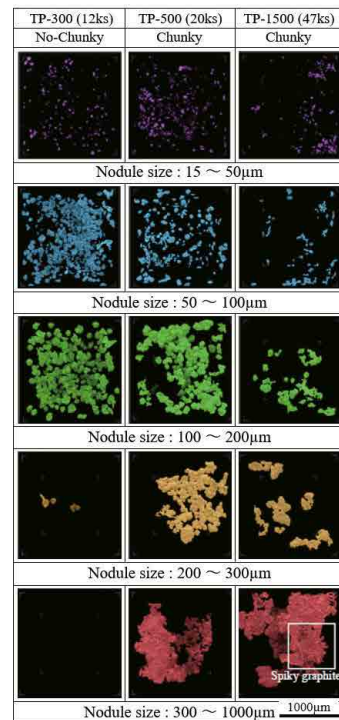


Fig. 5 Comparison of three-dimensional graphite structures by graphite grain diameter

Fig. 5 shows an image of the three-dimensional graphite structure classified by graphite grain diameter. Small graphite with a graphite grain diameter of 15 to 50 μm is uniformly distributed at a eutectic solidification time of 12 ks, while at 20 ks and 47 ks, small graphite crystallizes in the vicinity of coarse graphite with a grain diameter of 300 to 1000 μm . The graphite shape is mainly spherical at a eutectic solidification time of 12 ks, but the graphite becomes less spherical when the eutectic solidification time is 20 ks and 47 ks.

For graphite grain diameters of 50 to 100 μm and 100 to 200 μm , it can be confirmed the graphite is predominantly spherical at a eutectic solidification time of 12 ks. However, it is found that, when the eutectic solidification time is 20 ks or 47 ks, spherical forms in graphite with complex shapes do not increase.

Coarse three-dimensional graphite structures with a graphite grain diameter of 200 to 300 μm or 300 to 1000 μm are almost nonexistent at a eutectic solidification time of 12 ks, and coarse, non-spherical graphite with complex shapes is observed at a eutectic solidification time of 20 ks and 47 ks.

The results of three-dimensional observation of the spiky graphite present at a eutectic solidification time of 47 ks are shown in Fig. 6. From the two-dimensional observation image, the structure of spiky graphite is inferred to be a bar-shaped graphite radially spread. However, the three-dimensional observation of the spiky graphite

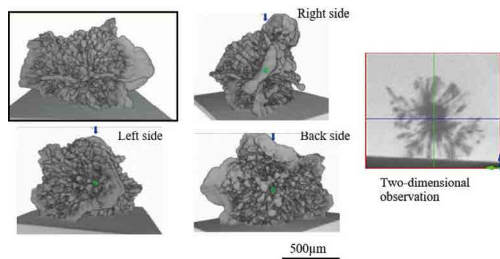


Fig. 6 Comparison of three-dimensional graphite structures of spiky graphite

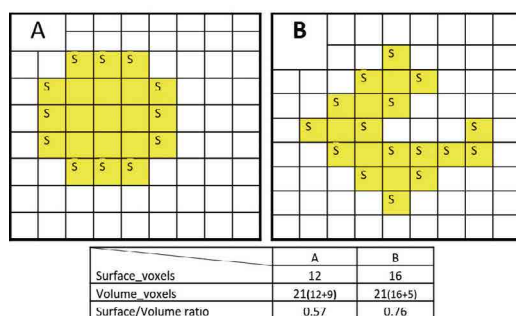


Fig. 7 Relationship between volume and surface area representing graphite shape

from the front, left, right, and back views shows the spiky graphite is composed of fragmentary and rod-shaped graphite shapes. This shows, while two-dimensional observation can only infer the shape from a single cross-section, three-dimensional observation allows a more accurate understanding of graphite structure.

Besides the qualitative evaluation through visualization as described above, the relationship between volume and surface area can be used as an effective means of evaluating graphite shapes in image analysis. Fig. 7 shows shape examples A and B, each of which consist of cubic three-dimensional pixels (voxels). B, in contrast to A, represents a complex shape. In figures A and B, their volume (Volume_voxels) is the same: 21, but their surface area (Surface_voxels) is different: 12 and 16, respectively. The "S" in the figure is the voxel in contact with the background, and the number of "S's" corresponds to the surface area. The number of "S's" combined with the number of voxels surrounded by the "S's" indicates the volume, as shown in the table in Fig. 7. The Surface/Volume ratio, which is the surface area (Surface_voxels) divided by the volume (Volume_voxels) for A and B, tends to be larger for B, which is a complex shape, than for A. When indicating the complexity of a shape in image analysis, referring to voxel often leads to obtaining results equivalent to a robust surface area. For this reason, a voxel-based shape evaluation method is used to evaluate graphite shape for each eutectic solidification time.

Fig. 8 shows the relationship between graphite volume and surface area for each eutectic solidification time. The plot in the Figure shows the distribution of surface area vs. volume of a graphite structure by voxel, and the solid line in the Figure indicates the relationship between surface area and volume of a spherical shape ($S = 4.835 V^{2/3}$). This solid line represents the ideal spherical curve. The graphite structure at a eutectic solidification time of 12 ks mainly consists of graphite having a spherical shape roughly consistent with the ideal spherical curve. At a eutectic solidification time of 20 ks, the surface area of the graphite structure is distributed above the ideal spherical curve, indicating the formation of a graphite structure with a large surface area relative to the volume and a complex shape. At a eutectic solidification time of 47 ks, the distribution of the surface area of the graphite structure is further above the ideal spherical shape curve than at 20 ks. The main cause of the deviation from the ideal spherical shape curve is the formation of graphite with complex shapes, including chunky and spiky graphite. The graphite grain diameter at which the relationship

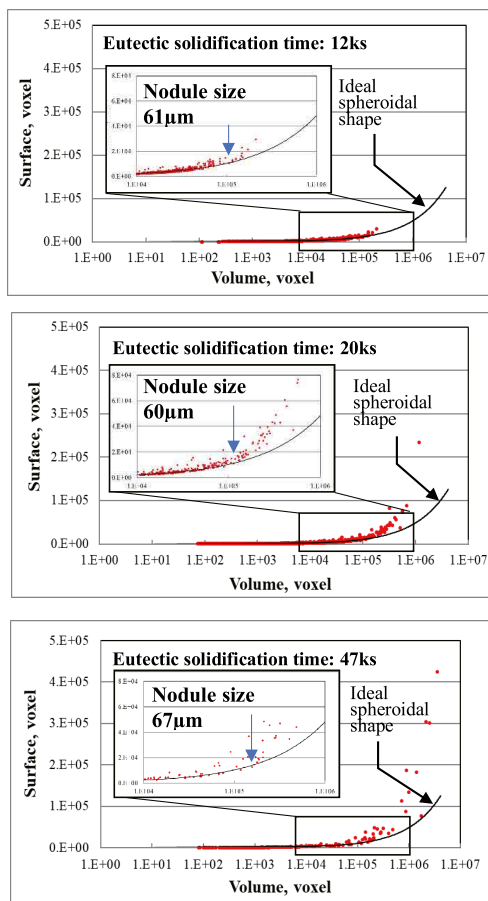


Fig. 8 Relationship between volume and surface area for each eutectic solidification time

between volume and surface area begins to deviate upward from the ideal spherical shape curve is 61 μm at 12 ks eutectic solidification time, 60 μm at 20 ks, and 67 μm at 47 ks. This indicates graphite is no longer spherical at a graphite grain diameter of 60 to 67 μm or more in the thick-walled castings in this experiment. Previously, the authors have confirmed the spherization ratio is 65% to 75% if the graphite grain diameter is 50 μm or more in two-dimensional structure observation using test pieces at a eutectic solidification time of 1 to 20 ks⁶⁾. This is generally consistent with the results in this report. Also, it would be possible to quantify the spheroidization state of graphite based on the relationship between the number of surface area elements and the number of volume elements of graphite to determine the presence of abnormal graphite such as chunky or spiky graphite and evaluate its mechanical properties.

4 Conclusion

We performed three-dimensional graphite structure observation of thick-walled spheroidal graphite cast iron by high-resolution X-ray CT and determined the following conclusions:

- 1) It was determined three-dimensional graphite structure observation of thick-walled spheroidal graphite cast iron by X-ray CT makes it possible to reveal complex graphite shapes and distribution, which are otherwise difficult to observe by two-dimensional observation.
- 2) It was determined coarse graphite increases as the eutectic solidification time increases and the volume ratio of the coarse graphite increases.
- 3) It was determined, using the relationship between surface area (Surface_voxels) and volume (Volume_voxels) of spherical graphite, complex graphite shapes begin to appear when the graphite grain diameter increases from 60 to 67 μm or more.

References

- 1) M.Tomizawa and H.Ookado: J. JFS 85(2013)900
- 2) N.Shiraki, K.Tanaka, A.Sugawara, R.Fujimoto, M.Tomizawa and T.Hara: J. JFS 91(2019)264
- 3) K.Sumizu, H.Toda, J-Y.Buffière, J.Lachambre, K.Uesugi and M.Kobayashi: J. JFS 86(2014)19
- 4) R.Fujimoto, M.Nakayama, I.Uemura: Report of the 168th JFS Meeting 168(2016)125
- 5) T.Hara: KENBIKYO 49(2014)53
- 6) R.Fujimoto: Doctoral theses of Iwate university (2014)
- 7) Y.Iwabuchi, H.Narita and Y.Ichinomiya: IMONO 59(1987)153
- 8) S.Kiguchi, M.Shintani, Y.Sumimoto and K.Nakamura: J. JFS 72(2000)311
- 9) O.Tsumura: J. JFS:76(2004)125

Application of a Surface Reforming Systems Using High-Speed Plasma Treatment to the Next Generation Printed Wiring Board Circuit Formation Process

Next generation high-speed communications have already started, and there is active development of data transmission technologies for realizing further acceleration. At the same time, there is a demand for highly integrated semiconductor package substrates used in data centers or the like because high-speed high-volume data processing through high-speed communications has become necessary. In this paper, we report on the development of the conductor layer formation process using a high-speed film formation system which can contribute to the fabrication of the fine patterned circuits required for achieving higher integration.



Kazuhiro FUKADA
Research & Development Center
Research & Development Department



Hiroyuki UEYAMA
Research & Development Center
Research & Development Department

1 Introduction

The high integration of semiconductor package substrates requires not only ultra-miniaturization of LSIs mounted on CPUs and GPUs but also formation of fine circuits of several micrometers width even on organic package substrates equipped with LSIs. For the miniaturization of organic substrate circuits, it is essential to form a conductor layer with high adhesion on the smooth surface of the insulating material. However, the conventional wet process does not allow adhesion to the smooth surface, making it difficult to form fine circuits. Our film forming system employs a vacuum-integrated process¹⁾, which enables surface treatment by plasma and conductor layer formation with high adhesion by sputtering under a medium-vacuum (100 Pa to 0.1 Pa) environment to achieve high-speed tact time.

In this report, we introduce adhesion evaluation and reliability evaluation by direct copper film deposition, and circuit fabrication evaluation by the semi-additive method as differentiating technologies.

2 Vacuum Film-forming System

This section describes plasma treatment employed in this system and the principles of sputtering¹⁾. The system is characterized by its ability to perform all processes in the medium vacuum range (100 Pa to 0.1 Pa). Plasma, which is said to be the fourth state of matter, is

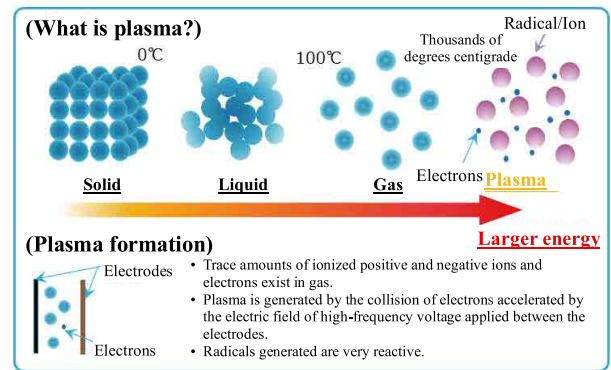


Fig. 1 Plasma treatment

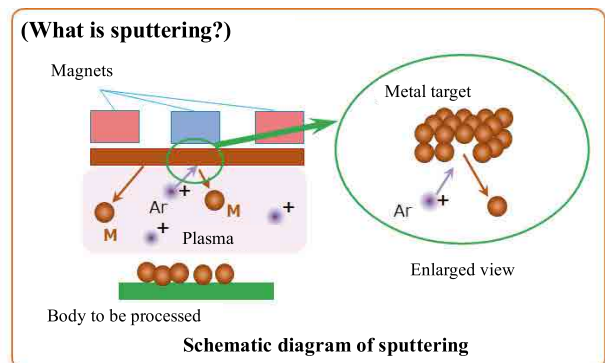


Fig. 2 Sputtering

generated by applying high-frequency power to the gas between electrodes to make electrons collide with gas molecules, as shown in Fig. 1. In plasma, highly reactive radicals are generated, enabling surface reforming of base materials and polymerized film forming of polymer material.

As shown in Fig. 2, in magnetron sputtering used in the film

forming system, metal (such as copper) to be film-formed is placed as the target in a vacuum chamber, a noble gas is cationized in plasma, and the target metal is repelled by collision with the target, thereby forming a film on the substrate surface facing the target.

3 Application to Printed Wiring Boards

3.1 Background of Development

Printed wiring boards on which CPUs, GPUs, etc. are mounted have a multilayer structure consisting of 10 or more layers of interlayer insulating film called build-up film. The wiring in each layer is formed by electrolytic plating. Currently, electroless plating is used to form conductive layers required for electrolytic plating. Adhesion of electroless plating to insulating materials is generally formed by physical anchoring with complex structures on the rough surface of insulating materials. However, fine patterned circuits require surface smoothness of insulating materials, and electroless plating can no longer provide sufficient adhesion, which greatly affects the reliability of substrates. In recent years, a conductor layer formation method using sputtering film deposition has been developed as a new method for next-generation package substrates²⁾. Compared to electroless plating, conductive layer formation using sputtering has a different adhesion system, and mainly uses chemical bonding through the generation of functional groups by plasma, enabling high adhesion to smooth surfaces. In addition, conductive layer formation using sputtering does not need the catalyst removal process required for electroless plating, which has the advantage of improving the yield rate in the subsequent process. In the general conductor layer formation process using sputtering, a two-layer metal structure in which a copper film is formed on an adhesive layer of Ti, Cr, etc. has been considered. However, the etching process for removing the conductor layer during circuit formation requires a removal process for the adhesive layer, which has many problems with the environmental impact and safety of the chemicals used. To solve this problem, we have developed a conductor layer formation process using the vacuum-integrated process¹⁾ and realized a highly adhesive direct copper conductor layer formation process that does not require a metallic adhesion layer by chemically bonding resin and copper through plasma treatment.

Since this process is performed in a medium-vacuum region, tact time is fast and no catalyst removal or metal adhesion layer removal

is required in the wiring process, which is suitable for miniaturization and advantageous for high-speed transmission characteristics. The following sections discuss the evaluation of adhesion to printed wiring board materials and the results of using the Semi-Additive Process (SAP) method to form a circuit having comb electrodes with $L/S = 15/15 \mu\text{m}$ on an Ajinomoto Build-up Film® (ABF) laminate substrate.

3.2 System Overview

We manufactured the LPP-450 high-speed vacuum surface-treatment film-forming machine as the system for forming a direct copper conductor layer and performed the processing described above. An external view of the system and the system specifications are shown in Fig. 3 and Table 1, respectively. The top view of the system is shown in Fig. 4.



Fig. 3 Sputtering system for reforming using plasma treatment

Outer dimensions	4,200 × 2,800 × 2,100 mm
Chamber volume	450 L
Substrate size	Max 630 × 540 mm
Sputtering method	DC magnetron method
Plasma method	RF remote Type
Deposition Rate (Cu)	~ 35nm/sec
Film thickness uniformity	<10% (max-min) / (2XAvg)
Tact time	240 sec (standard process)

Table 1 System specifications

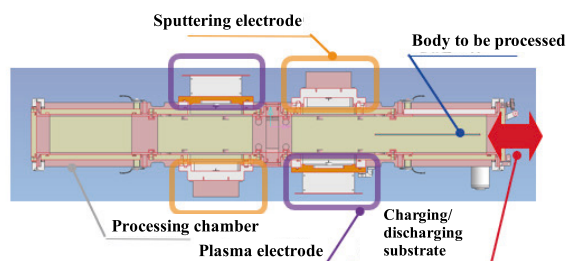


Fig. 4 System overview

[Processing steps]

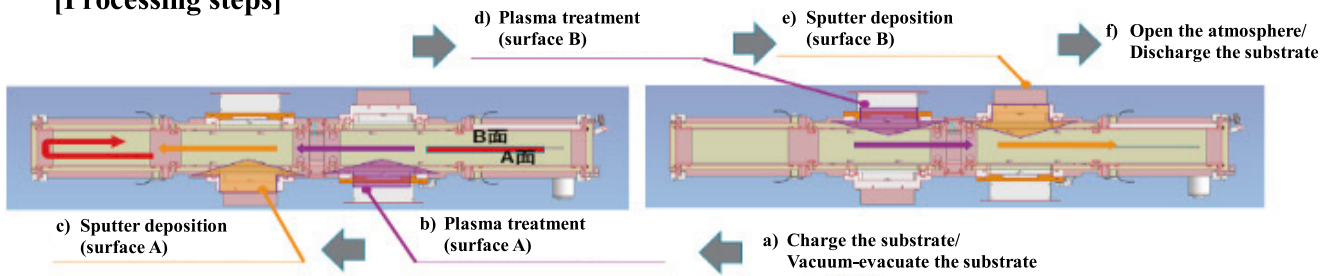


Fig. 5 Overview of processing steps

As shown in Fig. 4, the system consists of two plasma electrodes and two sputter electrodes, and is characterized by its ability to conduct surface treatment and deposit films on both sides of the printed wiring board material in a single vacuum treatment.

Fig. 5 shows the procedure for processing the printed wiring board by LPP-450. In Fig. 5, the first side to be treated (bottom side) is surface A and the second side to be treated (top side) is surface B.

- After charging the substrate, perform vacuum evacuation to a processable pressure of 0.1 Pa.
- Perform plasma treatment on surface A to reform it.
- Perform sputtering on surface A to form a Cu film.
- Switch the power supply and perform plasma treatment on surface B.
- Similarly, perform sputtering on surface B to form a Cu film.
- Open the atmosphere and remove the substrate.

Vacuum film-forming equipment usually needs to achieve to a high-vacuum range, and degassing takes place from the material when a resin substrate is vacuum-evacuated. For this reason, it takes a long time to reach the high-vacuum range. However, this process is conducted in a medium-vacuum region, which greatly reduces the exhaust time: processing can be completed in as little as 240 sec. per process. The maximum substrate size which can be processed by this system is 640 mm x 530 mm, which is the industry standard maximum size for printed wiring boards.

3.3 Method of Evaluation of Adhesion to Printed Wiring Board Materials

LPP-450 was used to evaluate adhesion with a direct copper conductor layer. A conductor layer was deposited on a 50 mm square insulation material, and a 30 μm thick copper film was additionally formed by electrolytic plating and annealing. After annealing, the peel strength between the plated layer and the resin was measured using a peel strength tester. Fig. 6 shows an example of evaluation of the sample produced by the process shown below

and a measurement schematic. The measurement conditions were as follows: peel test with a pulling angle of 90°, pulling rate of 50 mm/min, and test width of 1 cm.

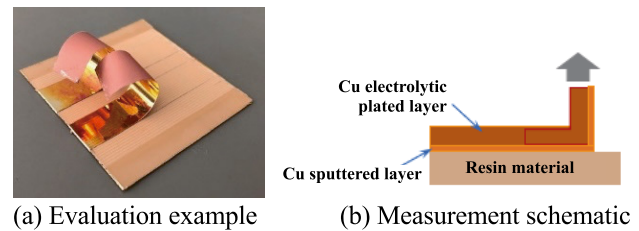


Fig. 6 Peel test evaluation example and measurement schematic

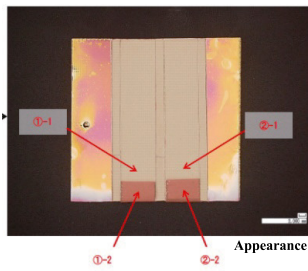
3.4 Results of Evaluation of Adhesion to Printed Wiring Board Materials

Material	Peel strength (N/cm)	Remarks
Build-up substrate material/ABF	4 ~	ABF reference data (GXT31)
Coating type polyimide	6 ~	Application to MPI materials to be considered
COP	6 ~	ZEONOR ZF16-100
Glass substrate	10 ~	EAGLE XG
Polyimide substrate	8 ~	Kapton V

Table 2 Results of peel strength measurement on printed wiring board materials

Table 2 shows the results of peel strength measurement on printed wiring board materials under the measurement conditions described in 3.3.

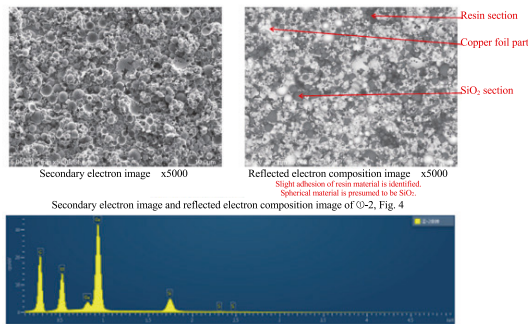
Patterning consists of processes including resist film lamination, exposure, development, conductive layer formation, electrolytic plating, and resist removal, and requires a peel strength of 4 N/cm or higher³⁾. Table 2 shows in the direct copper conductive layer formation process, a peel strength of 4 N/cm or higher is attained for the print circuit board materials which are considered for adoption in the next generation, indicating the wiring patterning process is feasible.



* Substrate size: 50 mm square, 0.8 mm thickness
Peel test width: 1 cm

Fig. 7 Substantive photograph of metal peel surface analysis after peel strength measurement

◆ SEM observation result (Q-2 Copper peel surface observation)



Secondary electron image and reflected electron composition image of Q-2, Fig. 4

Whole of Q-2	Line type	k ratio	mass%	mass% σ	Atom concentration %
C	K series	0.13993	21.89	0.11	49.10
O	K series	0.08878	10.34	0.06	17.41
Si	K series	0.08049	8.66	0.08	8.30
S	K series	0.00270	0.28	0.07	0.24
Cu	L series	0.46092	58.83	0.14	24.94
Total			100		100

Results of qualitative analysis by SEM-EDX (x5000, entire field of view)

Fig. 8 Analysis result after peeling off the metal surface of the plating seed layer

Fig. 7 shows the substantive diagram of metal peeled surface analysis after peel strength measurement, and Fig. 8 shows the results of metal peel surface analysis after peel strength measurement.

From the electron micrograph image shown in Fig. 8, resin adhesion can be observed on the metal side peeled surface, and the peeled surface was confirmed to be a cohesive breakdown in the resin substrate. In addition, elemental analysis using an energy-dispersive X-ray spectroscopy (EDX) also detected a large amount of C on the peeled surface, which suggested cohesive breakdown of the resin, confirming chemical bonding occurred at the resin-metal interface, so adhesion was attained by surface reforming using plasma treatment.

In order to confirm the effect of surface reforming, we plan to conduct chemical bonding analysis using X-ray photoelectron spectroscopy (XPS) to elucidate the adhesion mechanism between metal and resin, and to evaluate the adhesion strength of weak adhesive materials.

3.5 | Circuit Formation on Printed Wiring Boards

Next, the method of circuit fabrication by SAP (semi-additive process) using a direct copper conductor layer on an ABF build-up substrate is shown below. Fig. 9 shows the process flow. A desmear treatment was performed on an ABF substrate (GXT31) where FR-4 was used as the core material with permanganate and then dehydrated by oven heating. After that, LPP-450 was used to form a conductor layer (300 nm) by plasma surface treatment of ABF and copper sputtering. For patterning, dry resist film was applied using a vacuum laminator, exposed by the direct image method, and developed, and then electrolytic plating was performed to increase the film by 15 μm, followed by annealing, and finally circuit formation was performed by seed layer etching. For wiring evaluation, surface observation was performed using an optical microscope and cross-sectional shape observation using a laser microscope, followed by electrical reliability evaluation using the highly accelerated stress test (HAST) under high temperature and constant humidity.

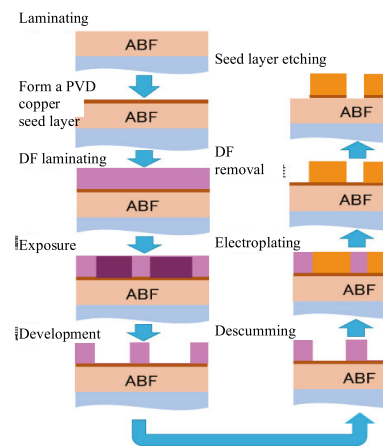


Fig. 9 Process flow of forming a circuit on a printed wiring board

3.6 | Results (Prototype Results and Performance Evaluation)

Fig. 10 shows a photograph of the surface after circuit fabrication and Fig. 11 shows a cross-sectional photograph by a laser microscope. From Figs. 10 and 11, it can be found that a comb-tooth pattern was formed without etching residue. Fig. 12 shows the results of electrical reliability evaluation of the reliability test (HAST test) at 85°C and 85%RH. When compared to a sample with the same pattern with a conductor layer made by electroless plating, the insulation resistance between the comb tooth pattern made by our film-forming system showed higher insulation resistance than that of the electroless plated conductor layer. These results indicate the direct copper conductive layer has adaptability to printed wiring board manufacturing methods.

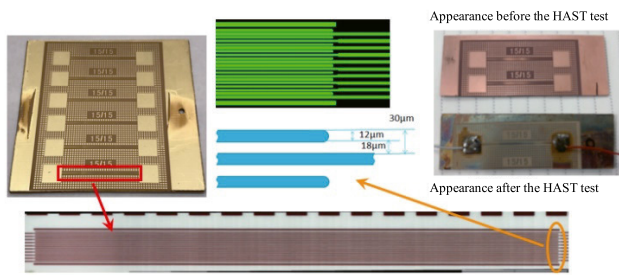


Fig. 10 Appearance after seed layer etching

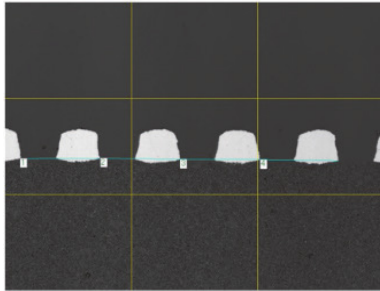


Fig. 11 Cross-sectional shape of wiring

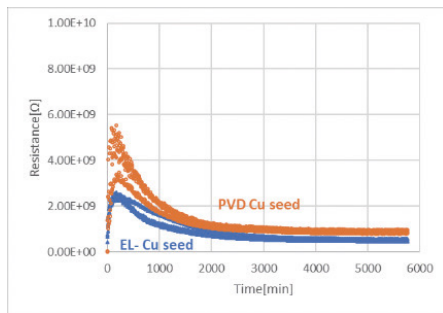


Fig. 12 Leakage current after HAST test

3.7 | Creation of Microcircuits on Mass-produced Substrates

Finally, we show the results of fabrication of a microcircuit with $LS = 5/5 \mu\text{m}$ on an ABF build-up substrate of 290 mm x 190 mm, which is close to the mass production size. The process flow is the same as in Fig. 9, and electrolytic plating of the wiring is done by increasing the film thickness by $5 \mu\text{m}$.

Fig. 13 shows the substantive photograph of the ABF substrate after microcircuit formation, and Fig. 14 shows the cross-sectional SEM image of the " $LS = 5/5 \mu\text{m}$ " section.

The circuit shown in Fig. 13 is formed with a periodic 3×2 pattern exposed in four shots. In the cross-sectional SEM image of the " $LS = 5/5 \mu\text{m}$ " section shown in Fig. 14, a good cross-sectional shape can be observed with no etching residue. From the above, it was confirmed the direct Cu conductor layer formed by our system is effective not only for small size substrates but also for normal size ones, and can be applied to fine wiring whose line & space is $10/10 \mu\text{m}$ or less.

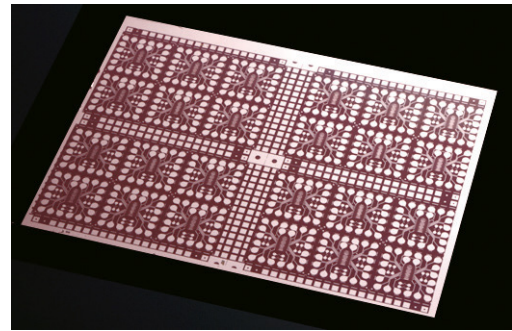


Fig. 13 Substantive photograph of microcircuit on ABF substrate



Fig. 14 Cross-sectional SEM image of the " $LS = 5/5 \mu\text{m}$ " section

4 Conclusion

We applied conductor layers by direct copper film deposition which were formed using the high-speed plasma surface processing system to the printed wiring board formation process and conducted a reliability test. The results confirmed the adaptability to circuit fabrication using the SAP method, which is used for package substrates. We are planning to expand the application to low-loss film materials and glass substrates as well as build-up substrates.

References

- 1) Fukada, Fukuyama, Namba, Kurihara, Sueki. Development of vacuum-integrated PVD+CVD deposition apparatus—Application to Al-SiO-NbO-based moisture-resistant multilayer reflective film for combiner-type HUD. Shibaura Machine Technical Report, vol. 28, 2021 13-16, 2021.
- 2) OH, Yoong, et al. Adhesion of sputter-deposited Cu/Ti film on plasma-treated polymer substrate. Thin Solid Films, 600: 90-97, 2016
- 3) SUN, Jiang-Yan, et al. Adhesion study between electroless seed layers and build-up dielectric film substrates. Journal of The Electrochemical Society, 160.3: D107, 2013.

Autonomization of Robots in the Stage of Transformation from Sustainability to Viability

The R&D Center, contracted by the New Energy and Industrial Technology Development Organization (NEDO), is developing an autonomous mobile work robot which supports various production activities in factories, in collaboration with Shizuoka University, Tokyo Metropolitan University, and Toyo University. In this report, we present the definition of the requirements for the system to which we conform and robot autonomy, and also present the concept of robot autonomy based on those requirements –maximization of viability – and the outline of the control which implements this philosophy and autonomizes robots. We also report the results of the initial stage of the tests which verify robot autonomy.



Yoichiro NAKAMURA

Research & Development Center
Research & Development Department



Yuya WADA

Research & Development Center
Research & Development Department

1 Introduction

Fig. 1 shows CONOID®, an autonomous mobile production support work robot under development. This robot has left and right arms (= articulated robot, manipulator) which manipulate work objects and an omni-directional traveling unit.

Such robots are called autonomous mobile robots (AMRs). Against the backdrop of a declining labor force, there is a growing need for automation of “mobile transport targeted by AMR, such as setting workpieces, supplying tooling to machine tools, and supplying reels to the automated reel warehouses of surface mount machines, plus handling tasks”, and mobile work robots equipped with manipulators on an AGV are also sold. However, their level of handling tasks is still limited to loading and unloading the materials to be transported. This is because the robot moves its arms only after stopping because the operator is focused on teaching the robot the appropriate stop position, and handling tasks while traveling is therefore difficult. In addition, when it becomes necessary to shift the robot body because the hand (i.e., end effector) cannot reach the target, not only does it become necessary to teach the manipulator, which is time-consuming, but the stop position of the robot body must be adjusted. This requires the operator to search for the desired stopping position of the robot body by guiding the robot arm to various locations, as in taking out parts in a cell production stall



Fig. 1 Dual-arm production support robot CONOID®-III

or replenishing goods in a convenience store. Also, moving the arms after stopping increases the work time.

In response to such current situations, AMRs with the following capabilities will be required in the future.

- ① Robot body travelling autonomously and follows hand movements, eliminating the need for teaching. Moreover, collisions between the robot body and its surroundings are autonomously avoided.
 - ② Hands and arms not only change the position of an object, but also perform sophisticated object manipulation where there is contact with the opponent side and an exchange of force occurs.
- To address these issues, behavior learning using deep learning,

which is representative of AI, has been attempted and the level of work is improving. On the other hand, the process of teaching and learning movements is time-consuming and movements are based on the playback of teaching and have not yet been optimized. In addition, recognition is mainly based on visual perception and the sense of force, which is necessary and effective for object manipulation, is neglected. From the perspective of industrial use, consistency with the framework of human cooperation and safety is also unclear. Furthermore, the working knowledge acquired by deep learning is limited to the same model of the robot.

By contrast, we do not rely solely on AI, but rather integrate advanced motion control technology, which is advancing just as rapidly as AI, with machine learning technology. In addition, we place the highest priority on speeding up on-site introduction of the robot and allow for rough teaching by the operator introducing the robot into the site. These approaches will enhance the autonomy of the robot and make practical use of AMRs which are easy to be introduced and have more advanced work capabilities.

2 Autonomization of Robot

2.1 | Significance of autonomization

The word "autonomous" is derived from the historical fact ancient Greek citizens governed themselves through legislation and has two roots from the Greek word: autos (meaning 'self') and nomos (meaning 'rule' or 'law')¹⁾. As these words suggest, autonomized robots are expected not only to act to achieve a defined goal, but also to infer and complement the range where human instructions cannot cover, and to generate and modify strategies of action by the robot itself in response to uncertainties and changes in the work environment. The challenge in providing autonomy to robots or the control system of machines is how to formulate these requirements and apply them to the control framework.

2.2 | Formulation of autonomy

Bourgine, a researcher in complex systems, extended the notion of viability domain in the viability theory²⁾ established by the mathematician Aubin and formulated the requirements for autonomous systems³⁾. We follow this requirements definition. The viability domain is the region in the state space of a control system where the system can stably perform a given function. Viability simply means survivability, but in the case of robots and machines,

it means continuity of work or activity, or continuity of function or operation.

Bourgine assumed the following equation must always be satisfied for an autonomous system to continue to function and maintain its existence or the significance of existence where f is the dynamics corresponding to the behavioral strategy of the autonomous system, s is the state, and $Viab$ is the viability domain.

$$\forall s \in Viab \quad f(s) \subset Viab \quad (1)$$

Accordingly, the next state which transitions as a result of executing f must also be included in the viability domain $Viab$ and must again be a state which can be safely manipulated by f . Although f is a kind of capability to build hypotheses, the state space handled by autonomous systems is wide and varied, so it is difficult to predict all $Viab$ and design f which satisfies equation (1) in any case. For this reason, we consider an autonomous system which interacts with the environment while hypothetically generating and executing f , and successively updates and learns the functions of f through this process. Denoting time as t , the metadynamics which update the dynamics f itself as g , and the autonomous system as $Unit(g, f, s)$, the adaptation process of the autonomous system to the environment through this functional update can be described as follows³⁾:

$$Unit(g, f, s)(t) \rightarrow Unit(g, f + \delta f, s)(t + 1) \quad (2)$$

δf is a newly acquired function of the autonomous system during the adaptation process. g is a function which allows the system to flexibly adapt to its environment, including generating new behavioral strategies, thereby increasing its viability.³⁾ This adaptive function is indeed the basic characteristic of autonomy described in the previous section.

From the above, the central issue in designing the control system of an autonomous robot is how to implement the dynamics f , which corresponds to the action strategy, and the metadynamics g , which corresponds to its adaptation strategy. As a practical response, we allow human interaction, and the motion of f is coarsely specified by humans through teaching or programs. We then adapt the trajectory and parameters of the motion to the work environment using the control laws described in Chapter 3 and a method under development for optimizing them by machine learning. We denote this process as g .

2.3 | Extending autonomy requirements

While in behavioral adaptation and learning it is necessary to generate new motions in some manner, we extend the autonomy requirement described in equation (2) for robots performing field work, as follows.

- The state space of the control system of an autonomous robot corresponds to the robot's viability domain $Viab$. Actions which lead the robot outside the viability domain must not be generated, and it is not necessary to generate actions corresponding to a state outside the viability domain.

In the case of a robot performing field work, deviation of the control state out of the viability domain in the form of an abnormal stop, should be avoided even in the trial phase of learning, since this would increase the danger with the number of trials and over time. Ensuring viability can be said to align the capabilities and safety of autonomous robots without contradiction. In addition, the property of keeping the control state in the viability domain facilitates teaching and learning.

3 Control Law Which Autonomizes Robot

In the lower layers of the control system of CONOID, the following two control laws are implemented to realize the philosophy of autonomy described so far.

3.1 | Solution of inverse kinematics with prioritized multiple targets

CONOID uses the solution of inverse kinematics with prioritized multiple targets^{4) 5)} devised by Sekiguchi and Takesue of Tokyo Metropolitan University, with whom we are collaborating, as the realization mechanism for the control system dynamics f described above. Fig. 2 shows its block diagram.

In general, inverse kinematics is a calculation method for finding the joint displacement which gives the positional posture of a hand tip of the manipulator, and analytical solutions exist for some representative configurations of both manipulators and traveling mechanisms. On the other hand, this solution is a numerical solution with iterative calculations which minimize the elastic energy of a virtual spring under the conditions where the joint displacement has a limited range of motion. The formulation is summarized below. For simplicity, we call the manipulator an arm and the end-effector a hand in some cases, and the respective translational position and rotational attitude angle of a hand tip and the traveling unit are

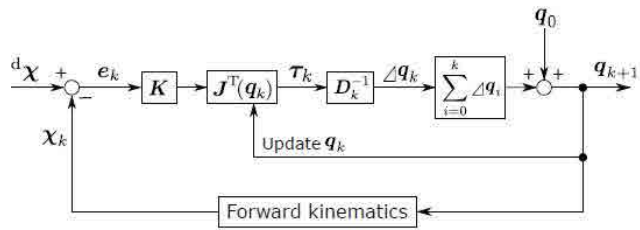


Fig. 2 Block diagram of the solution of inverse kinematics with prioritized multiple targets⁴⁾

collectively described as a pose, and the rotation angle of the output axis of the traveling unit is called joint displacement in the same way as an arm.

First, the respective current poses of the left/right hand tip and the traveling unit of CONOID has an error between the target pose and the current pose, and the error vector of those 18 degrees of freedom in total is denoted as $e(q_k)$ (even the 3 degrees of freedom of in-plane traveling is treated as 6 degrees of freedom). q is the joint displacement and k is the iteration step of the iterative calculation for the solution of inverse kinematics. Then, this numerical solution assumes there is a virtual spring between the current and target poses, and each joint receives a virtual torque from this virtual spring. The virtual spring coefficient matrix $K \in R^{18 \times 18}$ is a block diagonal matrix, and each diagonal block is the respective virtual spring coefficient diagonal matrixes of $R^{6 \times 6}$ of the left and right arms and the traveling unit. The virtual torque received by each joint from the virtual spring is given by the following equation:

$$\tau(q_k) = J^T(q_k) K e(q_k) \quad (3)$$

J is the Jacobian matrix. Assuming velocity is generated at each joint by damping from the virtual torque and the damping coefficient matrix is $D(q_k)$, the amount of change in joint displacement at time Δt between iteration steps is given by the following equation:

$$\Delta q_k = q_{k+1} - q_k = \Delta t D^{-1}(q_k) J^T(q_k) K e(q_k) \quad (4)$$

The joint displacement update law is then expressed by the following equation:

$$q_{k+1} = q_k + \Delta q_k \quad (5)$$

For $D(q_k)$, it needs to be set so the elastic energy of the virtual spring $D(q_k)$ expressed by

$$V_k = \frac{1}{2} e^T(q_k) K e(q_k) \quad (6)$$

will decrease, and a setting method is shown in Reference 5). In addition, the left and right arms and the traveling unit can be given priority in reaching their target pose. This is done by multiplying the respective matrices of the diagonal blocks of the arms and traveling,

which constitute the virtual spring coefficient matrix K , by a factor corresponding to the priority⁵.

Thus, this numerical method is a mathematical technique for solving a kind of optimization problem in which equation (6) is used as the evaluation function, and the displacements of each control axis to reach the respective target positions of the left/right arms and the traveling unit are collectively calculated according to the priority of reaching the target positions. CONOID has 4 motor drive axes in the omni-directional traveling unit and a total of 12 axes in the left and right arms. By changing the angle limit range of each axis and the target pose and priority of the left and right arms and the traveling unit, various cooperatively linked motions can be created between the arms and traveling. In particular, equations (3) and (4), which were not sufficiently emphasized in the original literature 4) and 5) because theoretical explanation was given for manipulators, play a very important role in these cooperatively linked motions. The role is that if the priority of the arm is set high and the priority of traveling is set low, traveling will prioritize the arrival of the arm's target pose over its own target pose and move in a coordinated manner to reduce the target pose error of the hand tip. This is because the virtual spring coefficient matrix K , which is multiplied by priority, is a diagonal matrix and has a zero correlation term, while the Jacobi matrix J^T has a non-zero correlation term, so that if, for example, the hand tip does not reach the target pose, its pose error will also affect the calculation of the displacement increment of the traveling in equation (4) via the correlation term in J^T .

In addition, this method for inverse kinematics has the following advantages over the usual method for inverse kinematics: 1) it can be applied regardless of the robot structure or the number of drive axes, 2) it can avoid deadlock caused by limited motion range of joint displacements, 3) it can set separate target positions for hands, legs, and traveling unit, and 4) even when there is no solution which satisfies all of the above, a compromise solution can be computed according to the priority^{4),5)}. The most important of these features is 5) it also has a kind of trajectory generation and motion planning capability, which can not only calculate joint displacements for a certain pose, but also sequentially calculate joint displacements for approaching a pose which is far away, in addition to near.

Therefore, the control system of a robot equipped with this method is equipped with a mechanism to draw the state of the arms and traveling unit into their respective target trajectories in a lower

fundamental part which is separate from the upper feedback control mechanism. This corresponds to the creation of an entrainment region^{Note1) Note2)} in the viability domain in the state space = the trajectory or attractor^{Note3)} corresponding to appropriate behavior. To maintain viability throughout the behavior, a mechanism to draw the state of the control system into the viability domain in this way is doubly or triply necessary. Chapter 4 examines these properties.

3.2 | Admittance control based on estimation of external force⁶⁾

This function is essential for sophisticated object manipulation involving contact. If the motion of the manipulated object is constrained like a fit, the manipulator will not be able to move as taught if the manipulator's motion is coarsely taught, and the manipulator will be subjected to excessive external forces. In such a case, this control law mitigates the external force after estimating the external force.

The general dynamics equation for manipulators is expressed by the following equation:

$$H(\theta)\ddot{\theta} + C(\theta, \dot{\theta})\dot{\theta} + g(\theta) + r(\dot{\theta}) = \tau_m - \tau_e \quad (7)$$

θ is the joint displacement, the first term of the left side of this equation is the inertia term, the second term is the centrifugal and Coriolis force term, the third term is the gravity term, the fourth term is the friction term, τ_m and τ_e of the right side is the motor torque and the external force torque, respectively. Assuming the manipulator is used at relatively low speeds and the effects of inertia, centrifugal force and Coriolis force are small (≈ 0), the external torque is estimated by the following equation:

Note 1 : Attractor: A region which has the property of attracting orbits in a state space of a dynamical system. Terms for Notes 1 to 3 are all for nonlinear dynamics.

Note 2 : Entrainment: A phenomenon in which nonlinear oscillating elements synchronize with each other. Entrainment includes the process in which a state is attracted to an attractor in a broad sense.

Note 3 : Entrainment region: That region in a state space of a dynamical system which is attracted to the attractor. This term is equivalent to the viability basin in the viability theory.

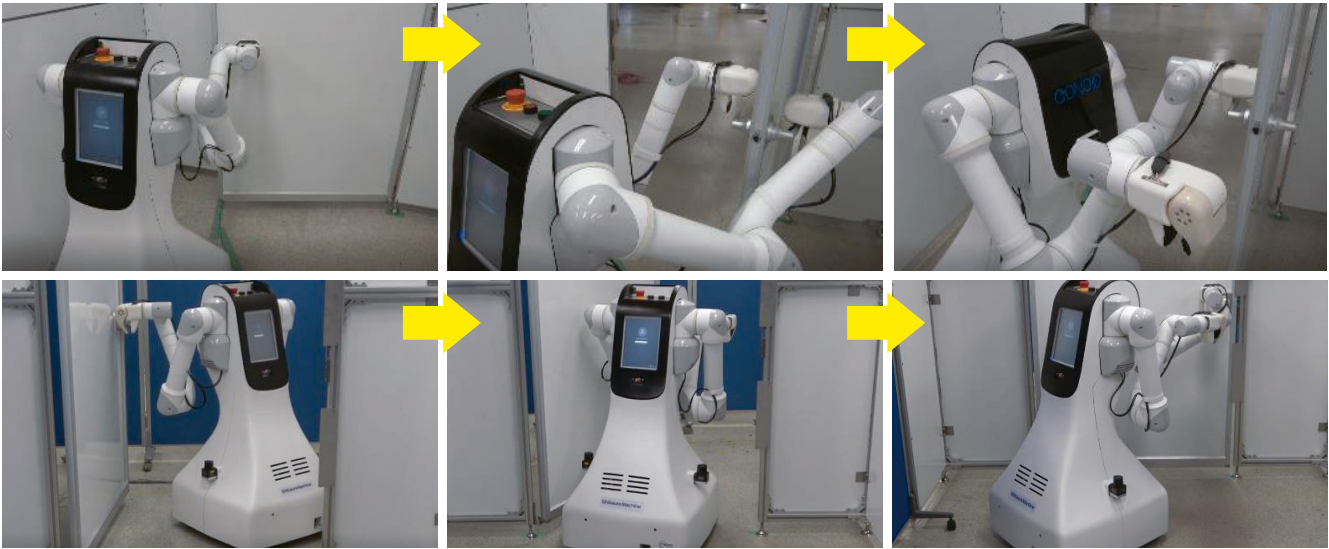


Fig. 3 Passing through a door by CONOID

$$\hat{\tau}_e = \tau_m - g(\theta) - r(\dot{\theta}) \quad (8)$$

The motor torque of the right side is detectable and the gravity and friction terms are determined from the physical quantity of the manipulator and the mechanical characteristics of the drive system. These constants are identified in advance. From this external force torque, the following equation is used to estimate the hand tip external force F_e without using force sensors.

$$F_e = J^{-T}(\theta)\hat{\tau}_e \quad (9)$$

$J(\theta)$ denotes the Jacobian matrix. Since the estimated value contains uncertainty, the value exceeding the threshold is taken as the hand tip-estimated external force \hat{F}_e .

This hand tip-estimated external force is used to perform admittance control^{7) 8)}. If a virtual spring mass damper system is set up at the manipulator's hand tip, the desired hand tip target position correction amount Δp follows the dynamics of the following equation:

$$\hat{F}_e = M\Delta\ddot{p} + D\Delta\dot{p} + K\Delta p \quad (10)$$

M represents inertia, D represents viscosity, and K represents elasticity.

4 Verification of autonomy requirements by door pass-through behavior

4.1 Significance of door pass-through behavior

Passing through doors by a robot is considered a difficult task to perform, has been tried for many years, and is still being tried today^{9) 10) 11)}. We are working on this task with CONOID, which is comparable to others, and it is currently possible to make robots pass through doors by teaching (Fig. 3). It should be emphasized

this behavior also requires traveling movements in accordance with hand movements, which is difficult to teach with conventional techniques, as described in Chapter 1. The reason we can teach the behavior is the traveling unit works autonomously without being taught by the aforementioned solution of inverse kinematics so the left and right hands which separately move both reach their respective target teaching positions.

In contrast to previous studies, this approach has the following points to differentiate:

- ① No model of work object, doors, and surrounding environment is required.
- ② No motion planning based on prior learning or simulation is made.
- ③ No special work teaching devices are needed.
- ④ Equipped with a function to optimize the movement trajectory (behavior learning function: under development).
- ⑤ For motion constraint, trajectory generation or teaching is not actively performed but is made to follow in a passive manner.
- ⑤ Of the utmost importance: in advanced object manipulations involving contact, where trajectory generation and teaching are difficult, it allows the possibility of reducing those issues. In the following sections we present the results of verifying the obedience to this motion constraint, which corresponds to a basic autonomy requirement, with a door-opening operation.

4.2 Verification of the followability of hands to motion constraints

For the motion of opening the door with the right hand we gave the robot the pose in which the right hand finished opening the

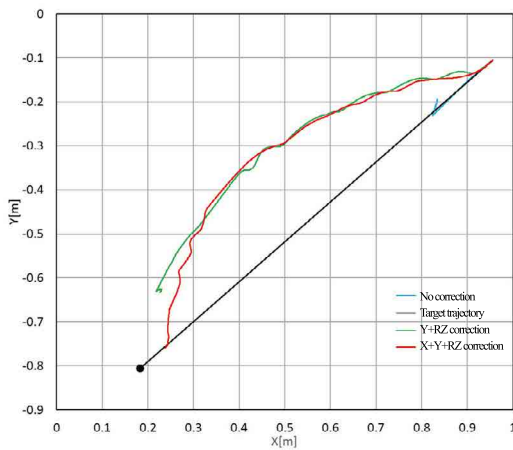


Fig. 4 Trajectory of the right hand moving the door handle

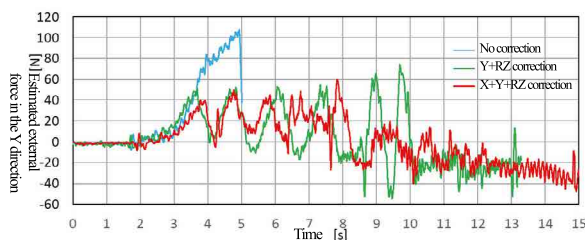


Fig 5 Difference in estimated external force in Y direction with and without admittance control

door as the target (end point) and taught the right arm to pull the door handle diagonally straight. We then verified whether admittance control could correct the robot motion to an arc-shaped orbit while suppressing the generation of excessive force. This followability corresponds to autonomy which compensates for coarse instruction. At the same time, we confirmed the changes in the right-hand trajectory with and without admittance control correction and in different correction directions.

First, the trajectory of the right hand which was moved while grasping the door handle is shown in Fig. 4. The black line is the target trajectory with the endpoint taught by the data. The right hand trajectory (light blue line) without admittance control correction stopped at a point about 0.1 m along the target trajectory (abnormal overload stop of the traveling unit). Next, when corrections were made to the rotation R_z around the Y and Z axes (green line), the trajectory was generally arc-shaped, but the door was not opened to the angle of the end point. By further correcting the X direction as well, the door was opened to the angle equivalent to the end point (red line).

Fig. 5 shows the estimated external force in the Y direction for the right hand corresponding to the right hand movement trajectory in Fig. 4.

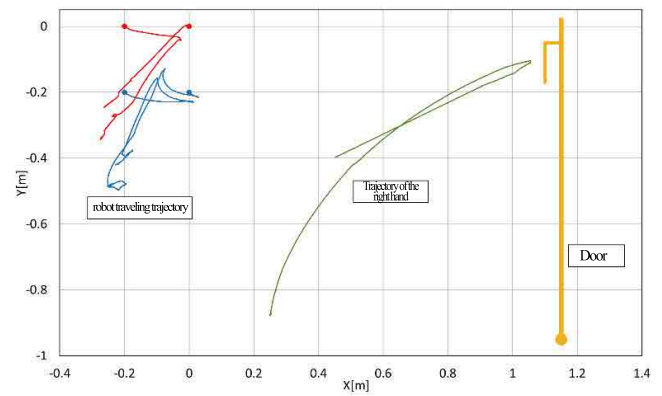


Fig. 6 Traveling trajectories from different starting positions

When there was no admittance control correction, an excessive force reaching 100 N was detected in the traveling unit at overload abnormal stop section around 5 s. This excessive force is considered to have given the traveling unit an overload which caused the abnormal stop. On the other hand, when the correction was applied in the X, Y, and R_z directions, the estimated external force was the smallest (red line) and was generally kept below ± 50 N. It can be seen that, to the coarse motion teaching to open the door by pulling it obliquely, the right hand motion followed the rotational motion constraint of the door and was attracted to the arc trajectory.

4.3 Verification of the followability of traveling to motion constraints

The teaching motion of the right hand which grips the door handle and then opens the door is started from four different robot body positions 0.2 m apart from each other. It is checked whether ¹⁾ the traveling of the robot body which started from different initial positions follows autonomously to the right hand which follows the rotational constraint of the door and ²⁾ it also converges to a constant trajectory. This corresponds to the autonomy in which the traveling of the robot body is attracted to a constant trajectory even without teaching.

Fig. 6 shows the results, showing the trajectory of the right hand grasping the door handle (one example, green line) and four examples of autonomously following trajectories of the robot body (red and blue lines). The latter shows the robot body which started moving from a position 0.2 m away in each of the X and Y directions eventually stopped with a spread of about 0.05 m in the X direction and about 0.24 m in the Y direction. The smaller this spread, the less effort the operator must expend to find the best position to start the operation with respect to the object to be operated (door). In addition, the deviation of the early state of the next door-opening pass-through operation becomes smaller, and teaching and learning

of the operation can be started regardless of the past operation history. However, the results at this time do not show a reduction in the Y-directional spread. The reason is the solution range of the traveling position is not narrowed down because the priority of the hand is increased in the inverse kinematics calculation described in section 3.1, while the priority of traveling which autonomously follows to the hand is lowered. Autonomous following of traveling is under continuous investigation, along with trajectory optimization, where this kind of contradiction will be resolved.

4.4 | Consideration of autonomy requirements

In Fig. 6, the two trajectories of the traveling of the robot body which started from $x = 0, y = 0$ (red) and $x = 0, y = -0.2$ (blue) show the robot body once moved forward toward the door, shown on the graph right side, and then moved to the lower left side of the graph. This is because the traveling of the robot body autonomously follows to the right arm without being taught so the right hand tip reaches the door handle even when the door opening motion is started from a position where the hand cannot reach the door handle even by reaching for it. In addition, looking at the two trajectories of traveling of the robot body (blue) which started moving from $y = -0.2$, both moved slightly to the upper left of the graph from around $x = 0$ before moving to the lower left of the graph. Similarly, this is because the traveling autonomously follows to the right arm so the motion of door opening by the right hand is established.

Thus, for the traveling of the robot body while the right hand grips the door handle and then opens the door, a non-programmed or unteaching movement is generated by the solution of inverse kinematics with prioritized multiple targets. In addition to the compensation for coarse teaching by following the motion constraints described in the previous sections, it can be concluded CONOID's control system should have fundamental autonomy.

On the other hand, CONOID aims to reduce the teaching time to 1/10th of that required by the conventional method. Although quantitative comparisons are difficult because some tasks, such as the door pass-through in this example, are difficult to teach with the conventional method, the current teaching time reduced is still only about 1/2 compared to the conventional method, subjectively and experientially. This is because, although the amount of teaching of target and intermediate poses has been reduced, conditions for admittance control and autonomous following of traveling remain

to be set. We are currently working on the automatic determination of these conditions as well and will report the results on another occasion.

5 Conclusion

We have described the concept of autonomy which maximizes the viability (=survivability) of CONOID, an autonomous mobile work robot under development and presented the results of the initial stage of the verification of autonomy. Using such autonomy as a core, we will commercialize CONOID not as a universal positioning device like conventional industrial robots, but as a work robot with a pre-installed execution program to perform specific tasks. For this purpose, we will conduct demonstration tests of the target tasks at customer sites.

Because of its life-related connotation "viability" has a stronger sense of identity and urgency than "sustainability". The viability theory, a multidisciplinary systems theory, has been applied to the respective analyses of climate change and resource management, and equations (1) and (2) apply to human behavior as well. People should act to the extent environmental conditions are within their own viability domain and should change their behavior pattern if there is a danger which threatens their survival.

In the case of a mechanical equipment manufacturer like us, improving the operational viability of products, that is, the continuity of operations and production, leads to higher productivity and less waste for customers through stable operations, which in turn leads to higher added-value for their products. This in turn increases the viability of our products in the market, or product life, and furthermore improves the viability of the manufacturing company itself. Based on this concept, we will develop this robot so, in addition to our company's existing dynamics f , with which products are manufactured and sold based on trust and stable profits are obtained, our efforts will become metadynamics g , with which the dynamics f will adapt to changes in the environment through originality.

Acknowledgements: This research was supported by the following projects by NEDO: "Development of Integration Technology as the Core of Next Generation Artificial Intelligence and Robotics", "Research and Development to Expand the Application Domain of Artificial Intelligence Technology", and "Reduction of

Period of On-site Installation of Production Support Robots and multi-capabilities thereof through Machine Learning".

References

- 1) L. Steels, When are robots intelligent autonomous agents?, *Robotics and Autonomous Systems*, Vol.15 (1995), pp.3-9.
- 2) J.P. Aubin, A.M. Bayen, P.S. Pierre, *Viability Theory: New Directions*, 2ns ed. (2011), Springer.
- 3) P. Bourgine and F. J. Varela, Toward a Practice of Autonomous Systems, F. J. Varela and P. Bourgine, eds., *Toward a Practice of Autonomous Systems* (1992), pp.xi-xvii, A Bradford Book, MIT Press.
- 4) M. Sekiguchi, N. Takesue, Stable Numerical Solution of Inverse Kinematics in Singular Posture and Unsolvable Problem Based on Minimization of Elastic Energy of Virtual Spring, *Journal of the Robotics Society of Japan*, vol.36, no.9 (2018) , pp.645-653. (in Japanese)
- 5) M. Sekiguchi and N. Takesue, Fast and Robust Solution of Inverse Kinematics with Prioritized Multiple Targets for Redundant Robots, *Advanced Robotics*, vol.34, no.16 (2020), pp.1068-1078,.
- 6) M. Nishimura, H. Shimizu, N. Takesue, Y. Wada, Y. Nakamura, Door Opening with Mobile Manipulator Using Force Estimation, *Lectures on Robotics and Mechatronics 2022, Collected Essays* (2022), 1A1-A07. (in Japanese)
- 7) N. Takesue, S. Nobata, H. Fujimoto, Admittance Control Method Achieving Stable Contact, *Journal of the Robotics Society of Japan*, vol.26, no.6 (2008), pp.635–642. (in Japanese)
- 8) H. Kaminaga, Control of Humanoid Robots and Actuators, *Journal of the Robotics Society of Japan*, vol.36, no.2 (2018), pp.128–133. (in Japanese)
- 9) K. Mizutani, S. Yuta, Research of Mobile Manipulator using Task-Oriented Approach, *Journal of the Robotics Society of Japan*, vol.17, no.6 (1999), pp.865–875. (in Japanese)
- 10) Y. Karayiannidis et al., An Adaptive Control Approach for Opening Doors and Drawers under Uncertainties, *IEEE Transactions on Robotics* 32(1) (2016), pp.1-15.
- 11) H. Ito, K. Yamamoto, H. Mori, T. Ogata, Efficient multitask learning with an embodied predictive model for door opening and entry with whole-body control, *Science Robotics*, 6 April, Vol 7, Issue 65 (2022).

Exploration of Foam Molding Technology to Improve the Functionality and Performance of Molded Products

Foam molding has already been put to practical use mainly to reduce the weight of automotive interior parts and to reduce material costs associated with weight reduction. It is now attracting renewed attention as efforts are increasing to apply to product design, enhancements of additional functions and performance such as thermal insulation and sound insulation provided by the foam layer. We have long been engaged in the development of foam molding technology to improve the quality of molded products mainly by using chemical foaming agents to realize finer and more uniform foam cells and enhance dimensional stability and other properties. In recent years, we have also been working on physical foam molding, which is expected to improve product recyclability and further increase the foaming ratio. More specifically, we have been developing technologies to enable physical foam molding to be applied in production of large physical foam molded automotive parts. In the following we report on the high-precision coreback molding technology we have developed and the characteristics of physical foam molding.



Ikuro TANAKA

Metal & Plastics Industrial
Machine Company
Metal & Plastics Industrial
Machine Technology
Department

1 Introduction

At present, in the face of the challenge of global warming, efforts to achieve a decarbonized (carbon neutral) society and the SDGs are gaining momentum. The automotive industry is undergoing digital transformation (DX) and CASE, which represents the trend of next-generation automotive, is attracting a lot of attention. CASE is a combination of the initial letters of 'Connected', 'Autonomous', 'Shared & Service', and 'Electric'. The 'Electric' related requirements include weight reduction to compensate for increase in battery mass resulting from more extensive electrification, thereby to achieve an adequate cruising range, and enhanced thermal insulation properties to reduce air conditioning energy consumption. Also, in various industries other than the automotive industry, enhancement of thermal insulation properties is attracting attention in terms of reducing energy consumption from the perspective of the SDGs. 'Connected' not only ensures a safe and comfortable means of transportation by using sensors to collect various information such as the vehicle status and surrounding traffic conditions but is also expected to provide an environment for enjoying entertainment such as music and video. Therefore, sound absorbency is required to

prevent interior sounds from reverberating, and sound insulation is required to keep exterior sounds, such as engine and motor noises, from penetrating into the vehicle interior space. Foam molding is a method to improve the functionality and performance required for parts of CASE vehicles. There are two types of foam molding: chemical foaming and physical foaming. Chemical foam molding involves adding a thermal decomposition type foaming agent to the base resin material, which means disposal of molded products requires they be treated as industrial waste depending on the type of foaming agent used. In contrast, physical foam molding uses nitrogen gas or carbon dioxide gas as the foaming agent, and therefore the resulting products are recyclable for reuse; an advantage over chemical foam molding in terms of both production and consumption. Another advantage of physical foaming is it can achieve a higher foaming ratio than chemical foaming by use of a higher supply gas pressure. With these advantages in mind, we are also developing technologies for physical foam molding. We are pleased to report we implemented a project to achieve large physical foam molded products using our high-precision coreback control technology and conducted performance evaluation of the technology.

As earlier mentioned, to address the challenges of the SDGs, efforts are being made to develop automotive parts and components which are light in weight and present enhanced thermal/sound insulation properties. An injection molding technology which is effective to achieve such automotive parts is a foam molding method involving coreback operation. In this molding method, the resin is filled into the mold when the cavity volume is small, and then the movable platen is made to retract (coreback operation) to enlarge the cavity volume whereby to accelerate the generation and growth of foam cells. In this way, it is possible to obtain a molded product having an internal foam layer, which cannot be formed in a solid product. However, with this method, variations in mold opening amount at the completion of coreback and behavior fluctuations during the coreback operation cause variations in the thickness dimension and foaming state of the molded product. Therefore, to obtain foam molded products of stable quality, it is necessary to eliminate all those factors associated with the structure of the mold clamping device which cause fluctuations in the mold opening amount and to optimize the coreback operation control to stably maintain an optimal foaming state. To solve these problems, we have developed a high-precision coreback control technology. The following describes the characteristics of the high-precision coreback control.

One of the factors associated with the structure of the mold clamping device which cause variations in the mold opening amount is variations in the coreback completion position due to clearance in the toggle mechanism (linkage), which can lead to poor foaming (Fig. 1a). The clearance counter device (patent No. 6608168) eliminates the control dead zone of the coreback operation (Fig. 2) and minimizes the range of variation in the mold opening amount at the completion of the coreback operation (Fig. 3). As a result, the actual coreback operation becomes a behavior which is close to the behavior represented by the theoretical value in the control, which enhances the repetition stability of coreback operation and thus enables a good foaming state to be created in a stable manner (Fig. 1b). In actual molding sessions, there occurs a difference between the set value and actual value of the mold opening amount due to changes over time in machine accuracy and wear, as well as disturbances such as temperature fluctuations. To compensate the actual mold opening amount, minute errors caused by changes

over time are determined using the linear scale (Fig. 3), and changes in mold thickness caused by temperature fluctuations and other disturbances are calculated from the fluctuating value of the actual mold clamping force (Fig. 4), respectively. In addition to accuracy enhancement enabled by the clearance counter device, limiting the adverse effects of changes over time and disturbances such as temperature fluctuations makes it possible to ensure good repetition stability in a precise manner.

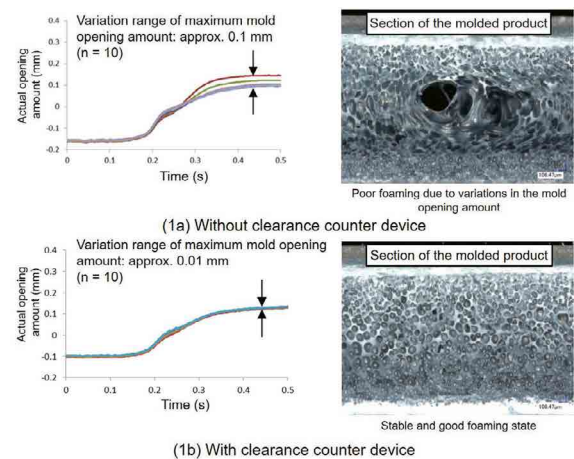


Fig. 1 Comparison of the mold opening amount variation range between without and with clearance counter device

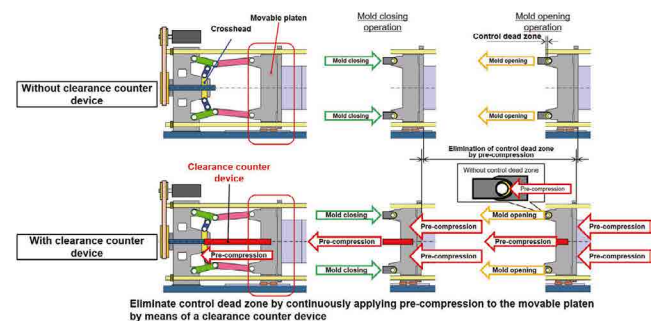


Fig. 2 Comparison of operation images between without or with clearance counter device

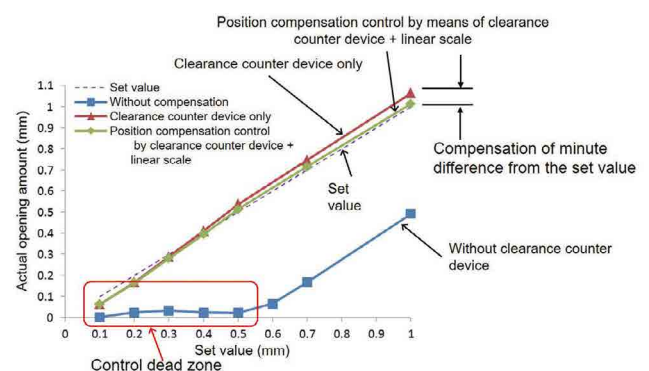


Fig. 3 Position compensation control for movable platen

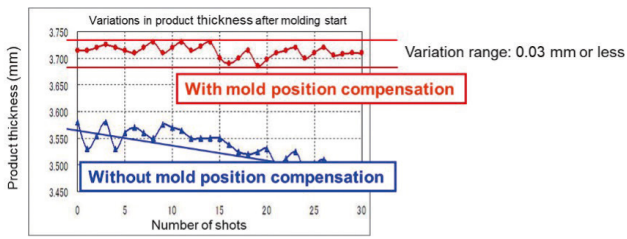


Fig. 4 Mold thickness position compensation control based on detection of actual mold clamping force

The mold clamping device with a toggle mechanism presents a curvilinear pattern of mold opening and closing speeds due to its mechanism characteristics. Therefore, setting the conditions to ensure a coreback speed appropriate for the growth rate of foam cells requires sufficient familiarity and experience. The movable platen constant speed control system (Patent No. 5872668) curvilinearly controls the crosshead speed pattern and performs constant speed control for the coreback operation to synchronize the foam cell growth rate and coreback speed (Fig. 5). This allows the formation of a uniform foam layer and simplifies the setting of conditions. In addition, since rapid depressurization is effective for the generation of fine foam cells, the responsiveness is improved compared to the conventional control method to reduce the time required to reach the set coreback speed by 64%.

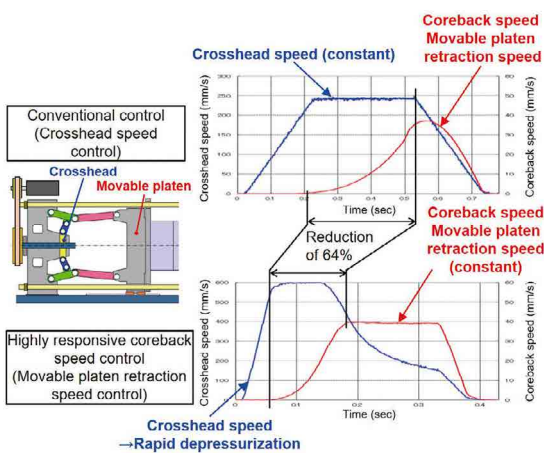
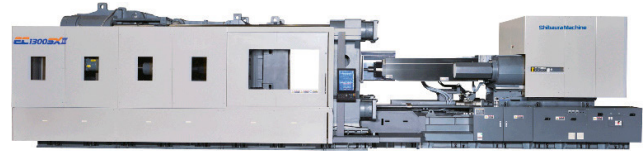


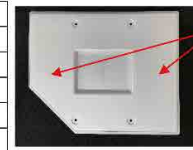
Fig. 5 Operation images of movable platen constant speed control

3 Application to large physical foam molded products

As an approach to physical foam molding of automotive parts, we implemented, together with Sankei Giken Kogyo Co., Ltd. - an automotive parts developer and manufacturer -, and Nippon Yuki Co., Ltd. - a plasticizer designer and manufacturer -, a project to develop a physical foam molding technology for realizing large



Molded product	Door module
Resin used	PP
Foaming agent	N ₂
Height	450 mm
Width	550 mm
Sheet thickness (solid)	1.8 mm



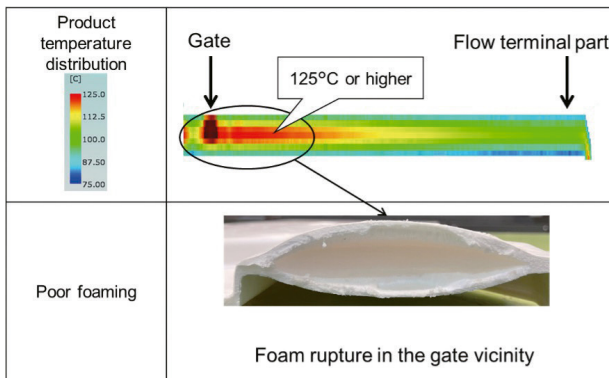
Gate (two locations)

Fig. 6 EC1300SX III and the large, molded product obtained

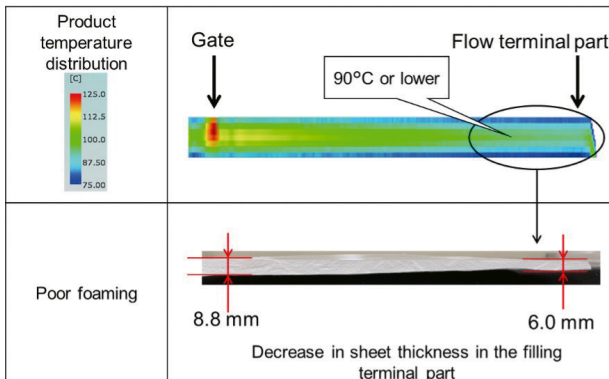
molded products with a high foaming ratio by applying "RIC-FOAM" developed by Maxell, Ltd. and Kyoto University. This project aimed to achieve foaming ratio of 5 or more using a plasticizing device with a screw diameter of $\phi 80$ mm or greater. Using our EC1300SX III ultra-large electric injection molding machine with a mold clamping force of 1,300 tons and physical foam molding technology including high-precision coreback control, we obtained a large, molded product (Fig. 6) achieving foaming ratio of 5 (plate thickness: 9.0 mm).

In the case of large, molded products, the temperature difference between the gate vicinity part and the filling terminal part increases due to the longer flow length from the gate part to the filling terminal part, shortening the time required for the entire resin mass to reach a temperature suitable for foaming. If the coreback start timing is early and the molten resin temperature of the foam layer is high, foam rupture occurs. Conversely, if the coreback start timing is late and the molten resin temperature of the foam layer is low, a decrease in the resulting plate thickness occurs due to insufficient foaming. Therefore, it is necessary to start coreback when the molten resin temperature drops down to a temperature within the range suitable for foaming. To bring the molten resin temperature to within the range suitable for foaming in actual molding sessions, a coreback delay time is set to adjust the coreback start timing. In the project to achieve large, molded products, it was confirmed insufficient foaming resulted when the coreback start timing was delayed by 0.6 seconds relative to the coreback condition (Fig. 7a) under which foam rupture had taken place (Fig. 7b). To resolve this problem, the coreback start timing was adjusted so the foam layer temperature was brought to within the range appropriate for foaming as shown in (Fig. 8), resulting in a molded product with uniform plate thickness (Fig. 9).

These results suggest the larger the size of the target product, the



(7a) When core back start timing is early



(7b) When core back start timing is late

Fig. 7 Types of poor foaming depending on the coreback start timing

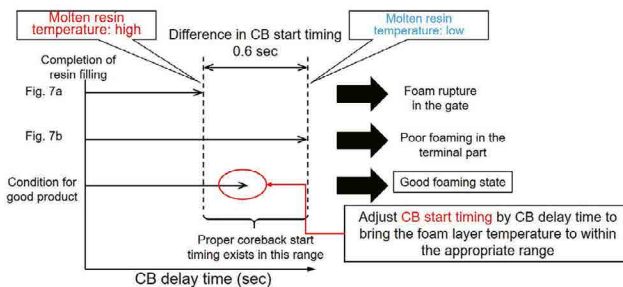


Fig. 8 Image of adjustment of coreback start timing



Fig. 9 Section of the molded product

greater the temperature difference between the gate vicinity part and the filling terminal part and the shorter the time for the resin temperature to become suitable for foaming, so it is necessary to adjust the coreback start timing in 0.1 second increments. In order to obtain a molded product not suffering poor foaming, coreback

must be initiated within this very narrow time frame, and high responsiveness and repetition stability of coreback are important. Electric injection molding machines are characterized by high-precision responsiveness and repetition stability thanks to servo motor drive. When combined with high-precision coreback control, they can produce large physical foam molded products in a stable manner.

4 Performance evaluation of physical foam molded products

Thermal conductivity measurements were performed to evaluate the thermal insulation properties of physical foam molded products. The measurements used polyethylene foam - a commercially available insulation material - as the reference sample and were taken on a total of five different samples: polyethylene foam, no coreback (no gas), no coreback (with gas), foaming ratio of 3, and foaming ratio of 5 (Fig. 10). The molded product sample with the second best insulation properties after polyethylene foam was a sample with foaming ratio of 5. The measurement results for this sample, together with the results for the sample with foaming ratio of 3, indicated the higher the foaming ratio, the better the thermal insulation properties. This indicates the increase in thickness of the foam layer associated with the higher foaming ratio effectively contributes to improvement of the thermal insulation properties. Although only thermal insulation properties were evaluated in this study, the new technology is also expected to achieve molded products with improved sound insulation properties.

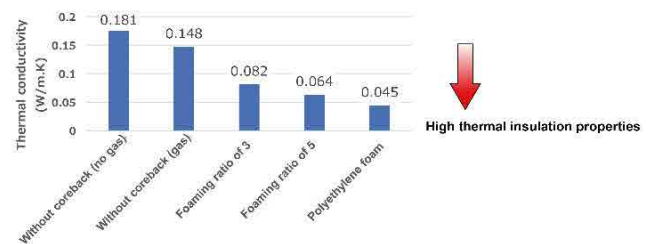


Fig. 10 Measurement results of thermal conductivity

5 Summary

Recently we developed a physical foam molding technology including high-precision coreback and intended to be used with the ultra-large electric injection molding machine EC1300SX III. In the process of developing this technology, it was confirmed high responsiveness and repetition stability of coreback operation are important to achieve a high foaming ratio and obtain satisfactory molded products. Enhancement of foaming ratio yields excellent thermal insulation properties similar to those of polyethylene foam, and this fact suggests foam molding can contribute to realization of molded products which have additional functions.

It has been more than 20 years since foam molding was first put to practical use, and meanwhile advances in molding technology have led to higher foaming ratio. Thus, foam molding is now expected to work as a new method to add new functions and performance to molded products. We are committed to making maximum use of the potentials of foam molding and developing molding technologies to realize higher value-added molded products, thereby contributing to our customers and society.

* "RIC-FOAM®" stands for "Resilient & Innovative Cellular Foam" injection foam molding technology. "RIC-FOAM®" is a registered trademark of Maxell, Ltd.

Column

Learning from Children



Yuki YAMAZAKI

Metal & Plastics Industrial
Machine Company
Metal & Plastics Industrial
Machine Technology Department

When I was a university student, I participated in a voluntary activity to engage with children. At one time, the children and I were trying to create a big boat using cardboard.

The children considered how to make it look real and suggested many different ideas to me. Thanks to those ideas, we finally completed a fine boat. I watched those children so enthusiastically communicating with each other and being totally engaged in what they really wanted to do.

After I graduated from university, I entered Shibaura Machine. On one occasion of conducting a durability test of half nuts, the test machine had some malfunction and automatic operation could not be started. When the machine was malfunctioning, die locking force was stronger than the force at the start of operation, which resulted in an abnormal locking force and the test machine

stopped. I periodically recorded the state of the driver in detail, including the driver temperature, cycle speed, and die locking force. Based on the information in those records, I analyzed why the malfunction occurred and how automatic operation could be started.

I guessed the die locking force was getting stronger due to expansion of the ball screw part because its temperature was increasing. I therefore created a mechanism to cool the high temperature portion and successfully eliminated the abnormal locking force. In this experience, I found it interesting to consider; how to solve a problem, propose a solution, and implement the solution. I felt a great sense of accomplishment when I was able to solve the problem.

Children and adults differ in many respects, such as perspective and responsibility. However, in doing my job, I try to respect the "power to actually do what you want to realize" as I learned from those children long ago.

Energy-Saving Measures for Die Casting Machines

Overview

Die casting is a manufacturing method widely used in the automotive industry. The automotive industry has been implementing measures to achieve carbon neutrality, and die casting systems must also adapt to this trend. This paper introduces energy-saving measures which can lead to carbon neutrality by die casting machines and their peripheral equipment.



Toshiaki TOYOSHIMA

Metal & Plastics Industrial Machine Company
Metal & Plastics Industrial Machine Technology Department

1 Introduction

Die casting is a manufacturing method which enables high-cycle, mass-production of castings with excellent dimensional accuracy. Since suitable strength and recyclable materials are selected, die casting is used in various fields, mainly in the automotive industry. With the recent global trend toward achieving carbon neutrality, the automotive industry is also aiming for carbon neutrality on a plant-by-plant basis. Therefore, manufacturers must also strive to achieve carbon neutrality in their die casting production facilities. Carbon neutrality means reducing the sum of greenhouse gas emissions minus absorption and removal to zero. This paper introduces several energy-saving measures from the standpoint of minimizing emissions in die casting production facilities.

2 Principles of Energy Saving Measures

Because die casting requires high output and high responsiveness, hydraulic drives are typically used for die casting machines. While hydraulic systems are compact and provide high power and high responsiveness, they have various energy losses as shown in Fig. 1.

There are also problems caused by inadequate hydraulic fluid management and fluid leaks. In contrast, electric drives are superior in terms of repetitive stability and energy efficiency, but in order to deliver the same output and responsiveness as hydraulic drives, increased size and costs are required, or there will be fields which are difficult to reach with the current base technologies. Therefore, we decided to examine a system which effectively uses both hydraulic

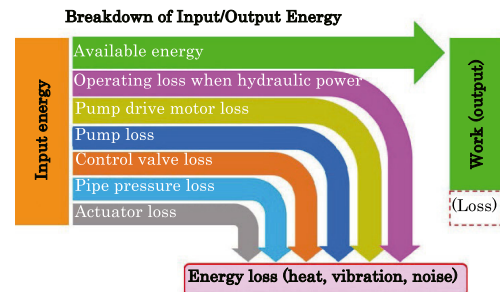


Fig. 1 Breakdown of Input/Output Energy in Hydraulic Systems

and electric power in the die casting process. In other words, in this system, hydraulic driving is limited to the moment of injection, extrusion, and core release, which require high output and high responsiveness, while other operations, such as mold opening and closing, are electrically driven. Each measure is described in section 3 to 6 from this standpoint.

3 Electric Clamping Die Casting Machine¹⁾

One of the reasons die casting is the method of choice for processing metal materials is its outstanding productivity. Although the die casting cycle time is determined by the casting system conditions of the entire production line, such as molds and peripheral equipment, and is not determined solely by die casting machine operation, as a die casting machine manufacturer, we believe it is important to pursue shorter dry cycle times.

Shibaura Machine has been releasing die casting machines with electric toggle die clamping for small and medium-sized machines since 2015, and developed the DC1100R-E (die clamping force:



Fig. 2 DC1300R-E Die Casting Machine

11,000 kN) and DC1300R-E (die clamping force: 13,000 kN) in 2020 by applying its expertise gained from these machines to large machines. Fig. 2 shows the appearance of the DC1300R-E. This development was based on the following three concepts.

- ① Shorter cycle time: The electric toggle die clamping mechanism provides outstanding productivity compared to conventional hydraulic toggle die clamping machines due to the speed of mold opening/closing and lapping operation with other processes.
- ② Space saving: A new design for the die clamping toggle unit has enabled significant space savings (reduced footprint) compared to conventional machines.
- ③ Less maintenance: Electric mechanism for minimizing hydraulic fluid leakage and equipped with the new TOSCAST-999 controller for outstanding ease of maintenance.

First, for achieving high cycles, the dry cycle time for the DC1100/1300R-E is shown in Fig. 3. To compare models, the DC1250CS3, a hydraulic toggle machine with a clamping force of 12500 kN, was used as the baseline machine. The electric toggle clamping mechanism significantly reduces the clamping and mold opening time, resulting in a cycle time more than about 30% shorter than the DC1250CS3 hydraulic clamping machine.

In many cases, when attempting to reduce the overall cycle time, the time required to fill the accumulator used in the injection section with hydraulic fluid becomes a bottleneck. Therefore, the capacity of the pump drive motor for the hydraulic fluid pressure source has been increased, and the oil discharge volume of the high-pressure line has been increased to shorten the hydraulic fluid filling time to the accumulator compared to conventional hydraulic toggle machines.

These modifications successfully reduced power usage per product.

While shortening the cycle time can be expected to improve molten metal flowing performance and casting pressure propagation because the mold temperature can rise more easily, there are also concerns about mold seizure and cracking. Consequently, a

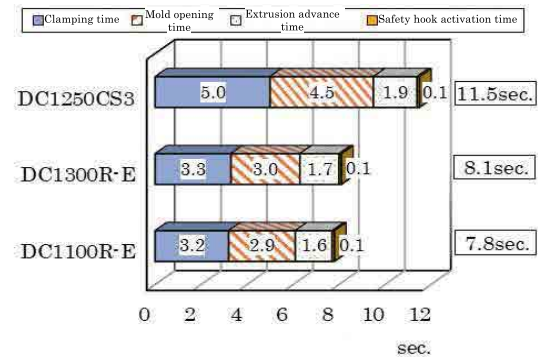


Fig. 3 Dry Cycle Time for the DC1100/1300R-E Dry Cycle Time

comprehensive measure focused on mold cooling methods is important.

Next, we will discuss space. The die size which can be mounted on a die casting machine depends on the die plate dimensions of the die casting machine. The die plate dimensions of the DC1300R-E are the same size as the DC1250CSW3, which is a conventional hydraulic die clamping wide-platen machine. On the other hand, when comparing the footprint (projection on a flat surface) for the DC1300R-E and DC1250CSW3, as shown in Fig. 4, the DC1300R-E has a smaller total machine length than the DC1250CSW3 (not including optional specifications), occupying less space. The reduced footprint can be effectively utilized, and the layout of the die casting line can be revamped when updating the machine. Similarly, a footprint comparison between the DC1100R-E and DC800R-EH is shown in

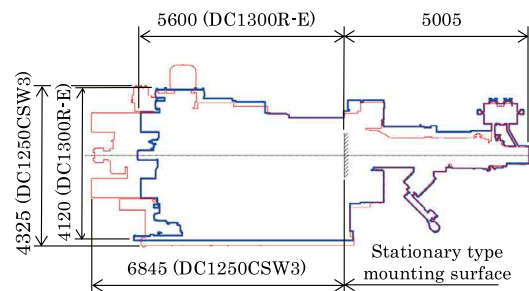


Fig. 4 Footprint Comparison between DC1300R-E and DC1250CSW3

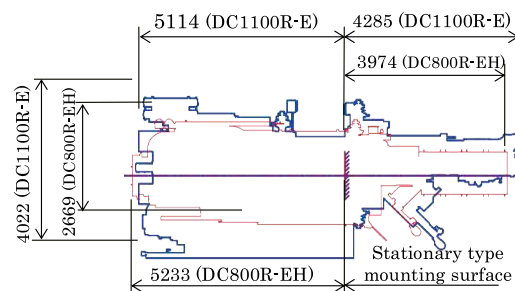


Fig. 5 Footprint Comparison between DC1100R-E and DC800R-EH

Fig. 5. Since they are almost the same size in terms of overall length, Shibaura Machine is considering installing them as update machines at locations where the 800-ton machines are currently installed to add support for larger products with higher profit margins than before.

Fig. 6 shows an outline drawing of the DC1100R-E clamping unit. The main components of the electric clamping unit consist of a servomotor, pulley, timing belt, and ball screw, which are identical to the components in the electric clamping units of small and medium-sized machines. The ball screw is located in the toggle section, and the reduced amount of required hydraulic fluid enables a more compact size for the hydraulic tank for improved accessibility and greater ease of maintenance around the frame hydraulic tank section.

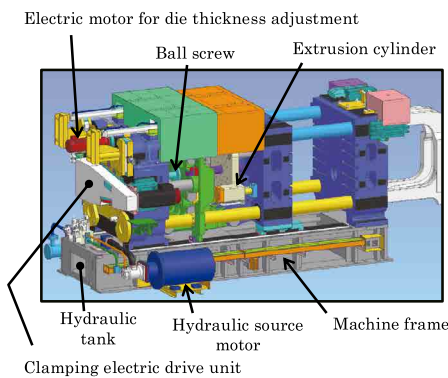


Fig. 6 Outline Drawing of DC1100R-E Clamping Unit

Also, this machine is equipped with the TOSCAST-999, which provides even more advanced functions than the conventional TOSCAST-888 controller. Ease of operation and visibility have been improved by integrating a larger monitor screen size (15 inches → 19 inches), a two-screen configuration, and additional injection waveform displays (5 → 8). Fig. 7 shows an example of the TOSCAST-999 monitor screen. The two-screen configuration enables the simultaneous display of real-time injection waveforms on the upper screen and injection settings on the lower screen. Injection settings can be changed while viewing the results on the injection waveform status display, eliminating the need to switch screens. Other features include an expanded centralized control function and a solenoid valve operation count to manage replacement scheduling for enhancing ease of maintenance.

Finally, to achieve energy savings, the electric toggle clamping mechanism and hydraulic system in this machine have been revamped for reducing its environmental impact compared to

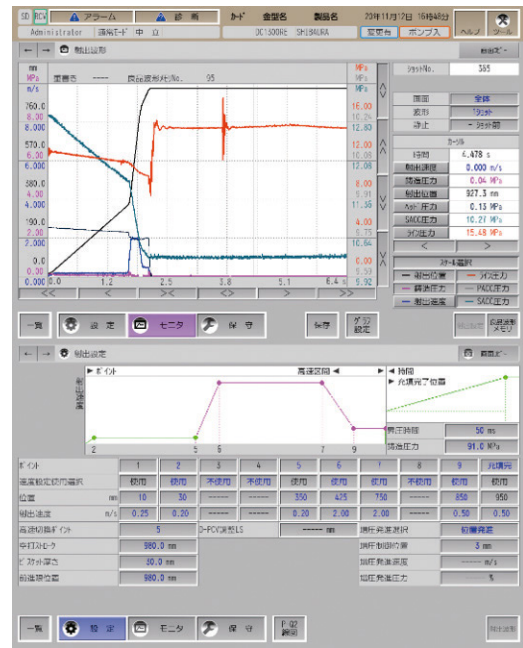


Fig. 7 Example of TOSCAST-999 Monitor Screen (Upper screen: Injection waveform, Lower screen: Injection settings)

hydraulic toggle machines. Fig. 8 shows the energy usage and CO₂ emissions per cycle for selected die casting machines. Note the conditions were set to 6 seconds for the ladling time, 18 seconds for the spray time, 5 seconds for the product take-out time, 100 mm for the extrusion stroke, and 10 seconds for the die timer. Electric toggle die clamping enables lap operation for mold opening/closing and core operation for shortening the cycle time. The DC1300R-E and DC1100R-E are expected to reduce their environmental impact per cycle by approximately 12% and 19%, respectively, compared to conventional hydraulic toggle machines. Also, by reducing the cycle time of die casting machines, the operation timing for peripheral equipment overall can be reviewed, which is expected to lead to even further reduced environmental impact.

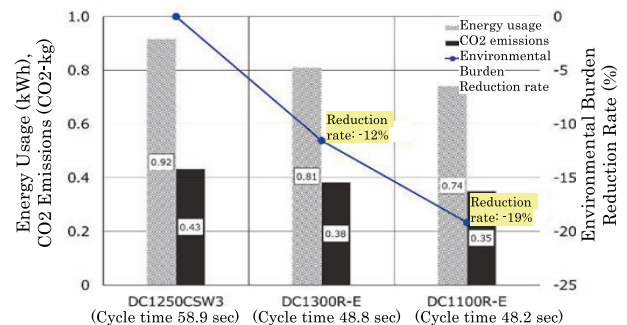


Fig. 8 Energy Usage and CO₂ Emissions per Cycle *Calculated assuming 1 kWh of energy usage generates 0.472 kg of CO₂.

4 Hybrid Core Device

Cores require high output power only during mold release, and other processes generally do not require high output power. Therefore, the hybrid core device is hydraulically driven during mold release only and is electrically driven for all other processes. As shown in Fig. 9, the basic structure consists of a servomotor, pulley, timing belt, and ball screw, and also includes a hydraulic cylinder used only for the initial core retraction movement. When the core is advanced, it is operated only by electric drive without using hydraulic power. When the core is released from the product after solidification, hydraulic drive is used, and after release, the machine switches to electric drive. Fig. 10 shows the appearance of a hybrid core drive converted from an existing hydraulic cylinder for a 1650-ton class mold. It is used by connecting a hydraulic hose (port on the core retraction side only) to the core port for each core system and by connecting the electrical wiring to the electrical box (outlet).

Fig. 11 shows an example comparing the hydraulic fluid usage amount for a hydraulic core cylinder and a hybrid core device in reciprocating motion. The hydraulic core cylinder conditions are a 52 mm rod diameter, 150 mm head diameter, and 110 mm core stroke. The hydraulic stroke of the hybrid core device was 20 mm. The amount of hydraulic fluid used by the hydraulic core cylinder

was 3.65 L while the hybrid core device used 0.32 L, which was a reduction of 91%.

Energy saving is discussed in section 7, along with other measures.

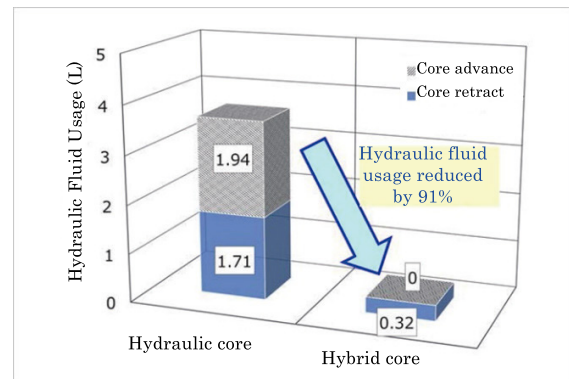


Fig. 11 Amount of Hydraulic Fluid Used by Hybrid Core Device

5 Hybrid Extrusion Device

A similar idea to the hybrid core device can also be applied to the extrusion device. Fig. 12 shows a description of the operation of a hybrid extrusion device. The hydraulic drive is used only during mold release for extrusion, which requires high output power while the other processes are electrically driven and utilize servomotors for mold opening and closing. First, from the mold clamping state in (1), the mold is electrically opened to the state shown in (2). Then, the extrusion cylinder (extrusion plate) cannot move to the open side of the mold from that position because the link housing acts as a stopper. Next, as shown in (3), hydraulic operation is used to extrude (release) by about 10 mm. After that, electric operation is used up to the extrusion limit as shown in (4). In the states (3) and (4), the extrusion cylinder does not move, and the moving die plate moves to the mold opening side to enable the extrusion operation. Finally, in the state in (5), the extrusion plate locking mechanism is used to clamp while locking to the extrusion cylinder housing to return to the extrusion cylinder. Fig. 13 shows the structure of the extrusion cylinder. This design allows an extrusion force identical to that of a conventional hydraulic machine while reducing the amount of hydraulic fluid used. Assuming 10 mm of the 100 mm stroke is hydraulically extruded (mold release), the hydraulic fluid usage per cycle would be reduced from 9.77 L to 0.41 L as shown in Fig. 14, which is a reduction of 96%.

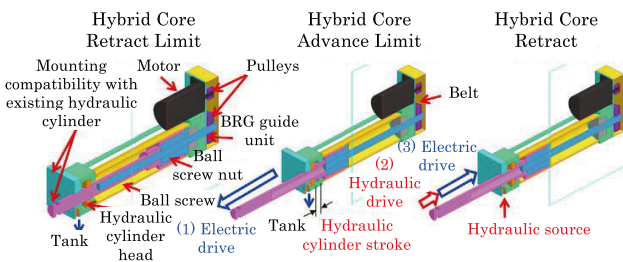


Fig. 9 Operation of the Hybrid Core Device

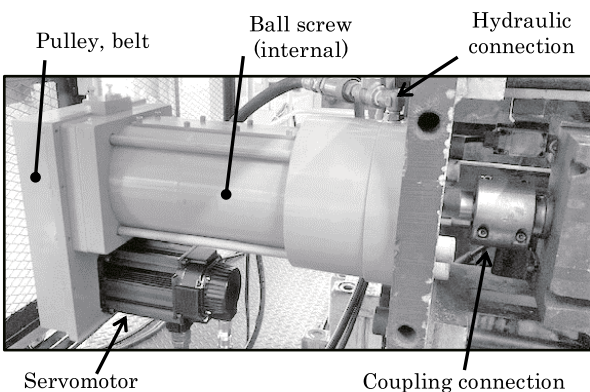


Fig. 10 Appearance of Hybrid Core Device

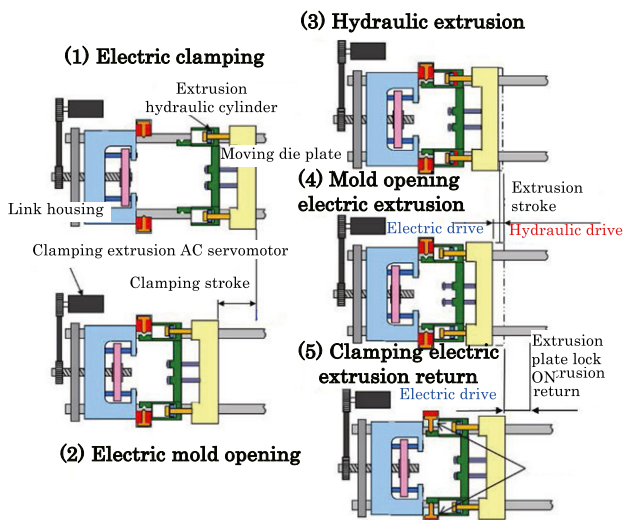


Fig. 12 Operation of Hybrid Extrusion Device

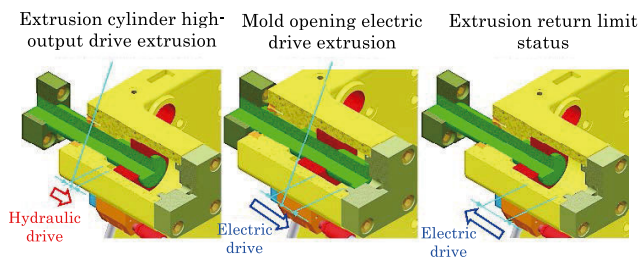


Fig. 13 Structure of Hybrid Extrusion Device

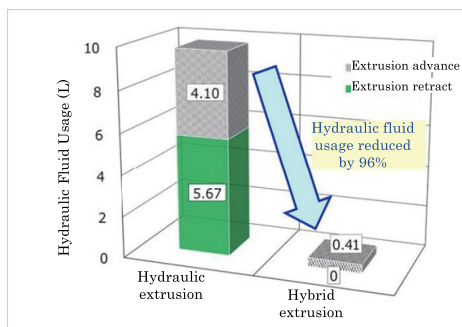


Fig. 14 Hydraulic Fluid Usage Amount by Hybrid Extrusion Device

6 Energy-saving Injection Device

Because injection devices require high output and high responsiveness, hydraulic drive using accumulators is considered best at this time. However, accumulator oil filled to high pressure is wasted in low output ranges such as low-speed injection sections. Consequently, a so-called run-around circuit, in which oil from the rod side of the injection cylinder is returned to the head side in the low output range, and a meter-out circuit in the high output range, in which molten metal is filled into the cavity, is being studied. Fig. 15 shows this concept and the hydraulic circuit. The C2G17 check

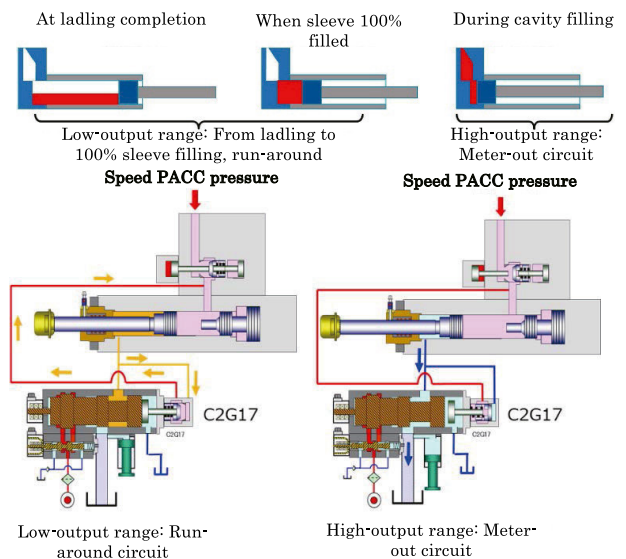


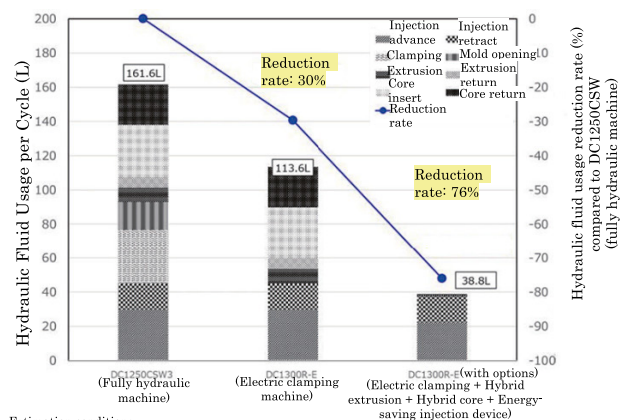
Fig. 15 Concept for Energy-saving Injection Device and Hydraulic Circuit

valve is the run-around switching valve, which is automatically switched by the injection cylinder pressure. The run-around circuit configuration allows for a 25-30% reduction in hydraulic fluid compared to conventional circuits.

7 Conclusion

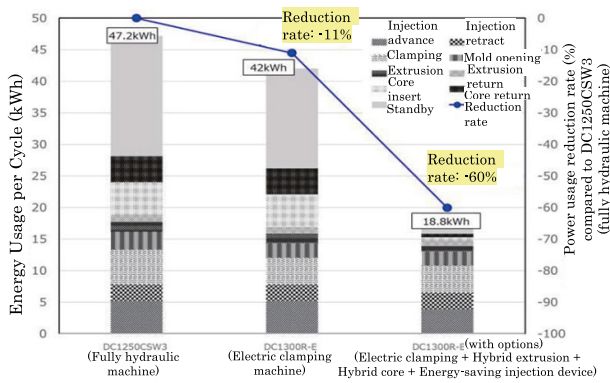
Figs. 16 and 17 show the estimated results under certain conditions for the effects of reducing hydraulic fluid and power usage when the measures described in Sections 4 to 6 are installed on the DC1300R-E electric die casting machine.

The bar graph on the right side shows a system equipped with energy-saving measures 4 to 6. Compared to the hydraulic machine on the left side, the amount of hydraulic fluid used is reduced by



Estimation conditions
 - The run-around circuit in the injection low-output range enables a molten metal sleeve filling rate of 50%
 - The extrusion ST has specifications of 150 mm full ST, and hybrid extrusion performs mold release at 10 mm
 - The core has 4-system specifications, and the hybrid core performs mold release at 10 mm

Fig. 16 Energy-saving Measure: Effect of Reduction in Hydraulic Fluid (Estimated)



Estimation conditions
 - Average load rate of hydraulic source motor was set at 80%, with 40% for standby power, and 60% for high-pressure hydraulic fluid, and these were converted for each work, and 60% of energy was assigned based on hydraulic fluid usage
 - The power factor for electric/hydraulic is taken into account for the power usage for electric clamping, hybrid extrusion, and hybrid core
 - Motor load operates at 50% during hybrid extrusion by mold opening/closing drive
 - Hydraulic source of energy-saving injection device is calculated using model with AC servomotor specifications

Fig. 17 Energy-saving Measure: Effect of Reduction in Power Usage (Estimated)

76% and the amount of electricity used is reduced by 60%, which is expected to result in significant energy savings.

8 Finally

Some of the energy-saving measures in die casting production systems were presented in the context of the global decarbonization trend. At the current stage, some of these measures are still in the concept or prototype stage, but we will continue to develop them so die castings will continue to have a place in society and can continue to contribute in the future.

References

- 1) Satoshi Tomioka: Kaiho Diecast No.154, p.53, (2021)

Approach to Implementing Digital Transformation in Twin-Screw Extruders

In recent years, it is essential for companies to implement digital transformation (or DX for short) to not only keep up with drastic changes in the business environment and the needs of customers and society but also gain superiority over competitors. In response to increasing demand for DX in the plastics industry, Shibaura Machine has been making enormous efforts to improve sensing technology for the implementation of DX in twin-screw extruders. In our experiment, we installed several kinds of sensors on some barrels of a twin-screw extruder, measured plastic behavior inside the extruder, and converted it to numbers. This technical report will introduce the sensing technology adopted to monitor the state inside the twin-screw extruder and the utilization of the data obtained from the experiment.



Yosuke OGINO
Metal & Plastics Industrial
Machine Company
Extrusion Machine
Engineering Department



Yasuhiro MAEKAWA
Metal & Plastics Industrial
Machine Company
Extrusion Machine
Engineering Department

1 Introduction

Today, plastics are used in a wide range of fields such as food packaging, medical equipment, electric appliances, automobiles, energy, and the environment. Many of these plastic materials (hereafter called resin) are manufactured using extruders. The Intermeshing, Co-Rotating Twin-Screw Extruder series, which Shibaura Machine manufactures and sells (hereafter called TEM), is used for compounding (or pelletizing composite resin), reactive extrusion, and sheet or film manufacturing.

TEM is capable of plasticating, kneading, and extruding resin by the action of shear arising from the two screws rotating inside the barrels and heat conveyed from the barrel heater. As Fig. 1 illustrates, the barrel and the screw are modular so their configurations can be flexibly changed depending on the application. In addition, the operating conditions of the TEM, including screw speed, barrel temperature, and the amount of resin charged, are widely adjustable and user-configurable as desired, to the extent permitted in the extrusion molding process. As a result, the TEM can run according to the properties of each resin and meet a wide variety of needs in the plastics industry.

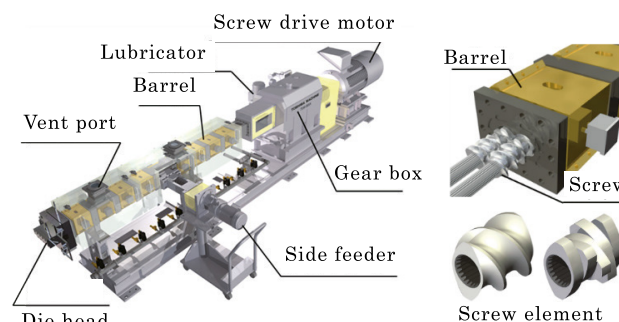


Fig. 1 Intermeshing, Co-Rotating TEM (left) Barrel and screw (right)

2 Background

Shibaura Machine uses several TEMs of its own to perform extrusion molding tests when requested by a customer or when verification is necessary. Resins used vary depending on the extrusion molding processes. Therefore, whenever performing an extrusion molding test, we carefully consider the configurations of the barrel and the screw and find the most suitable operating conditions for customer needs. TEM is configurable with an almost infinite combination of screws and barrels, particularly because these key components are modular. This makes it extremely difficult

to find the most appropriate configuration for each extrusion molding process.

In the past we often adopted a trial-and-error approach until we found the most appropriate configuration to satisfy customer quality requirements. However, in recent years we have strived to minimize the number of extrusion molding tests performed and the amount of raw material consumed for testing in order to reduce burdens on the customer. For this reason, it is an urgent necessity to establish a system to efficiently optimize the extrusion molding process with a limited amount of time and raw material.

3 TEM Extrusion Molding Test

In the planning phase of an extrusion molding test, a screw configuration is selected in view of the forms and properties of the resin to be used as well as the purpose of the test. Some screw configurations are selected based on the database Shibaura Machine has developed while others are worked out by our test staff from scratch. Table 1 shows you the characteristics of typical screw elements.






Appearance					
Function					
Shape	Screw-R Right-hand	Screw-L Left-hand	Disk-R Right-hand	Disk-N None	Disk-L Left-hand
Feed capacity	Forward	Reverse	Forward	None	Reverse
Fill ratio	Lowest	Highest	Low	High	High
Residence time	Shortest	Longest	Short	Long	Long
Action of shear	The action of shear varies depending on a combination of a screw and a disk.				

Table 1 Characteristics of screw elements

While there is a great variety of shapes and functions in screw elements, they can be broadly divided into two types: full-flight screw (hereafter called SC) and kneading disk (hereafter called KD). SC and KD are used for feeding and kneading resin, respectively. The inside of the extruder is a kind of ‘black box’ during extrusion molding. In other words, it is difficult to grasp the state of the resin fed inside. To begin with, our test staff considers changes in the resin inside the extruder from plastication to kneading and extrusion before determining an appropriate screw configuration. Next, our test staff plans a barrel configuration suitable for the determined screw configuration, arranges necessary attachments, and then determines a TEM test configuration. In addition, while performing an extrusion molding test, it is necessary to closely observe any

phenomenon occurring and adjust the operating conditions accordingly for steady operation.

The series of tasks as above described is often likely to rely heavily on the skills, experience, and instincts of individual test staff. As a consequence, this issue often hinders the optimization of the extrusion molding process and remains to be solved.

4 Efforts for the Implementation of DX

As above mentioned, effective use of the TEM to satisfy product quality demands required significant time and experience. However, as part of our DX implementation effort in TEM, Shibaura Machine has been striving to improve the sensing technology during extrusion molding and has recently achieved 2 major outcomes. First, the use of an analyzer system has made it possible to measure distribution of pressure in the resin flow direction. The analyzer system is designed to measure pressure and its change over time inside the TEM. Second, the use of an acoustic emission sensor (hereafter called AE sensor) has enabled us to understand plastic behavior inside the TEM. The AE sensor is used to detect acoustic emission (hereafter called AE), which is derived from the strain energy of a solid arising when resin is sheared and deformed. The next section will give you an overview of the sensing technology based on the analyzer system and the AE sensor.

5 TEM Sensing Technology

5.1 Analyzer System

The analyzer system is designed to measure pressure inside the TEM with the pressure sensors installed on some of the barrels, and

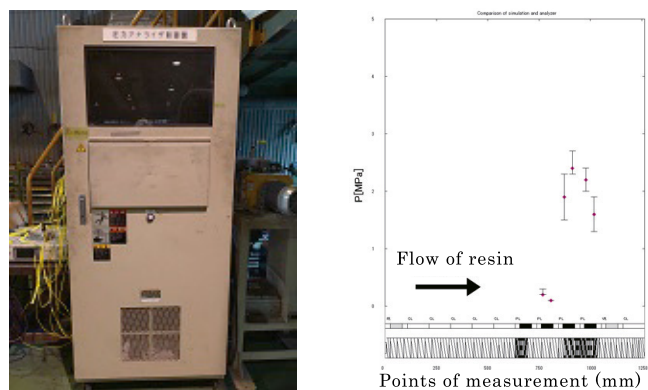


Fig. 2 Analyzer system (left)
Resin flow direction and pressure distribution display (right)

detect the rotation cycle and angle of the screws using the fiber sensor. The individual sensors are configured to send data to the PCI board via the amplifier.

Fig. 2 shows you the analyzer system and the display. Synchronizing the individual data collected from the pressure sensors and the fiber sensor for analysis enables us to examine how pressure in the rotational direction of the screw changes over time per screw rotation, as illustrated in Fig. 3. In addition, installing the pressure sensors on several barrels helps to examine the distribution of pressure in the resin flow direction in real time.¹⁾

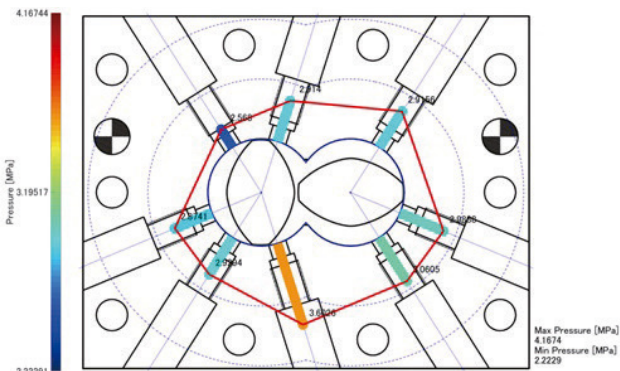


Fig. 3 Polar coordinate graph of pressure in the rotational direction of the screw¹⁾

5.2 | Sensing Technology Based on the AE Sensor

Through joint academic and industry research, Shibaura Machine has established a technique to continuously measure AE signals and monitor the state inside the TEM with the AE sensor installed thereon. This facilitates the detection of AE arising when pelletized resins are sheared and deformed by KD and eventually monitoring the state of the plasticized resin, which was difficult to do. In addition, we have built a system to conduct a real-time FFT analysis on AE signals during extrusion molding and accumulate signal strength data only within the corresponding frequency band.

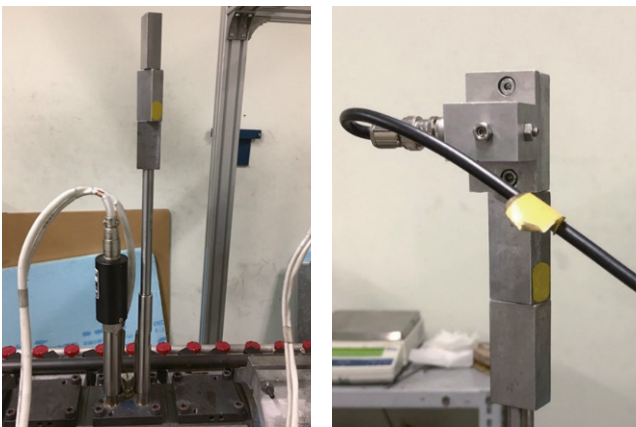


Fig. 4 AE sensor installed on the barrel

Thanks to this system, the state inside the TEM can be more accurately monitored.²⁾

Furthermore, we are working on predictive gear box maintenance using the AE sensor. The gear box is one of the more important components of the TEM. It employs a special reduction gear designed to distribute the power from the motor in the same direction. When a gear box unexpectedly fails, it takes enormous time and expense to recover from such failure, plus there is a significant impact on the customer's production plan. Traditionally, a fault diagnosis of a gear box was conducted in either the customer's daily inspection or regular inspection by our service department. To accurately diagnose a problem with components within a rotating unit, such as gears and bearings, we had to stop the extrusion molding process, disassemble the gear box, and then visually inspect.

To address such issues, our service department has developed its own gear box fault diagnosis technique. To be more specific, our service representatives visit a customer production site, apply the AE sensor directly to the gear box during the extrusion molding, measure the AE signals from inside the gear box, and then analyze them. This allows us to identify damage or wear to the gears or bearings early and perform predictive maintenance of the gear box without stopping extrusion molding. Consequently, our technique will contribute to the prevention of unexpected failure and the systematic maintenance of the equipment.

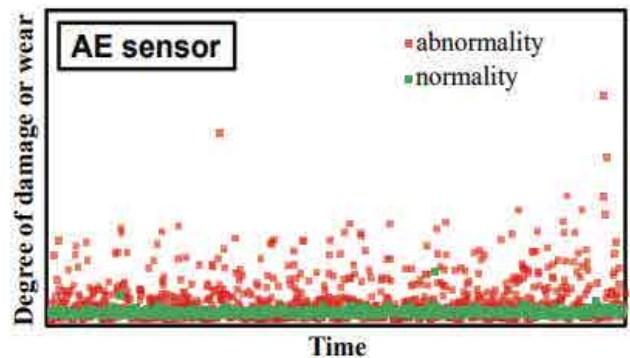


Fig. 5 When diagnosed as normal or abnormal in gear box fault diagnosis

6 | Verification

6.1 | Operating Conditions

The throughput (hereafter called Q) and screw speed (hereafter called N_s) of the TEM can be configured as desired. The strength of kneading resin inside the TEM can be adjusted by changing the Q

parameter and/or the N_s parameter. Fig. 6 illustrates the relationship among N_s , Q , and kneading strength.

In general, it is assumed as long as the throughput per rotation of the screw (hereafter called Q/N_s) is constant, the physical properties of the extruded resin remain equal. As N_s increases with Q kept constant, the kneading strength will be more likely to increase. In contrast, as N_s decreases, the kneading strength will be more likely to decline.

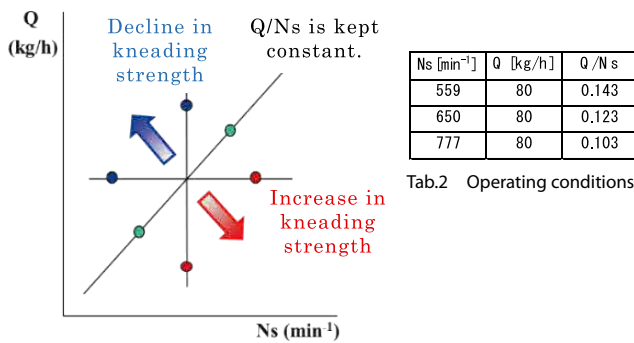


Fig. 6 Relationship between Q/N_s and kneading strength

6.2 | Verification Test

We conducted a verification test on the analyzer system and the AE sensing technology using Shibaura Machine's TEM-26SX. Table 2 shows the operating conditions under which the verification test was conducted. In the verification test, we measured a distribution of pressure in the resin flow direction inside the TEM when N_s changed with Q kept constant, and then monitored the state inside the TEM. The resin used for the test was ABS (TECHNO ABS 130 manufactured by Techno UMG Co., Ltd.). The TEM was equipped with 12 barrels ($L/D = 48.5$). Four pressure sensors were installed on Barrel No.9 and No.10, and the AE sensor on Barrel No.7. (See Fig. 7.)

Next, the screw configuration was as illustrated in Fig. 8. The AE sensor was installed on kneading section No.1, and the analyzers on kneading section No. 2.

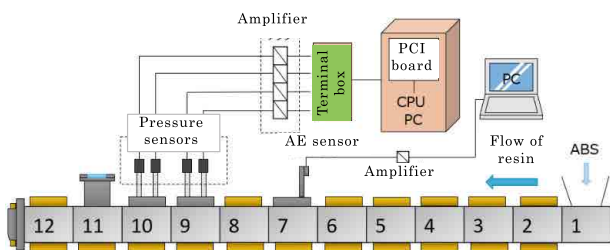


Fig. 7 Machine configuration in the verification test

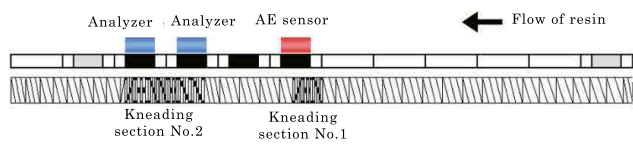


Fig. 8 Screw configuration in the verification test

6.3 | Findings from the Measurement of Distribution of Pressure

Fig. 9 shows the relationship between the distance from the tip of the screw and resin pressure. As N_s increased with Q kept constant at 80kg/h, resin pressure inside the TEM was more likely to decline. To be more specific, at the entrance to kneading section No. 2 (represented as ④ in Fig. 9), resin pressure was 1.90MPa with $N_s = 559\text{min}^{-1}$, but it declined to 0.70MPa (by approximately 63%) with $N_s = 777\text{min}^{-1}$. In addition, with $N_s = 559\text{min}^{-1}$, resin pressure was at its peak at the point presented as ③ in Fig. 9 while with $N_s = 777\text{min}^{-1}$, it was at the point presented as ②. These results indicate how the screw filled with resin will change at each position of KD in the kneading sections when N_s changes with the same screw configuration and constant Q . By making the most of such change, it becomes possible to adjust the operating conditions and assess if KD in the kneading section is producing an intended effect under the specified conditions.

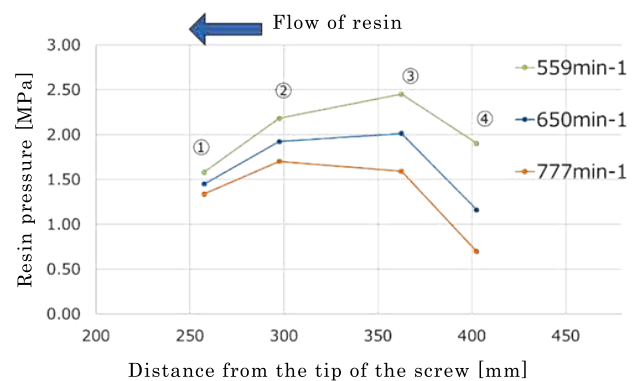


Fig. 9 Distribution of pressure inside TEM

6.4 | Finding from State Monitoring

Fig. 10 shows AE signals on a graph when the operating conditions are changed. This graph shows changes in plastic behavior over time with a moving average line as N_s changes from 559min^{-1} (constant as shown in the left of the graph) to 650min^{-1} in stages. The graph reveals that as N_s increases, the signal strength is more likely to increase, and the moving average line is likely to rise. On the other hand, once N_s has reached 650min^{-1} , the moving average line

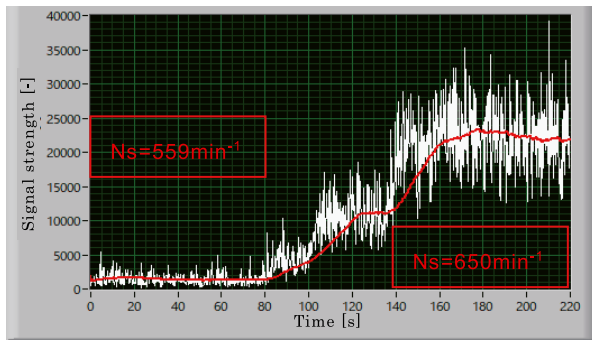


Fig. 10 Changes in AE signals when the operating conditions are changed

will gradually level-off.

Note this graph can be displayed in real time on the PC. For instance, when we set multiple operating conditions for an extrusion molding test and take samples under each operating condition while continuously changing the conditions one after another, the display function will allow us to confirm in real time that running the TEM has gone into a steady state, and to finally determine the accurate timing of sampling.

7 Conclusion

Utilizing the data collected from the analyzer system and the AE sensing technology makes it possible to predict the state inside the TEM, which has been difficult to do. So far, primary importance was placed on the physical properties of resin samples produced by extrusion for evaluation. However, from this time forward, an optimum configuration for extrusion molding can be considered much more efficiently than before by evaluating not only the quality of resin samples but also how the screw is filled with resin, plastic behavior inside the TEM, and appropriateness of the extrusion molding process.

With the successful development of this approach to objectively monitor the state inside the TEM, we have taken a big step toward the implementation of DX in TEM. As both a manufacturer and a user of the TEM, Shibaura Machine will continue to compare and verify a tremendous amount of data we have accumulated and is committed to developing TEM technologies which are friendly and contribute to both the users and society.

References

- 1) Takemasa Sugiyama, Development of an Analyzer for Twin Screw Extruders, Page 7, 8, and 18
- 2) Masatoshi Ohara, Research on Flow in Twin-Screw Extruders, Page 3 and 5
- 3) Masatoshi Ohara, Shin-ichiro Tanifuji, Yuya Sasai, Takemasa Sugiyama, ShoUmemoto, Jun-ichi Murata, Isao Tsujimura, Shin-ichi Kihara, Kentaro Taki, Resin distribution along axial and circumferential directions of self-wiping co-rotating parallel twin-screw extruder. *AIChE Journal*, 2020.66(11): p. e17018.
- 4) Masatoshi Ohara, Yuya Sasai, Sho Umemoto, Yuya Obata, Takemasa Sugiyama, Shin-ichiro Tanifuji, Shin-ichi Kihara, Kentaro Taki, Experimental and Numerical Simulation Study of Devolatilization in a Self-Wiping Corotating Parallel Twin-Screw Extruder. *Polymers*, 2020. 12(11): p. 2728.
- 5) Kentaro Taki, Takemasa Sugiyama, Masatoshi Ohara, Sho Umemoto, Shin-ichiro Tanifuji, Jun-ichi Murata, Isao Tsujimura, Shin-ichi Kihara, Online Monitoring of the Degree of Fill in a Rotating Full-Flight Screw of a Co-rotating Twin-Screw Extruder. *AIChE Journal*, 2019. 65(1): p. 326-333.
- 6) Masatoshi Ohara, Yuya Obata, Shin-ichiro Tanifuji, Kentaro Taki, Experimental and numerical study of glass fiber attrition in molten polypropylene in D26 mm twin screw extruder based on the Hele-Shaw flow model, in 35th Annual Meeting of Polymer Processing Society. 2019, Polymer Processing Society: Izumil, Turkey.
- 7) Yuya Obata, Masatoshi Ohara, Shin-ichiro Tanifuji, Kentaro Taki, Experimental evaluation of fiber attrition behavior in twin screw extruder and prediction based on Hele-Shaw simulation. in Asian Coating Workshop 2019. 2019. Soul National University.
- 8) Sho Umemoto, Yuya Obata, Masatoshi Ohara, Shin-ichiro Tanifuji, Kentaro Taki, Experimental evaluation of devolatilization behavior in twin screw extruder and prediction based on Hele-Shaw simulation. in 13TH KOREA-JAPAN SYMPOSIUM ON MATERIALS AND INTERFACES,. 2018. Busan, Korea.
- 9) Masatoshi Ohara, Takemasa Sugiyama, Sho Umemoto, Shin-ichiro Tanifuji, Kentaro Taki, EXPERIMENTAL VALIDATION OF FILL RATIO, RESIN PRESSURE, RESIN TEMPERATURE OBTAINED FROM THE 2.5D HELE-SHAW MODEL IN FLOW OF COROTATING TWIN SCREW EXTRUDER, in ANTEC 2018. 2018: Orlando.

- 10) Masatoshi Ohara, Sho Umemoto, Yuya Obata, Shin-ichiro Tanifuji, Kentaro Taki, EXPERIMENTAL VALIDATION OF NUMERICAL SIMULATIONS OF DEVOLATILIZATION IN A CO-ROTATING TWIN-SCREW EXTRUDER, in ANTEC 2019. 2019: Detroit.

COLUMN

Experience with VR Games

**Takumi TSUCHIYA**

Machine Tools Company
Machine Tools Engineering
Department

Today, for recreation, I often spend my time on holidays starting up a game wearing VR goggles and enjoying a chat with friends, or playing board games within a virtual space.

What I do is essentially to enter any of an infinite number of worlds existing in a virtual space to enjoy various games or have a chat with others while viewing the landscape. You can set any 3D avatar you like as your appearance in this game. This is why I can see a giant robot and a dragon and sometimes a cute girl talks to me in a strange voice within the game.

You need to use a game engine called Unity® (registered trademark of Unity IPR ApS) to upload a world and a 3D avatar in the game. To do so, you are required to use tools for developers, so the hurdle is very high to be able to enjoy the game. To my surprise, however, most of the users can use Unity® to upload the avatars they desire. I'm also using my

favorite 3D avatar which I uploaded.

A common topic of conversation in the game is about the avatars, and I enjoy having a chat with other players while I stand in front of a mirror looking at both my own avatar and the other person's avatar. It is almost a game etiquette to make complimentary remarks on each other's avatars. There are many users who are familiar with avatars and they help others quickly solve problems related to the avatar such as uploading and errors. For this reason, I feel there is a good environment for users to continue to play the game with the same motivation regardless of a high hurdle for some operations. At the beginning, I struggled to upload an avatar, but now I can add new functions to my avatar and even try to create a 3D avatar based upon myself.

I'm enjoying it very much as I can experience new technologies totally different from those in my job. I recommend anyone who is interested in it to try it once in their spare time such as on holidays. The genre of the game I play is called VRSNS (Virtual Reality Social Networking Service).

Development of Grease Lubricated High-Speed Spindle

In recent years, the growing shift to EVs in the automobile industry has led to a demand for higher accuracy in die machining and improved surface quality to reduce the weight of die products. Furthermore, there remains an ongoing need to reduce the lead times for die fabrication by 10-20%, and so shorter machining times and post-processing (polishing) times are also issues. With this as a backdrop, there have been calls for faster spindle and cutting feed speeds. At the same time, customers are increasingly asking for products which are environmentally-friendly, energy-efficient, and maintenance-free. To meet these requirements, we decided to use a grease lubrication system which is superior to other lubrication systems from an environmental standpoint because it does not consume air to supply lubricating oil and does not disperse oil into the surrounding atmosphere. Additionally, we developed a high-speed spindle with the highest Dmn value for the grease lubrication system.



Hirohiko MATSUZAKI
Machine Tools Company
Machine Tools Engineering
Department

1 Introduction

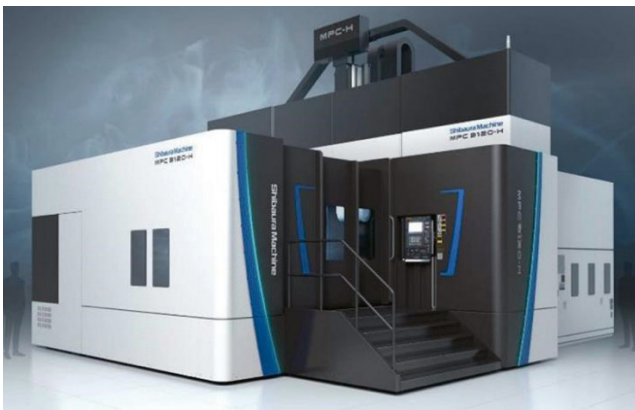


Fig. 1 MPC-H Appearance

In developing the MPC-H (Fig. 1) series of double-column machining centers for dies, the goals were to improve the surface quality of dies and to reduce the machining time. We planned to improve surface quality through a review of each part of the machine body and a review of the control-like adjustment process. Also, to reduce machining time, it is essential to equip the machine with a high-speed spindle. The following features were essential to begin the development of a high-speed spindle.

1. Support for attachment change system
2. Support for light finish cutting and maximum rotational speed of 20,000 min⁻¹
3. Environmentally-friendly and energy-efficient operation with maintenance-free performance
4. Capable of supporting spindle swivel operation

2 High-Speed Spindle Structure

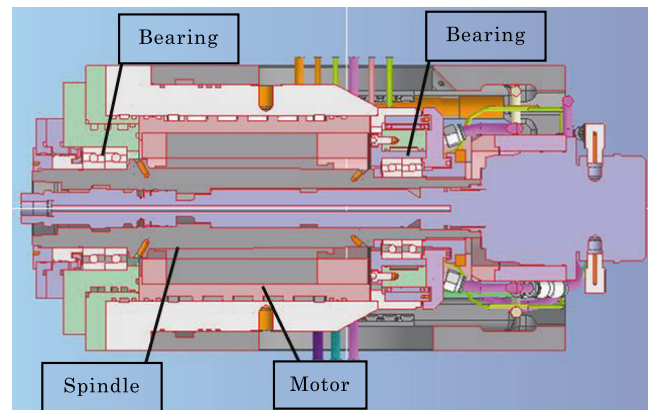


Fig. 2 Spindle Structure

The high-speed spindle to be developed also needs to be as small as possible to allow mounting on a swivel-type attachment. For this reason, a built-in drive system is used where the motor is shrink-fitted to a spindle having a built-in tool loading/removal section as shown in Fig. 2, and the motor directly drives the spindle.

The planning process focused on the following items.

1. Spindle taper method
2. Bearing location and lubrication system
3. Bearing preloading
4. Management of bearing temperature

The following sections will explain each of these items.

2.1 | Spindle Taper Method

Generally, the BT and HSK tapers are commonly used. For this development, the HSK taper was used because it enables shortening of the entire spindle unit and is suitable for high-speed rotation.

2.2 | Bearing Location and Lubrication System

To make the spindle unit compact, the bearing combination system uses the DT+DT system, where the front and rear of the motor are supported by bearings.

Next, the bearing lubrication method was selected from two options. These methods are described below.

2.2.1 | Oil-air Lubrication

This method supplies high-pressure air + fine oil particles from the side of the bearing to the inside of the bearing using an oil supply nozzle. This method is also used in Shibaura Machine's 30,000 min⁻¹ spindles for aluminum machining and has a proven track record of performance. Smooth draining of continuously supplied lubricating oil is the key to achieving stability during lubrication, but our use of this method has been limited to machines without attachment changes. Therefore, using this method in the new high-speed spindle raises the following concerns.

- (1) When the attachment is disconnected, air enters the oil line, and when oil is mixed with air, the oil mist cannot be continuously supplied correctly.

*In the initial adjustment of Shibaura Machine's proven oil-air lubrication system, it is stated "air discharge operation should be performed until the lubricating oil no longer contains air".

- (2) Oil drainage issues arise when the spindle posture changes because it is mounted on a swivel head. If oil drainage is not performed properly, the lubricating oil stays in the bearing, and excessive lubrication leads to bearing burnout.
- (3) Oil dispersion leads to contamination of the factory environment (air).

2.2.2 | Grease Lubrication

This is the most common method of lubrication, which involves filling the bearing space with an appropriate amount of grease. Oil oozing out from the grease adheres to the transfer surface and lubricates between the rolling elements and raceways. From an

environmental standpoint, the advantage is air is not consumed and oil is not released into the atmosphere as in the above-described oil-air lubrication. However, after consulting with several companies, the concern about grease lubrication is the lack of a proven track record in achieving 20,000 min⁻¹ (Dmn 1.8 million).

There were concerns with both methods, but the oil-air lubrication method raised concerns about lubrication as well as issues with environmental load, such as oil dispersal into the atmosphere, and so it was decided to use the grease lubrication method even though it presented the most difficult hurdle in terms of rotational speed.

2.3 | Bearing Preloading

The bearings are preloaded primarily to increase their rigidity. The preloading method can be either position preloading or constant-pressure preloading, but the constant-pressure preloading method was used because it did not increase the bearing preload at high-speed operation and can suppress bearing heat generation.

Spindle operation raises the motor temperature, which is transmitted to the spindle, causing the spindle to elongate. The constant-pressure preload system is a structure which prevents excessive force from being applied to the bearing due to this elongation. The following are the key points of this system.

- (1) Movement shall be smooth and follow the elongation of the spindle.
- (2) The contact type shall be used to maintain the rigidity of the spindle system.

To achieve these two key points, the preload, slide structure, and mating of slide sections, and combinations of these, were examined and tested in this development. For this study, two types of slide structures were tested, and the advantages and disadvantages of each were found and will be described here.

2.3.1 | Preload Structure 1

In Fig. 3, the spring for preload is located outside the slide mechanism. The preload is set by adjusting the spring length and other dimensional control. However, the preload may not be as expected due to individual differences in springs.

The advantage of this method is, even after adjustment, the preload can be changed by simply removing two parts, making readjustment easy and facilitating testing of various preloads. The disadvantage is the spring is far from the slide section, making it

difficult for the slide section to move. To ensure proper sliding of the moving section, dimensional control of necessary parts during assembly is required.

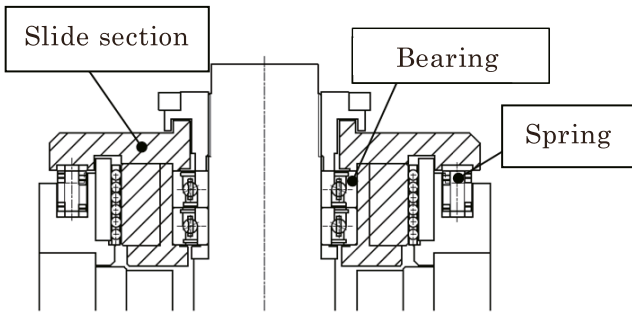


Fig. 3 Constant-pressure Preload Structure 1

2.3.2 | Preload Structure 2

Fig. 4 shows the spring directly below the moving section. This enables smooth movement of the moving section. In this development, the layout ratio of the components was studied and determined based on Shibaura Machine's past machine results and data. However, this method has a disadvantage of being difficult to readjust the preload if it does not reach the targeted value.

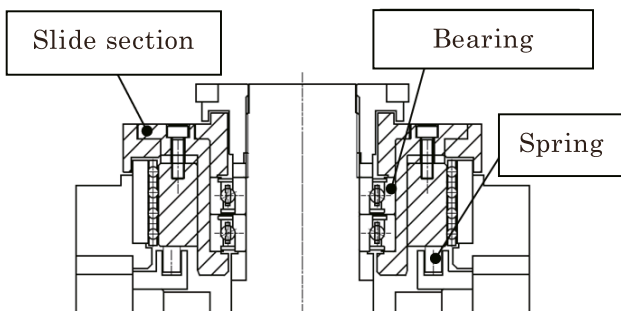


Fig. 4 Constant-pressure Preload Structure 2

In this development, each method was tested. When verifying the preload, the method in Fig. 3 was used to ascertain various conditions, and the method in Fig. 4 was used as the final structure.

2.4 | Management of Bearing Temperature

For bearing cooling, outer cylinder cooling was used to cool the bearing outer ring side. On the inner ring side, since there is a temperature rise associated with the spindle temperature rise, air is actively circulated inside the spindle to prevent heat buildup and to mitigate rotor temperature rise. To minimize the temperature difference between the bearing inner and outer rings, the optimal cooling water path was studied. In addition to these points, the

preload applied to the bearings was adjusted so stable rotation can be maintained even over long runs.

Also, bearing temperatures are sensed and constantly monitored for their conditions.

3 Test Results

Machining tests were conducted on the jug-shaped workpiece shown in Fig. 5. Comparisons were made using Snout 220 (maximum spindle rotational speed of 8,000 min⁻¹, capable of heavy-duty cutting) and High-Speed Snout (maximum spindle rotational speed of 20,000 min⁻¹, capable of light finish cutting). The machining conditions during testing are shown in Table 1.

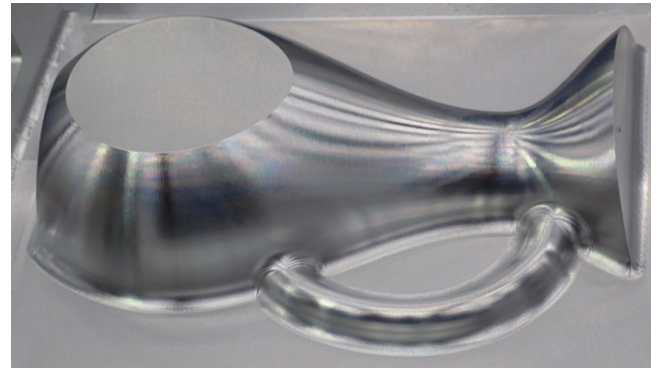


Fig. 5 Shaped Workpiece

Table 1 Cutting Conditions

	Spindle rotational speed (min ⁻¹)	Feed rate (mm/min)	Cutting Time(min)
Snout 220	3,920	1,090	153
High-speed Snout	15,000	4,170	66

Visual inspection of the machined surfaces showed both surfaces were equivalent. It was confirmed each of the adjustment sections described in this paper functioned and the high-speed spindle developed for finishing had sufficient performance.

4 Conclusion

A high-speed spindle with the highest Dmn value as a grease lubrication system was developed. The results of the machining test showed the machining time was reduced by 57% (compared to our test workpiece) while maintaining satisfactory machining quality, as was originally intended. We will continue to test-process various workpieces and gather further knowledge.

By using a lubrication system which does not require air, air consumption is reduced by 500 NL/min compared with mist-lubricated or oil-air lubricated spindles of other companies, and an annual reduction of 3,600 kg of CO₂ emissions is expected (based on average machine operating hours). Also, because there is no oil dispersal, this method will contribute to reduced environmental impact.

In addition, this eliminates the need to periodically supply oil for oil-air to the pump, giving the pump a maintenance-free design.

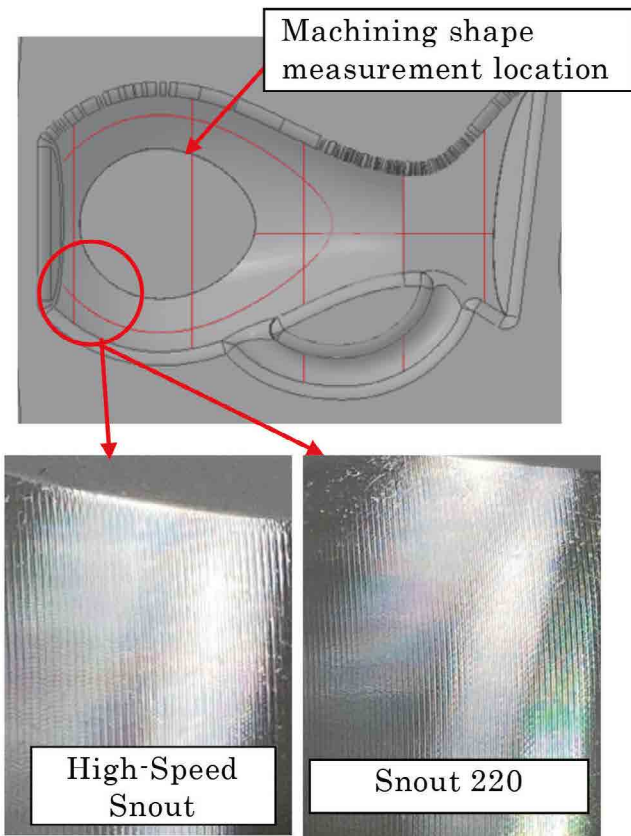


Fig. 6 Photos of Machined Surfaces

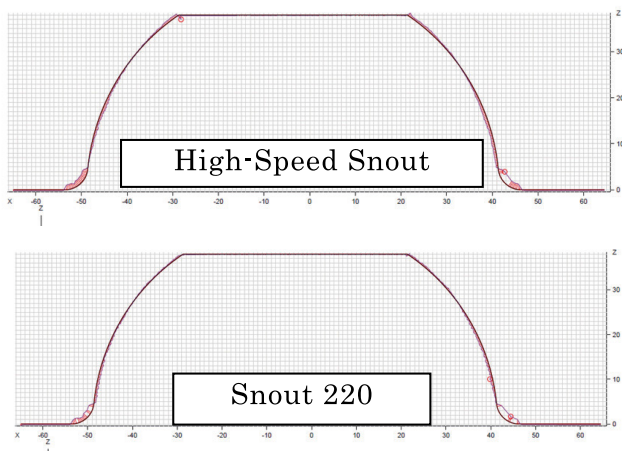


Fig. 7 Machined Shape Measurement Results

The accuracy of the machined shape was within a few micrometers of the model shape (Fig. 7).

Cutting time was reduced by 57%, a result expected to contribute to higher efficiency in the future (Table 1).

Using Direct Cutting to Reduce Energy Usage in Cemented Carbide

To address the issue of greenhouse gas emissions, various sectors are being called upon to implement energy conservation measures. In the manufacturing industry, energy conservation is achieved by reducing the power used in product manufacturing. Cemented carbide has excellent characteristics as a press die material for forging, but its high mechanical strength makes cutting difficult, and so die shapes have conventionally been fabricated by using electrical discharge machining (EDM). However, because EDM removes a small amount of material and requires electrode fabrication of inverse shapes, this results in an extremely long overall fabrication time and high power usage. Recent advancements in tool development have made cutting of cemented carbide possible by direct cutting. This report presents a case study comparing the times for fabricating gear-shaped cemented carbide dies by cutting processes and by EDM.

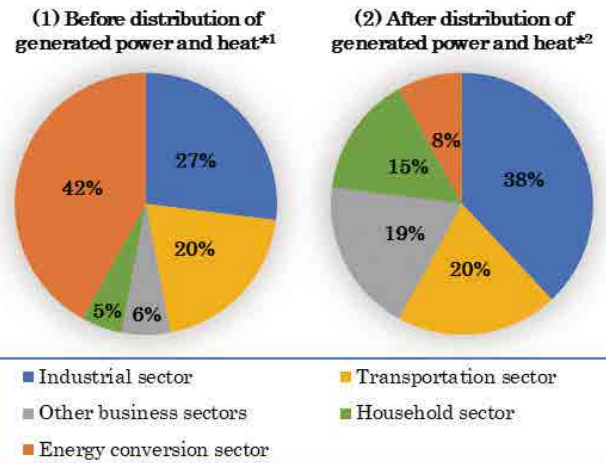


Tomoyasu MAKIDA
Machine Tools Company
Machine Tools Engineering
Department

1 Introduction

Greenhouse gas emissions have become a global issue in recent years, and the Japanese government declared in 2020 Japan will aim to become carbon neutral by 2050, reducing its overall greenhouse gas emissions to zero. In line with this target, the industrial sector is being called upon to implement energy conservation measures.

Fig. 1 shows a breakdown by sector of CO₂ emissions generated and emitted by fuel combustion in Japan in FY 2019 according to government figures. From this, the energy conversion sector, such as power plants, accounts for up to 42% of Japan's CO₂ emissions. This includes CO₂ emitted during the generation of electricity and heat by power plants and other sources to supply other sectors. If CO₂ emissions from power generation and other sources are recalculated as if they were emitted on the consumption side instead of the production side, the industrial sector would account for the largest CO₂ emissions at 38%. This means the industrial sector consumes considerable electricity and heat, equivalent to an increase of 11%, in addition to the CO₂ generated in production processes. CO₂ emissions total 1.029 billion tons, with the electricity and heat consumed in the industrial sector alone emitting more than 100 million tons annually.¹⁾ Also, due to the impact of various global situations, Japan is facing a power shortage crisis, and the manufacturing industry, which falls under the industrial sector, is also required to reduce energy consumption, especially electricity



*1 Calculating CO₂ emissions from generation of power and heat as if they were emitted at the production side.
*2 Calculating CO₂ emissions from generation of power and heat as if they were allocated to the consumption side.

Fig. 1 CO₂ Emissions by Sector in Japan

usage. In the manufacturing industry, electricity is used mainly for the air conditioning and machinery used in the production of products, and the less electricity used by each facility to produce a single product, the more energy efficient the entire factory can be.

Cemented carbide is a material which has excellent properties such as high wear resistance and heat resistance, and manufacturers have high expectations for its use as material for press dies for forging gears and other components. However, cemented carbide is classified as a hard and brittle material, and its high mechanical strength makes it difficult to cut. Consequently, until now, die shapes have been fabricated mainly by electrical discharge

machining (EDM), which is a process which can machine any material which conducts electricity, regardless of its hardness. EDM requires an extremely long fabrication time throughout the entire process because the amount of material removal per discharge is small and the electrode must be fabricated with the inverse shape required for machining. Therefore, improving the production efficiency of cemented carbide dies has become a challenge. In response, recent advances in tool development have made it possible to cut cemented carbide by direct cutting.

Cutting does not require fabrication of electrodes with the inverse shape, thus reducing the time required to fabricate the product. Shorter product production times throughout the entire process will improve production efficiency, leading to energy savings throughout the factory. In this report, we present a case study comparing the fabrication times of EDM and cutting processes for gear-shaped cemented carbide dies.

2

Manufacturing Methods for Cemented Carbide Dies

2.1

Conventional Manufacturing Process for Cemented Carbide Dies

The conventional manufacturing process for cemented carbide dies is shown in Fig. 2. First, a powder, which is blended and mixed with raw materials such as tungsten carbide and cobalt adjusted to have the mechanical strength required by the cemented carbide die to be manufactured, is pressed and molded, then pre-sintered at a low temperature and hardened until a certain degree of hardness is achieved. Next, primary shape machining is performed to roughly shape the product, and the holes required for the product are machined. Once the cemented carbide has been sintered to the required mechanical strength, a reference surface is created by grinding. At this stage, an electrode of the inverse shape is fabricated for EDM, the cemented carbide die undergoes secondary shape machining by EDM, and the machined surface is finished by grinding.^{2,3)} At this point, grinding must be used to remove altered layers such as molten recast layers and microcracks which occur on the surface layer due to EDM.

This report presents a comparison where cutting replaces the secondary shape machining where EDM is performed. Accordingly, this eliminates the cutting process to fabricate electrodes with inverse shapes in the preceding process. Therefore, when secondary shape machining is performed by cutting, the entire amount of

electricity due to machine operating time which was spent on electrode fabrication can be eliminated.

2.2 | Electrical Discharge Machining (EDM)

Because EDM can process any material which conducts electricity, regardless of its hardness, it has been used to fabricate shapes of materials with high hardness, such as cemented carbide and high-speed tool steel. It is also used for machining deep and narrow grooves and other shapes which are difficult to cut. However, because EDM processes metal by discharging electricity and melting it, the amount of material which can be removed in a single discharge is small and the machining time is long. The characteristics of this machining method also cause the formation of an altered layer on the machined surface, resulting in reduced surface roughness, cracking, and other problems. These could shorten the life of the die, and so the altered layer must be removed in the finishing process.

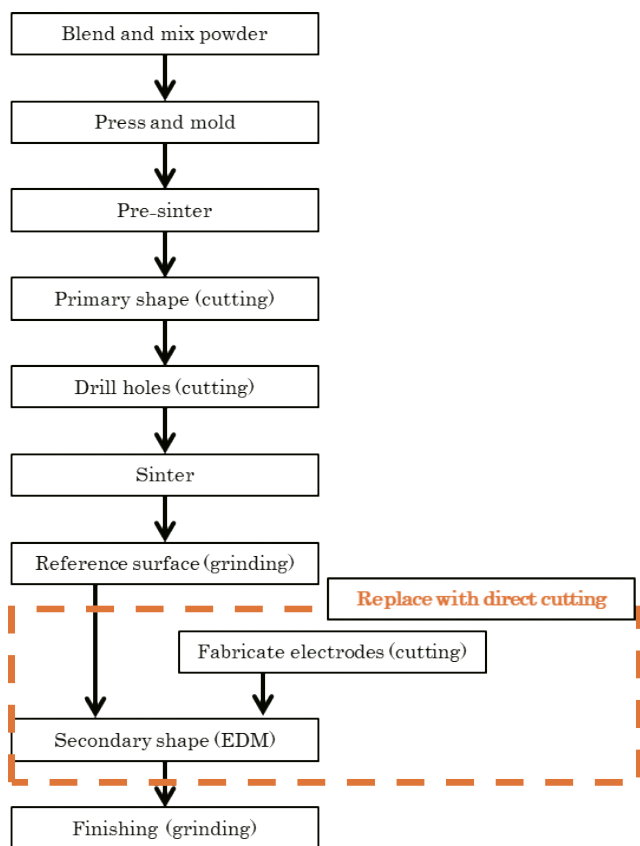


Fig. 2 Production Process For Cemented Carbide Dies

The altered layer has a depth of several tens of micrometers and must be removed in the finishing process, which also increases the finishing time in the next process. Also, if multiple electrodes are used in machining, the required number of electrodes must be fabricated, which requires additional electrode fabrication time based on the number of electrodes as well as the additional machines and tools needed for machining.

2.3 | Direct Cutting of Cemented Carbide

As mentioned above, cemented carbide has excellent characteristics as a material for dies, but it is well known to be extremely difficult to cut. Recently, however, the development of diamond-coated tools and polycrystalline diamond tools has made it possible to easily cut cemented carbide through direct cutting. This eliminates the need to fabricate electrodes in the inverse shape required for EDM, and because the metal is machined by shaving, no altered layer occurs on the machined surface, and the finishing allowance for finishing can be reduced to several micrometers. This enables reduction of not only the machining time for secondary shape machining, but also the machining time for finishing in the next process.

3 | Comparison of Machining Times for Electrical Discharge and Cutting

Fig. 3 shows the machining model of a gear die used for verification and the actual machined product. We asked Fuji Dies Co., Ltd. to estimate the machining time for fabricating this type of gear die by EDM and by cutting, and compared the results for a shape with a finishing allowance of 0.2 mm left. Table 1 shows the gear specifications.

The machining time by EDM was 960 minutes, and the time needed to fabricate the four electrodes with inverse shapes used for EDM was 1050 minutes. In contrast, the cutting process had a machining time of 780 minutes.

As reference values for power usage, we used the wire EDM machine from Company S and our company's UVM-450D (H) machining center. Company S's wire EDM machine has a total electrical capacity of 13 kVA. In contrast, the actual electrical capacity of our UVM-450D(H) during machining is about 10 kVA, which is almost the same as that of a wire EDM machine when the power usage of the ancillary equipment is also taken into account.

In the EDM process, the total time for electrode fabrication and

EDM is 2010 minutes, which is more than twice the machining time required for cutting. Based on the above data, assuming the power usage of wire EDM machines and machining centers is equivalent, because power usage is proportional to the overall machining time, cutting requires 38.8% of the machining time of EDM machines, and so power usage would be reduced by 61.2% if EDM was replaced by cutting. Therefore, we conclude replacing the EDM process with cutting as the manufacturing method for cemented carbide dies will contribute to both improved overall factory production efficiency and reduced power usage in the manufacturing industry.

4 | Integration and Higher Accuracy for the Manufacturing Process of Cemented Carbide Dies

4.1 | Finishing of Cemented Carbide Dies

The results from the previous section show, when looking at cemented carbide die fabrication methods in terms of energy usage, die fabrication by cutting is better than by EDM. However, the results in the previous section are for secondary shape machining, and typically, reference surface machining is performed before this process, followed by finishing. When EDM is used, the workpiece must be taken out between each process and set up again for machining on the next machine. Therefore, in our proposal, we use the UVM High-precision Machining Center to perform reference surface machining, secondary shape machining, and finishing on the same machine without performing setup again.

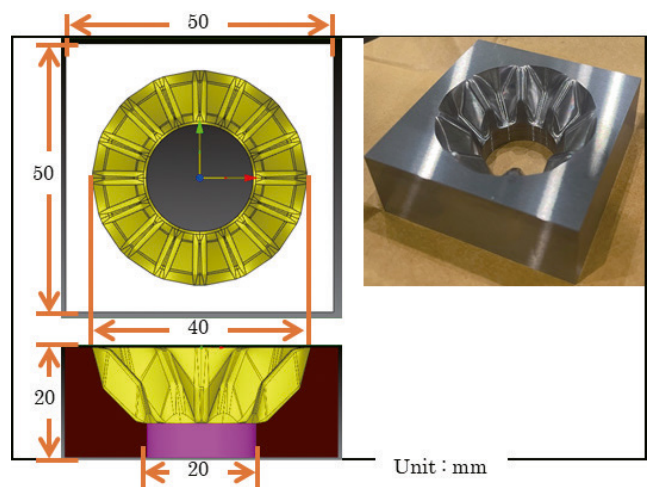


Fig. 3 Machining Model of Gear Die and Actual Machined Product

Table 1 Gear Specifications

Gear type	Bevel gear
Large end diameter	40 mm
Small end diameter	20 mm
Pitch circle diameter	30 mm
Number of teeth	8
Module	3.75 mm
Tooth tip conical angle	45 degrees
Tooth base conical angle	45 degrees
Pitch conical angle	45 degrees
Tip distance	13.8 mm

4.2 | UVM High-precision Machining Center

In recent years, as industrial products have been developed with increasingly higher accuracy, there has also been demand for higher 3D shape accuracy for gears. High-accuracy machine tools are required to achieve this. Shibaura Machine has developed the UVM series of high-precision machining centers which employ high-accuracy linear guides and linear motors for the three linear drive axes to achieve a high positioning accuracy of 10 nm and high rotational performance by using aerostatic bearings on the rotating spindle. The UVM series can be equipped with "FormEye®", Shibaura Machine's proprietary feature for high-accuracy measurement of tool geometry, and "VectPath", a feature which performs automatic 3D correction of the machining path to the tool contour geometry.^{4,5)}

Fig. 4 shows the process of automatic 3D shape correction using these methods. For 3D shapes such as gears, conventional machining centers could only perform 2D corrections based on two points: tool length and tool diameter. Therefore, the unevenness of the tool contour would be transferred to the product shape and would become a shape error. Tool contouring accuracy has been improved to about 1 micrometer through the efforts of tool manufacturers, but tool wear, runout, and external disturbances can cause shape errors of several micrometers. To solve this issue, we studied how to correct the tool 3D geometry. In the conventional process, a machining path created by CAD/CAM is actually machined, and based on the measurement results, the CAD is corrected in areas of poor geometry, and the machining path is created again. The VectPath tool path vector correction feature adds the tool contact angle information to the first generated machining path, and the tool contour measured by FormEye® on the machine is read, and so corrections are constantly being made at the machine side, and even changes to the tool contour due to wear are automatically re-corrected by re-measuring the tool. In

other words, the correction process is shortened because the CAD/CAM does not need to be modified each time a correction is made. This correction process also reduces the overall work time and thus improves factory productivity. With such a wide variety of features, we believe by allowing the UVM to handle the cutting of cemented carbide dies, it could cover all processes from reference surface machining to finishing, and even achieve high shape accuracy.

5 Conclusion

In the manufacture of cemented carbide dies, we showed replacing conventional EDM with cutting can reduce the machining time by 61.2%, contributing to improved production efficiency and energy conservation in the factory. Also, by using the UVM High-precision Machining Center for cutting, the four processes from reference surface machining to finishing can be integrated into a single process with the same setup. In addition, we proposed a way to further reduce work time with an automatic 3D shape correction process which does not revert to CAD/CAM, allowing for high shape accuracy without recalculation of machining paths.

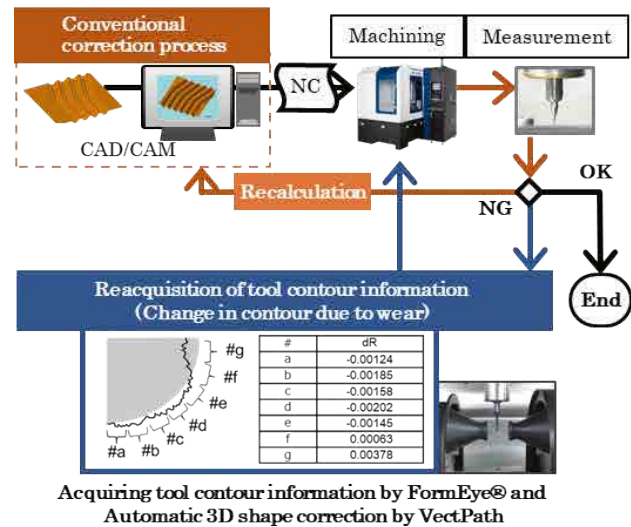


Fig. 4 UVM Automatic 3D Shape Correction Feature

Although this paper focuses on cemented carbide dies formed into gears as an example, other industrial products also need higher and higher accuracy, and require high-accuracy machining. We must also address environmental issues in this process. Therefore, we will continue to strive to develop clean and advanced high-machining machining.

References

- 1) Ministry of Economy, Trade and Industry website, Current Status of Greenhouse Gas Emissions, <https://www.env.go.jp/council/06earth/y0620-3b/mat03.pdf> (Japanese), (Reference: 2022-7-19).
- 2) Kei Amano, Atsuro Inoue, Toshiaki Takahashi, High accuracy Cutting of Hardened Steel, *Toshiba Review*, Vol. 53, No.7, (1998), pp. 47-50.
- 3) Keiichiro Yamamoto, Hiroaki Wakamiya, Yukihiro Hayakawa, et al., A Study of Integrated Technology Development for the Manufacture of Large Cemented Carbide Molds, *Journal of the Society of Quality Engineering*, Vol. 27, No. 5, (2019), pp. 35-43.
- 4) Shibaura Machine Corporation website, UVM series, <https://www.shibaura-machine.co.jp/en/product/nano/lineup/uvm/> (Reference: 2021-4-12).
- 5) Tomoyasu Makida and Kunitaka Kuriyama, Development of a three-dimensional compensation processing for machining center, *Proceedings of the 2022 Japan Society for Precision Engineering Spring Conference*, (2022), pp. 489-490.

Efforts to Save Energy in Control Equipment Development

In recent years, the growing global interest in the SDGs has become a major trend, and countries around the world are accelerating their efforts for effective use of resources and carbon-free products. Our various control components require electric power for control operations or actuator drives, and we have been developing energy-efficient products with low power loss and reducing the number of components. This paper introduces our efforts in this area.



Shinjiro ONO

Control Systems Company
Control Systems Engineering
Department



Yoshimi MIZUGUCHI

Control Systems Company
Control Systems Engineering
Department



Shoichi SATO

Control Systems Company
Control Systems Engineering
Department



Yuichi EGAWA

Control Systems Company
Control Systems Engineering
Department

1 Introduction

One role of the Control Systems Engineering Department is to improve customer product competitiveness by providing various control components (hardware, software, and system integration) optimized for in-house companies and external users.

In addition to the control technologies we have developed over the years, to maintain sustainable manufacturing activities, an urgent need and key issue is to address greenhouse gas (CO₂) emission controls, which affect climate change.

In this paper, we introduce our efforts to save power, labor hours, and resources in various control components.

The application of new-generation electronic devices (microcontrollers, power modules, etc.) to controllers and servo amplifiers not only reduces the power loss of the product itself, but also contributes to reduced environmental impact throughout the entire product lifecycle by consolidating various functional components into high-function IC (integrated circuit) packages and reducing the number of components, thereby reducing the manufacturing labor hours and product weight.

As an approach to using software functions to assist in energy

savings, we will introduce a function which shortens the machine operation time itself and present an example of promoting energy savings by clearly indicating the power usage to the user during machine operation.

2 Change of the Microcontroller

For the microcontrollers used in our controllers, the H8S/2144, which was manufactured using a 0.5- μ m process, was released by Hitachi in 1997, and was used in many products as the microcontroller for the TC200 and TCmini TC3 series of sequence controllers.

However, in 2015, when the H8S/2144 was nearing obsolescence due to process advancements, Renesas released the RX231, which was manufactured using a 40 nm process, and we studied it for use in the TCmini series.

It outperforms the H8S/2144 in terms of processing speed, memory capacity, and communication capabilities, etc., and has been used for the TC12 series from 2016.

Since 2016, its use has been expanded to the TC12-10, TC12-11, TC12-12, TC12-13, TC12-01, TC12-02, TC12-0A, TC12-1D, and

TC12-14 products.

The number of H8S/2144 units shipped in FY 2019 was 12,576. From FY2021, 4,954 of all shipments was changed over from the H8S/2144 to the RX231.

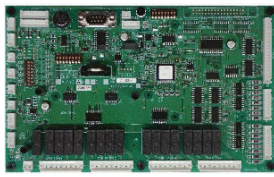


Fig. 1 TC12-01

Example of reduced power usage in specifications

Old model TC3-01: 3.35 W

New model TC12-01: 1.89 W → Reduction of 1.46 W (44%)

Reduction in annual electricity usage of approximately 63 MWh

* Equivalent to year-round operation of 4 to 5 air conditioners for 30 m² rooms

At a metering rate of 20 yen/kWh, this comes to 1.26 million yen.

* The change from TC3 to TC12 is primarily a change in microcontroller and elimination of unused functional components, with no change in basic functions.

3 Change of the Gate Array (Semi-custom IC)

In 2005, we developed a gate array (T-P0243303) for the servo amplifier BS-X series using the former NEC CMOS-12M process.

The development of compatible ASICs for the BS-X series was studied when the old NEC ASICs began to be discontinued in 2016. The development (TM20242R0) was performed by the Taiwanese manufacturer CMSC starting in 2018.

The power usage was reduced by changing the process from 0.15 μm to 0.13 μm and by adopting a clock gating circuit. As shown in Fig. 2, the power efficiency increased and the effect in suppressing the temperature rise was verified.

Result: Simulated power usage

*At maximum operating frequency

T-P0243303: 685 mW

TM20242R0: 240 mW

→ Reduction of 445 mW (65%)

Shipping results:

T-P0243303: FY2018 67,941 units

TM20242R0: FY2022 7,830 units

(Replaced April-June)

Reduction in annual power usage of approximately 125 MWh

* Equivalent to year-round operation of 8 to 9 air conditioners for 30 m² rooms

At a metering rate of 20 yen/kWh, this comes to 2.50 million yen.

* Clock gating: The circuit is configured so the clock for the flip-flop is supplied only when the data changes.

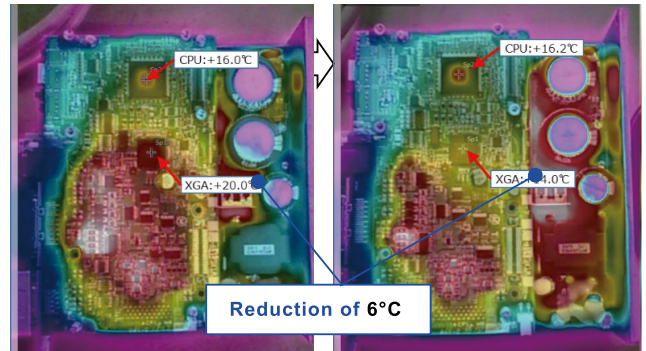


Fig. 2 Temperature rises (Left: Current product, Right: Compatible product)

4 Reduction in Number of Parts Used in TCmini

The current thermocouple circuit in the TCmini series has been used since 2009. Initially, the emphasis was on high accuracy, but a faster sampling cycle (400 ms for 1 channel) became necessary to meet customers' demand for improved controllability.

For this reason, Maxim's MAX31855 cold-junction compensated thermocouple-to-digital converter was used.

The MAX31855 has an internal cold junction circuit which converts thermocouple input to temperature data and outputs it as serial data. The minimum conversion time is 70 ms, which allows for faster sampling cycles.

Also, complex analog switching and V-F conversion circuits are no longer required, enabling a reduced number of components.

Number of parts: Per channel

Current circuit: 55 (ICx4, Rx35, Cx10, PCx4, OSCx1, TRx1)

New circuit: 23 (ICx3, Rx12, Cx7, PCx1)

→ Reduction of 32 components and 55% reduction in mounting area

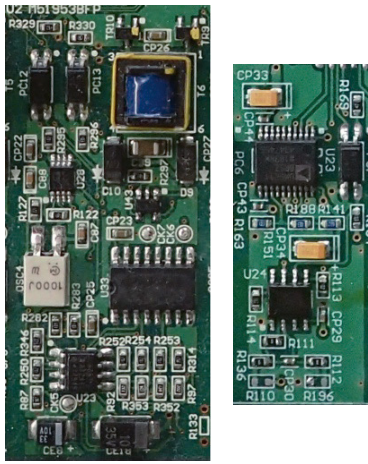


Fig. 3 Comparison of thermocouple input circuits (Left: Previous model, Right: Latest model)

Rated voltage: 600 V
Rated current: 150 A

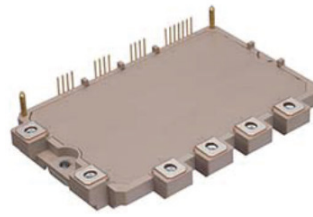


Fig. 4 Power module

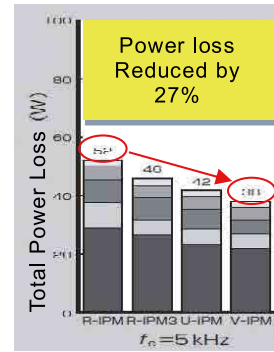


Fig. 5 Example of reduction in power loss

The following is an example of a servo amplifier (GM series) with the latest power module and a machine equipped with the same servo amplifier.

5 Change of the Power Module

Power modules installed in variable speed drives (commonly known as servo amplifiers) for feed axis servo motors of various machines have a power conversion (DC to AC) switch function. Power conversion switches for servo amplifiers are mainly composed of semiconductor power devices called IGBTs (Insulated Gate Bipolar Transistors). IGBTs are distributed as power module products which combine high-speed switching performance with high power handling capability, and their energy-saving performance is improving every day.

In conjunction with the model change of the servo amplifier, a new-generation power module has been used to help reduce the power usage of the machine.

In the example in Fig. 5, the latest models (servo amplifier GM series and IPM V series) achieve a loss reduction of 27% (14 W) compared to the early models (servo amplifier AR series and IPM R series).

This results in an estimated annual reduction of 123 kWh (=14 W x 24 hr x 365 days) in power usage under continuous operation of the servo amplifier (GM42A) + servo motor (rated 6 kW).

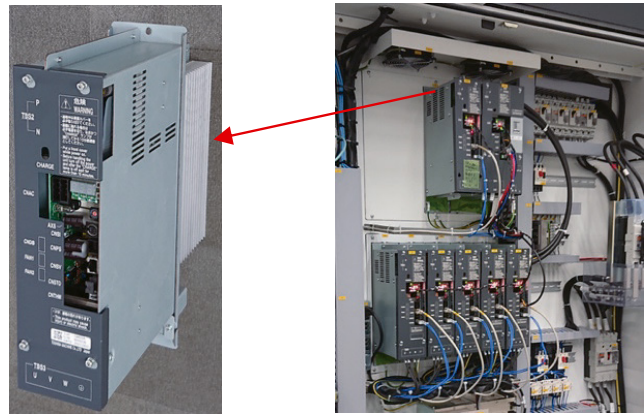


Fig. 6 Servo amplifier GM series



Fig. 7 BTD-110S.R16 horizontal boring machine

6 Shorter Machining Times for Reduced Power Usage

The TOSNUC PX200, our numerical controller for machine tools, is equipped with CNC SHAPE as a die machining function. Turning on the CNC SHAPE assist function improves machining speed, reducing machining time and machine power usage.



Fig. 8 TOSNUC PX200

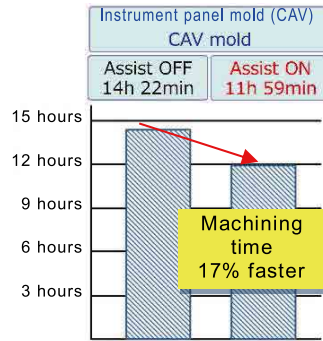


Fig. 9 Example of improvements in mold processing time

Shibaura Machine is also working on a "workpiece weight adaptive control" function to improve inefficiencies when machining lightweight workpieces on machines with large maximum loading capacity. Parameters are optimized according to the workpiece weight, contributing to shorter machining times and reduced machine power usage. Fig. 10 shows an example of a test performed on the MPJ-3120M.

Machine: Max. loading capacity 15t	Machining time 15.8 hr → 12 hr
Workpiece: 5t	24% faster

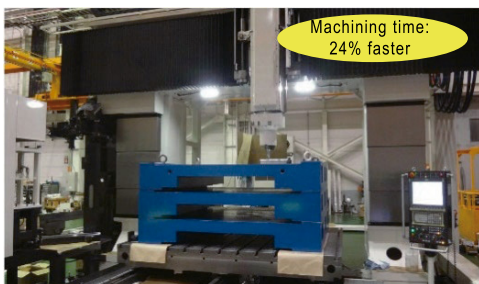


Fig. 10 Demonstration test on MPJ-3120M

7 Display of Power Usage

Shibaura Machine's process controllers for injection molding machines display the power usage information on a screen so operators can easily monitor the power usage.

Real-time monitoring of changes in power usage based on the molding operation conditions facilitates the process of setting energy-saving operation patterns.



Fig. 11 Power usage screen

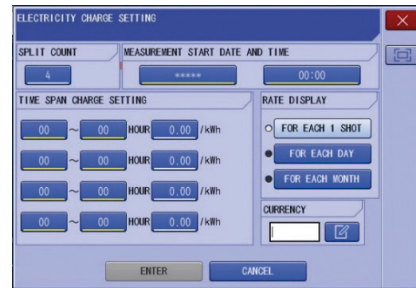


Fig. 12 Electricity rate setting screen

8 Conclusion

This paper has described initiatives for saving power, labor time, and resources for various control components.

We believe the timely adoption of electronic devices with advanced energy-saving technologies will continue to contribute to a reduced environmental burden.

**Shinju SAKURAI**

Control Systems Company
System Engineering
Department

My job is to deliver new automation equipment to customer plants. I will relate one example of the bitter experience of failure I had in the past.

This story is about a robotic unit to unload strip-shaped wood materials carried into a customer plant from a flat transport structure called a pallet, and then input them into the existing machining device.

It was my first experience to handle wood materials, so I conducted a transportation test after arranging in advance the dimensions of the material to be machined and the dispersion requirements and conditions within the process, which I thought were appropriate. I developed the handling equipment based on those conditions. However, the actual workpiece delivered to the plant included goods with dispersion significantly outside the conditions I determined

(such as bowing, cracks, deformations, and exposed spurs).

The equipment was delivered to the customer because the problems which occurred were determined to lay within the customer's responsibility. However, when I later revisited the customer, I found our equipment was not being used because of frequent issues such as interruption of operation.

There were several causes for this failure, such as the customer's insufficient understanding about the workpiece delivered to its plant and my lack of knowledge about wood materials; I provided design instructions with the same tolerance and accuracy as those for general industrial products.

Through this experience I acutely realized the importance of carefully listening to customers especially in the case of an inquiry received from a new industry. Since then, I have been making sure to see and check actual worksite conditions and actual workpiece characteristics without taking action based on mere assumptions. This is the story of my experience of failure in the past, which is inscribed in my memory.

Approach to Reduction of Environmental Impact in SCARA Robot Development

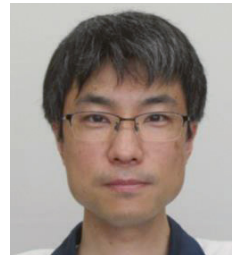
Performance requirements for industrial robots are increasing year by year, with expectations for shorter cycle times and improved trajectory accuracy in terms of operating performance, as well as compatibility between these and cost. Furthermore, such robots are required to be environmentally friendly products from the viewpoint of reducing environmental impact. We have developed the SCARA Robot THE800/THE1000 as the new product to meet this need. This paper introduces the measures taken to reduce environmental impact in the development of THE800/THE1000 and the design efforts using 1DCAE, and reports on the effectiveness of the measures in reducing environmental impact.



Katsuyoshi KIDO
Control Systems Company
Robot Engineering Department



Yoshinori NAKAI
Control Systems Company
Robot Engineering Department



Ryuichi AMEMIYA
Control Systems Company
Robot Engineering Department



Yusuke NAGAREDA
Control Systems Company
Robot Engineering Department

1 Introduction

SCARA robots are also called horizontal articulated robots. With the 4-DOF mechanism consisting of 3-axes of horizontal rotation and 1-axis of vertical linear motion, this industrial robot excels at working on flat surfaces. They have a wide range of arm lengths, from 300 mm to over 1,000 mm, and are used to automate various processes. Among them, high payload robots with arm lengths of 800 mm or 1,000 mm are in high demand in the market for transporting secondary batteries used in electric vehicles (EVs). Our conventional SCARA robots, TH850A and TH1050A, are our existing high payload robots with arm lengths of 800 mm and 1000 mm, respectively, and have the necessary minimum required performance. However, the manufacturing process of rechargeable batteries is becoming more efficient day by day, and to further increase tact time, robots are required to have higher speed and improved trajectory accuracy. In addition, recent years have seen growing interest in reducing environmental impact, and from a carbon-neutral perspective, CO₂ emissions must be reduced. To meet these market requirements, we have developed the new SCARA robot THE800/THE1000.

The specifications of the new THE800 and the conventional TH850A are shown in Table 1. THE800 and TH850A are used for comparison below.

Table 1 Specifications of THE800 and TH850A

Model		THE800	TH850A
Number of controlled axes		4	4
Arm length(mm) (Arm 1 + Arm 2)		800 (350+450)	850 (350+500)
Operating range	Axis 1 (deg)	±132	±160
	Axis 2 (deg)	±152	±145
	Axis 3 (mm)	0↔420	0↔200
	Axis 4 (deg)	±360	±360
Max speed*1	Axis 1 (deg/s)	300	300
	Axis 2 (deg/s)	540	420
	Axis 3 (mm/s)	2,200	2,050
	Axis 4 (deg/s)	1,100	1,200
	Composite speed of axes 1 and 2(mm/s)	8,400	8,130
Rated payload mass(kg)		5	5
Max payload mass(kg)		20	20
Permissible load inertia (kgm ²)		0.6	0.2
Positioning repeatability *2	X,Y(mm)	±0.025	±0.010
	Z(mm)	±0.010	±0.010
	C(deg)	±0.010	±0.004
Mass of robot body (kg)		46	76
Applicable controller *3		TS5000-MS	TS3100

*1: Speed and acceleration are limited in accordance with the operation pattern, payload mass, and the offset value.

*2: The positioning repeatability of one-directional movement at a constant ambient temperature and machine temperature. It is not absolute positioning accuracy or trajectory accuracy.

*3: Model for standard specification; options such as CE specifications have different model.

2 Development of THE800/1000

2.1 Basic Specifications

Compared to the TH850A, the standard stroke of the third axis of the THE800 has been increased from 200 mm to 420 mm to meet recent customer needs. In addition, the allowable moment of inertia has been increased from 0.2 kg-m² to 0.6 kg-m² to grip larger workpieces. Fig. 1 shows the comparison of the appearance of THE800 and TH850A.



Fig. 1 Comparison of THE800 and TH850A appearance

2.2 Approach to Reduction of Environmental Impact

THE800/THE1000 were approached from various angles during the development phase to reduce environmental impact. The following is the description of the design details for reducing environmental impact.

2.2.1 Base Commonality

Base of THE800/THE1000 and other components are the same as those of the conventional THE600. Fig. 2 shows the names of the various parts of the SCARA robot (THE800), and Fig. 3 shows THE800 and THE600.

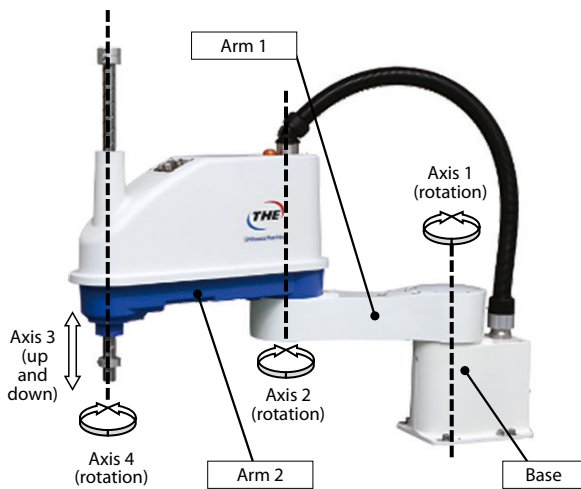


Fig. 2 The various parts of the SCARA robot (THE800)

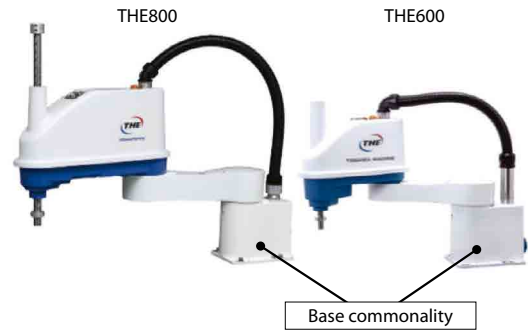


Fig. 3 Base of THE800 and THE600

2.2.2 Lightening of Arm 1 and Arm 2

For THE800/TH1000, a thorough structural analysis of Arm 1 and Arm 2 and the use of a highly flexible die-casting process allowed us to achieve the ideal shape. Table 2 shows Arm 1 and Arm 2 overall mass of THE800 and TH850A.

Table 2 Arm 1 and Arm 2 overall mass of THE800 and TH850A

	THE800	TH850A
Arm 1 overall mass (kg)	8.92	12.12
Arm 2 overall mass (kg)	28.1	33.27

2.2.3 Axis 2 and 4 motor capacity reduction

THE800/TH1000 use lower capacity motors compared to TH850A by changing the reduction ratios of axis 2 and 4. Table 3 shows axis 2 and 4 motor capacities of THE800 and TH850A.

Table 3 Axis 2 and 4 motor capacities of THE800 and TH850A

	THE800	TH850A
Axis 2 motor capacities (W)	750	1000
Axis 4 motor capacities (W)	200	750

2.2.4 Reducing the number of components

THE800/THE1000 use a die-cast product with a high degree of freedom, making it possible to integrate the mechanical stopper and housing. In addition, the THE800 achieved a 6% reduction in the number of parts compared to the TH850A through measures such as base integration and sheet metal reduction.

2.2.5 New Controller

The controller TS5000-MS is used for THE800/THE1000, and its communication functions and programming language have been greatly improved compared to controller TS3100 used for the TH850A.

In an effort to reduce environmental impact, TS5000-MS has a 35% reduction in mass compared to TS3100 due to downsizing of

the controller. In addition, by placing all connectors in the front, the installation area has been reduced by 33% (including cable laying), resulting in the smaller control panel and reduced materials. Fig. 4 shows TS5000-MS appearance.



Fig. 4 TS5000-MS appearance

2.3 | Development DX Initiatives Using 1DCAE

In the development of THE800/THE1000, we promoted development DX incorporating 1DCAE and worked on the energy-saving design by model simulation. The following section describes the method.

2.3.1 | About 1DCAE

1DCAE is the design support concept, method, and tool which can be applied from the upstream design stage. In this study, one of its tools, drive torque simulation, enabled us to evaluate the kinematic performance of a prototype without fabricating the actual prototype.

2.3.2 | Driving Torque Simulation Procedure

The following procedure was used to simulate the drive torque of axis 1 and 2 combined motion of THE800 and TH850A.

a) Creation of simulation model

In the drive torque simulation, the simulation model was created by combining blocks called components. Fig. 5 shows the simulation model of THE800. Table 4 shows the inputs of the components used in the simulation.

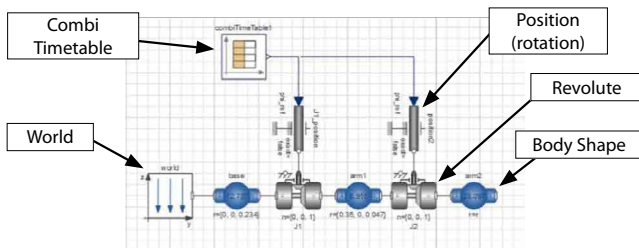


Fig. 5 Simulation model of THE800

Table 4 Inputs of components

Component	Input content
World	Gravity direction, Each axis direction
Position(rotation)	Nothing
Revolute	Rotation direction
Body Shape	Model center of gravity coordinates, Mass, Inertia tensor
Combi Timetable	Angular data of each axis by time series

b) Calculation of input parameters for Body Shape

The input parameters for Body Shape were calculated from the 3D-CAD data created at the time of design, divided into parts for Base, Arm 1, and Arm 2, and the center of gravity coordinates, mass, and inertia tensor of the model.

c) Calculation of angle data for Combi Timetable input

The angle data for the Combi Timetable was calculated under the condition the maximum torque can be obtained in axis 1 and 2 composite motion. Table 5 shows the calculation conditions, and Fig. 6 shows the graph of THE800 angle data.

Table 5 Component Inputs

	THE800	TH850A
Axis 1 operating range(deg)	-65⇔65	-86.5⇔86.5
Axis 2 operating range(deg)	-115.7⇔115.7	-130⇔130
Load(kg)	5	

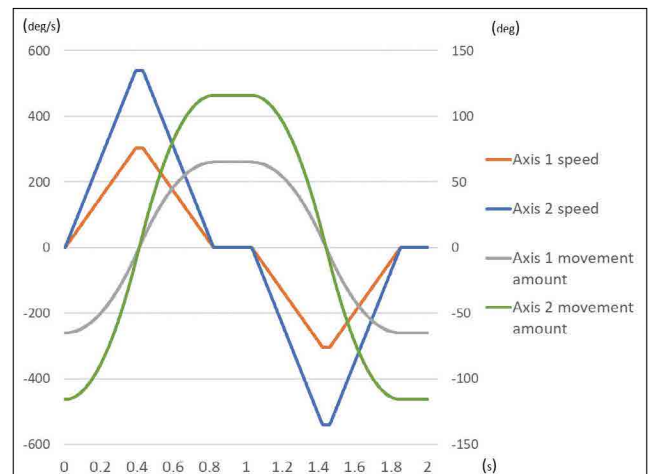


Fig. 6 THE800 angle data

d) Perform drive torque simulation

The values calculated in b) and c) were input into the simulation model created in a) and drive torque simulations were conducted. Fig. 7 and Fig. 8 show graphs comparing the results of axis 1 and 2 drive torque simulations for THE800 and TH850A, respectively. Table 6 shows Max and Min torque for axis 1 and 2.

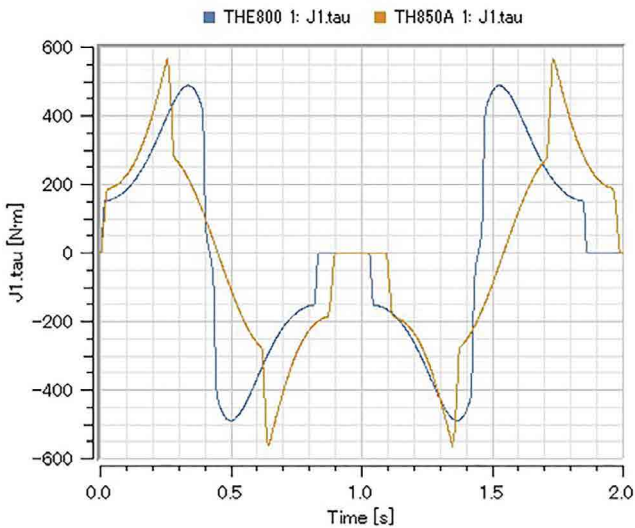


Fig. 7 Axis 1 drive torque simulations for THE800 and TH850A

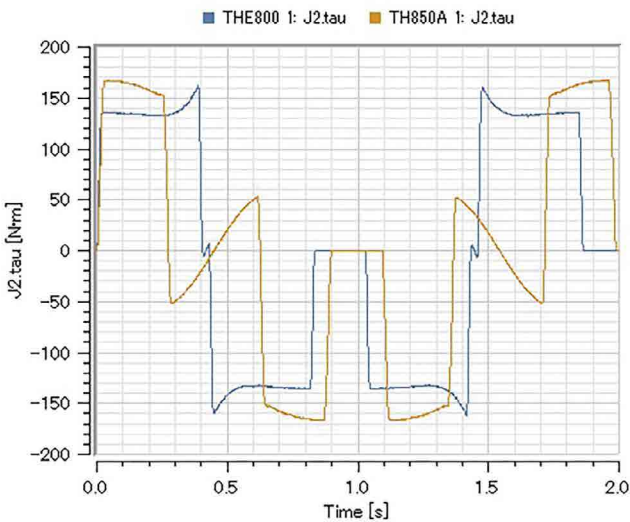


Fig. 8 Axis 2 drive torque simulations for THE800 and TH850A

Table 6 Max and Min torque for axis 1 and 2

	THE800	TH850A	Reduction
Axis 1 Max torque[N]	489.6	567.5	13.3%
Axis 1 Min torque[N]	-489.6	-565.2	13.4%
Axis 2 Max torque[N]	161.9	167.3	3.2%
Axis 2 Min torque[N]	-161.6	-166.9	3.2%

3 Effects on Environmental Impact Reduction

The environmental impact reduction measures in the THE800/TH1000 development described in the previous chapter and the development DX efforts based on the 1DCAE were evaluated using LCA (Life Cycle Assessment) based on the results of electricity consumption measurements for THE800 and TH850A. The results are described in the next section.

3.1 About LCA

LCA is the method for quantitatively evaluating the environmental impact of the product or service during its entire life cycle or at a specific stage. In this study, reductions (improvement values) were quantitatively evaluated by comparing projected CO₂ emissions.

3.2 Comparison of CO₂ emissions between THE800 and TH850A

To compare the CO₂ emissions of THE800 and TH850A, values measured from actual equipment are shown in Table 7.

Table 7 Actual measurement values for THE800 and TH850A

	THE800	TH850A	Reduction
Gross mass (kg)	46	76	39.5%
Oil consumption (g)	192	860	77.7%
Electric consumption at full load (kVA)	0.74	0.85	12.9%

Based on the measured values in Table 7, the life cycle CO₂ emissions of THE800 and TH850A were calculated and compared, and it was confirmed a 12.8% reduction is expected. Fig. 9 shows the graph comparing the life cycle CO₂ emissions of THE800 and TH850A.

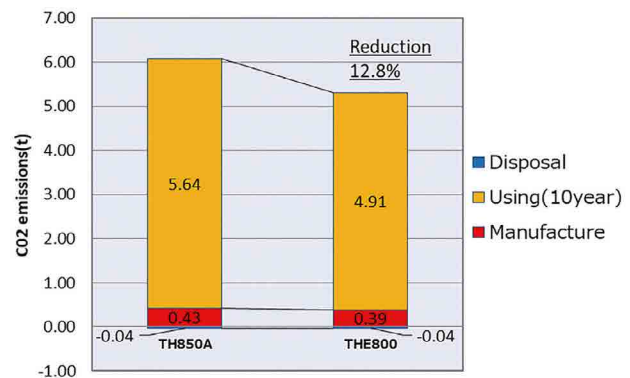


Fig. 9 comparing the life cycle CO₂ emissions of THE800 and TH850A

4 Conclusion

We introduced measures to reduce environmental impact in the development of THE800/THE1000 and design efforts using 1DCAE. These measures have resulted in a reduction in environmental impact compared to conventional models.

**Junji TAKETAZU**

Production Center
Machinery & Production
Engineering Department

I have been working at SMMT (Shibaura Machine Manufacturing Thailand: Thailand Plant) since the spring of this year and engaging in machining technical support with regard to locally procured parts.

The first issue one encounters at the local workplace is the “language” barrier. We can usually communicate smoothly with machining subcontractors in Japan by using machining terms and their interpretations without problem, but that is not the case with overseas plants where in many cases those terms cannot be understood by local people.

“Set-up for machining,” “deburring,” and “swing machining” are examples. It takes time and effort to make these expressions understood by local people by using words and 2-dimensional drawings. An exception to this the 3D modeling of products which is being promoted at the machining plant in Thailand. With this technology, we are able to share information such as the

3-dimensional shape of products and the issue, which is difficult to communicate using only “words”, and can be understood far more easily and quickly by adding “visual” information.

There are issues which can be solved by using new advancing technologies, but there is still an open issue. Workers at the machining worksite can sense the “cutting sound” and the “vibration” generated by the machine during the machining process, as well as the “tactile sense” on the machined surface, and they can use such information obtained in the adjustment of machining. Skilled workers in Japan can, in many cases, determine the machining state from such sensory observations, but it is often difficult to “demonstrate or express” those feelings. How can I explain and communicate those technical feelings which are hard to demonstrate to young workers overseas? That is the next issue I need to address.

Injection Molding Machine Upgradation from Induction to Energy Efficient Servo System

Shibaura Machine India has began its operations with the takeover of the plastic machinery business of Larsen & Toubro in 2012. The company manufactures advanced Injection molding machines and Auxiliary equipment since 1992. Its products cater to the needs of wide range of sectors such as automobiles, packaging, medical equipment, pipe fitting, consumer goods, electrical and agriculture.

Shibaura Machine India organized upgradation process of Injection molding machine manufactured at Shibaura Machine Japan (SMJ) as well as Shibaura machine India (SMI) from Induction system to Servo system. SMI executed more than 50 no. of machines for this retrofitment. Most of the retrofitment work was done at customer place.

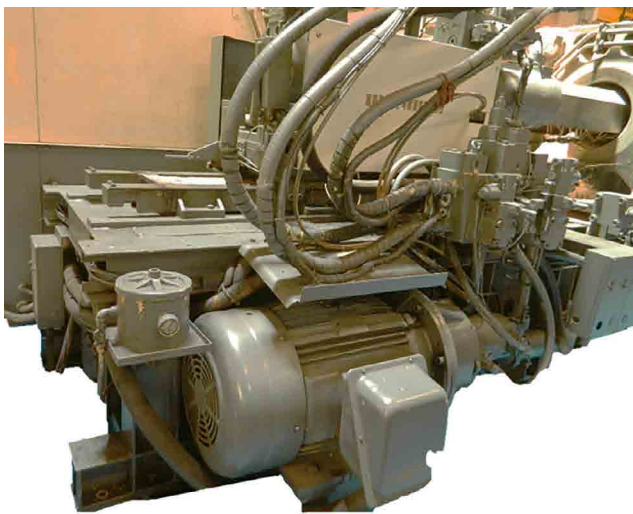


C.Somaskandhan
Head-Customer Service & Application
SHIBAUURA MACHINE INDIA PRIVATE LIMITED

Customer's are benefitted with followings:

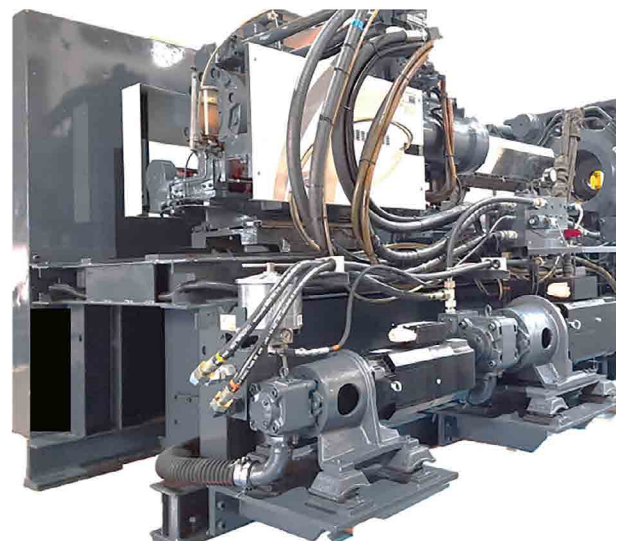
- ✚ Energy conservation: 30-40% or more in power saving
- ✚ Environmental impact on reduction in carbon footprint
- ✚ Noise level reduction from Maximum 90 dB to 80 dB
- ✚ Improvement on productivity and quality

Before retrofit



Japanese machine equipped with induction motor and binary multi-pumps

After retrofit



Field modification by using new technologies with servo motor and a single pump



Energy efficient Servo motor and pump system

Servo drive

Software

Some of the sample of retrofitment details & its benefits as below:

Sl.no	Machine model	Year of Manufacturing	Product	Energy saving	Environment impact	Customer voice
1	1300T (SMJ)	2003	Headlamp (Automobile -Cars)	60% and 33 kWh saved	Reduction of 23 kg CO ₂ equivalent	Highly satisfied with energy saving and technical support from SMI
2	850T (SMJ)	1993	Grill radiator (Automobile -Cars)	42% and 25 kWh saved	Reduction of 18 kg CO ₂ equivalent	Performance of machine improved, will plan for next machine upgradation
3	200T (SMI)	2003	Writing instrument (Pen)	41% and 22 kWh saved	Reduction of 15 kg CO ₂ equivalent	Machine performance is on par with new machine

Introduction of the Electric Sub-Injection Unit EC PLUS⁺

1 Overview

A long time has passed since multi-color, multi-material molding became a practicable injection molding technology which enables higher functionality, such as enhanced design flexibility for molded products, as well as production process integration. However, this technology requires not only special molds but also an injection molding machine of dedicated design. This means higher levels of capital investment are needed, becoming a barrier to smooth introduction of the technology into production sites. To avoid this problem, there is a solution consisting of inserting a premolded component into the molding machine and performing additional resin molding. But with this solution, the process is complicated and the production efficiency is low as compared with use of a dedicated machine. To solve these disadvantages, we have developed the Electric Sub-Injection Unit EC PLUS⁺, which is a reasonable add-on device for the all-electric injection molding machine of the EC-SXIII series. The following describes its main features.

2 Features

(1) Electric Sub-Injection Unit EC PLUS⁺

The EC PLUS⁺ is a secondary injection device which is added to the injection molding machine separately from the main injection device of the machine to charge into the mold a different resin material from that injected by the main injection device. Fig. 1 shows the appearance of the EC PLUS⁺ and Table 1, the specification values of the unit. In designing the unit, its application was confined to multi-color, multi-material molding aiming at a limited resin amount (or screw diameter), reduced space, and compact structure. In consequence, we were able to achieve reduced external dimensions as compared with the injection device^{*1} of a general purpose molding machine: a reduction of 130 mm (10%) in overall length, a reduction of 130 mm (20%) in width, and a reduction of 170 mm (50%) in height^{*2}.

*1 Screw diameter $\phi 18$

*2 Dimension from screw center to cover's top surface

(2) Scalability

The EC PLUS⁺ employs a modular structure so it can be added relatively easily even to standard EC-SXIII machines already delivered to customers. The machine with the EC PLUS⁺ added can be easily brought back to its original state, which means high flexibility in terms of changing the equipment allocation according to changes in production demand for multi-color, multi-material molding. The unit is compact as above described, and stands have been developed which enable installing the unit either vertically or horizontally. These two features make it possible to fill the material into the mold in any of three directions (from the top side and both lateral sides).

(Fig. 2)

Table 1 Specification Values

	Unit	Selection Specifications			
		$\phi 18$	$\phi 20$	$\phi 22$	$\phi 25$
Screw Diameter	mm	$\phi 18$	$\phi 20$	$\phi 22$	$\phi 25$
Screw Stroke	mm	72	80	88	100
Injection Volume Calculated	cm ³	18.3	25.1	33.5	49.1
Injection Pressure	MPa	200	200	200	160
Holding Pressure	MPa	150	150	150	150
Injection Speed	mm/s	180	180	180	180
Injection Rate (MAX.)	cm ³ /s	45.8	56.5	68.4	88.4
Screw Torque	Nm	61.0	82.0	107.0	153.1
Maximum Screw Speed	min ⁻¹	480	430	420	420
Plasticizing Capacity(PS)	kg/h	12	14	22	28
Nozzle Touch Force	kN	5.8	5.8	5.8	5.8

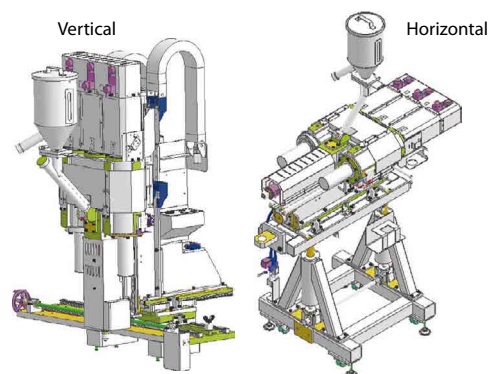


Fig. 1 Appearance of the EC PLUS⁺

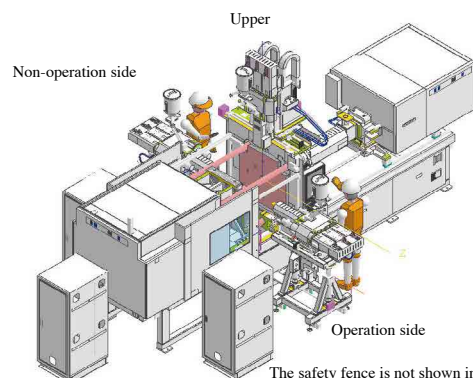


Fig. 2 Installation layout of the EC PLUS⁺

Another advantage of the EC PLUS+ is it is not necessary to construct a structure to link this injection device to the mold or work the mold in any way, which means existing molds for multi-color, multi-material molding can be easily used with this device.

(3) Operability

For an EC-SXIII series machine provided with the 'INJECTVISOR V70', injection setting can be performed for both the main and sub units on the operation screen of the machine with the on-screen control panels adjacently displayed^{*3}. (Fig. 3) In general, the operation screen of an add-on type sub-injection device is added separately from that of the machine, and the set-up condition and operation monitoring data for the main and sub-injection devices are independent from each other. Therefore, integrating the management of these factors made it necessary to devise a solution. On this machine, data management for the main and sub-injection devices is performed in an integrated fashion, simplifying the process. In the IoT utilization of production facilities represented by Industry 4.0, centralized management of production data is essential. The next version of the injection molding machine remote management system 'iPAQET' to assist such data management will support dual-material injection molding. (Fig. 4)

*3 Adding two or more sub-injection device requires additional operation screens.

(4) Linking with an electric rotary table

An extension unit developed separately from the electric sub-injection unit is an electric rotary table. (Fig. 5) An electric rotary table is an extension unit which rotates the mold attached to the movable board in the multi-color, multi-material injection molding process of the core rotating type. After the first material is filled into the mold by the injection device of the molding machine, the mold is rotated by the electric rotary table and then the second material is filled by the EC PLUS+. (Fig. 6) This electric rotary table is also designed as an add-on device for a general-purpose machine. Thus, multi-color, multi-material molding, which in the past required the installation of a dedicated injection molding machine, can now be realized at a relatively low cost.

Models supported: EC100SXIII, EC230SXIII, EC350SXIII

3 Conclusion

The newly developed 'Electric Sub-Injection Unit EC PLUS+' incorporates as standard our control technologies, which have been cultivated through the development of electric injection molding machines and enable high-precision stable molding to be realized. Moving forward we will refine these basic technologies and

contribute to the realization of unprecedented ideas while working closely with our customers in their product development activities. We intend to offer, at reasonable prices, functionality extensions for the injection molding machines our customers purchased, and to push forward with further product development to be able to help our customers realize high value-added molding relatively easily.

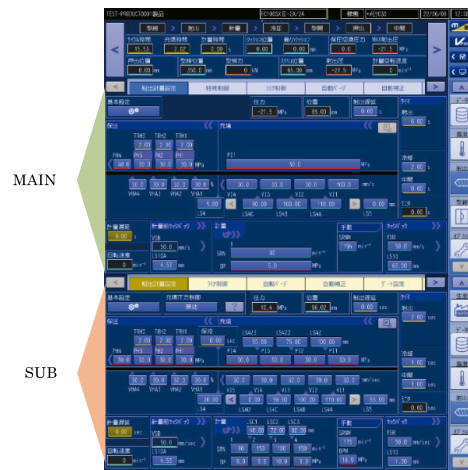


Fig. 3 INJECTVISOR V70 operation screen

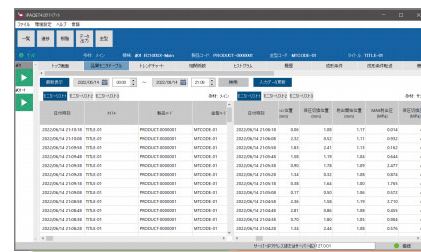
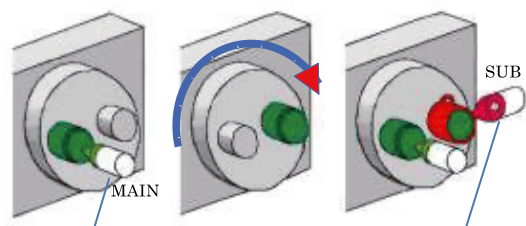


Fig. 4 iPAQET monitoring screen



Fig. 5 Electric Rotary Table



Inject 1st material → Rotate the mold → Inject 2nd material
Fig. 6 Core rotation type dual-material molding

Introduction of the DC400R2 Die Casting Machine



Fig. 1 DC400R2 Appearance

1 Overview

Recently, as a result of the growing concern for energy conservation, companies in the die casting industry have been asking for equipment which can reduce their environmental impact. This paper introduces the DC400R2, which can be equipped with an electric servomotor-driven toggletype mold clamping mechanism and a servo-hydraulic source which controls flow rate and pressure using a servomotor. (Fig. 1)

2 Features

1) Energy saving by electric clamping

The electric drive structure of the DC400R2 is shown in Fig. 2.

The combination of a ball screw and servomotor enables smooth acceleration/deceleration control with smaller energy loss than hydraulic drives enabling energy-saving results.

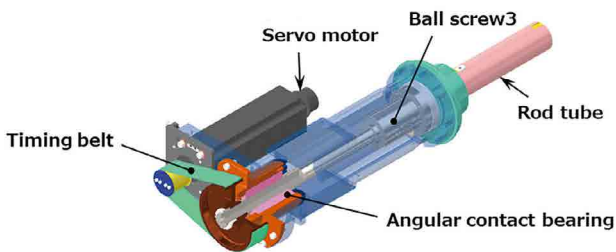


Fig. 2 Electric Drive Unit

Table 1 shows a comparison of the power usage and time for mold opening and closing when using hydraulic and electric clamping. Electric clamping uses less power and shortens the cycle time enabling improved productivity.

Table 1 Energy-saving Effects by Use of Electric Clamping

		Hydraulic	Electric	Difference
Power usage	(kW)	12.2	7.0	5.2
Mold opening/closing time	(sec)	4.0	2.7	1.3

*Measurement results with no mold installed and at 100% speed

2) Energy saving by servo-hydraulic source

In standard hydraulic power sources, the hydraulic pump is driven by an induction motor which rotates at a constant speed, and the oil discharged from the pump has its pressure and flow rate adjusted by a pressure flow control valve, which returns unneeded oil to tank. This is where energy loss occurs (Fig. 3).

Standard Hydraulic Source

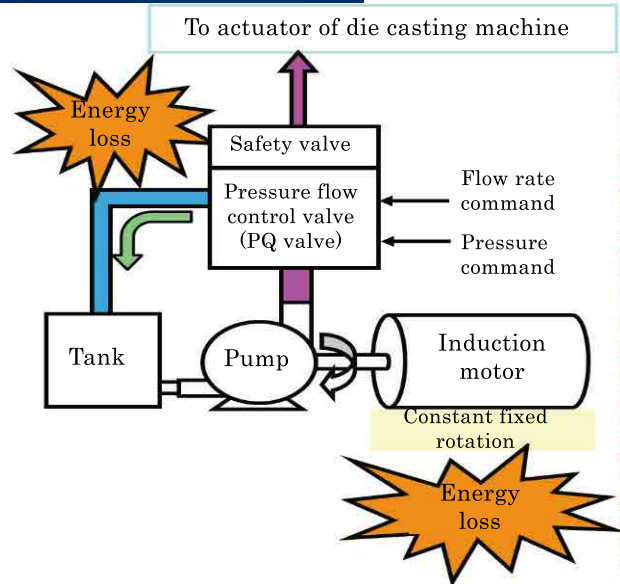


Fig. 3 Configuration of Standard Hydraulic Power Source

In contrast, in servo-hydraulic sources, the hydraulic pump is driven by a servomotor, the flow rate is controlled by the motor speed, and the pressure is controlled by feeding back the hydraulic circuit pressure to a servo amplifier. This makes it possible to reduce power usage without energy loss (Fig. 4).

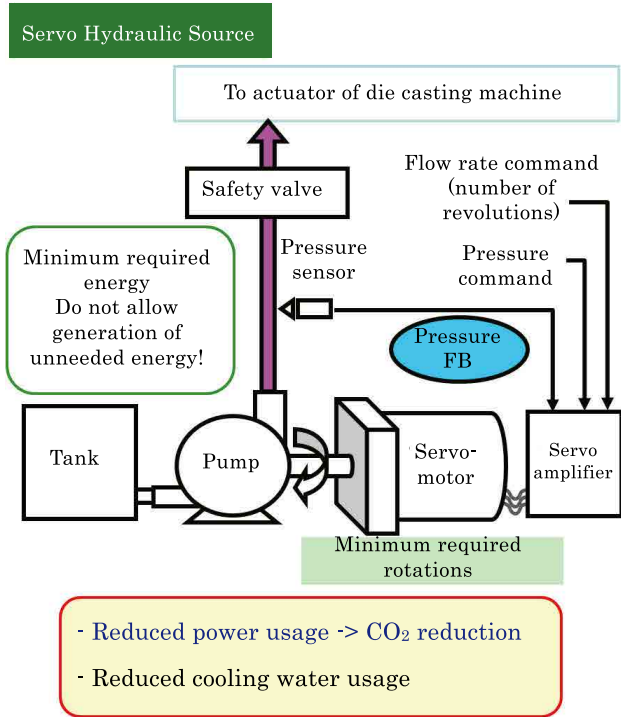


Fig. 4 Configuration of Servo-hydraulic Source

A table comparing the power usage of standard and servo-hydraulic sources is shown in Table 2. Power usage can be reduced by about 34% by installing a servo-hydraulic source.

Table 2 Energy-saving Effect by Use of Servo-Hydraulic Sources

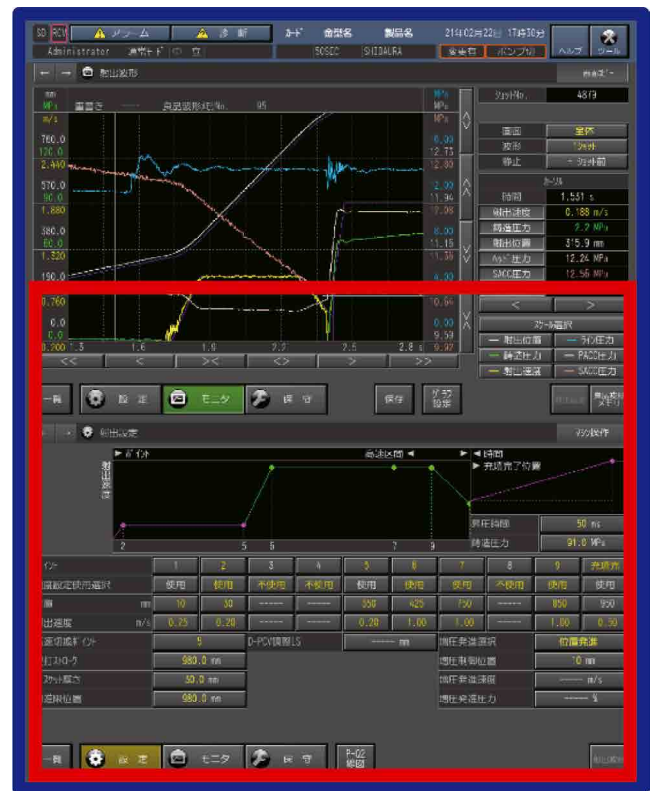
		Standard hydraulic source	Servo-hydraulic source	Reduction rate (%)
Power usage	(kW)	15.9	10.4	34.6

*Cycle time 30 (sec)

3) New controller

The controller is equipped with the newly developed large-screen TOSCAST-999 (Fig. 5). To take advantage of the larger screen, the GUI enables user operation on two screens, an upper and lower screen, for reducing the number of screen-switching operations and allows the user to change conditions while viewing the monitor and to display waveform and line data simultaneously for greatly improving ease of operation.

This controller can also display documents required by the user, such as ladder program circuits, instruction manuals, and system diagrams, for contributing to improved ease of operation and environmental conservation through paperless operation.



Red box: Previous screen size (298 x 375 (mm))

Blue box: New screen size (447 x 375 (mm))

Fig. 5 TOSCAST-999 Controller

3 Specifications

Table 3 shows the specifications for the DC400R2. Compared to the previous model, the DC350R, the new model has a higher die clamping force (3500 ⇒ 4000 kN) and larger die plate size (935 × 935 ⇒ 960 × 955 mm) for improved product appeal and higher productivity for the user.

Table 3 DC400R2 Specifications Table

		Units	DC400R2
Die clamping	Die clamping force	kN	4000
	Die plate size (V x H)	mm	960×955
	Tie bar spacing (V x H)	mm	650×650
	Tie bar diameter	mm	135
	Die thickness	mm	300 to 700
	Die stroke	mm	420
Injection	Maximum injection force	kN	344
	Intensification ratio		1:2.07
	Plunger stroke	mm	480
	Tip protrusion amount	mm	265
	Injection port position (from machine center to below)	mm	150
	Injection speed	m/s	0.3 to 6.5
Extrusion	Tip diameter (standard)	mm	60 to 80
	Extrusion force	kN	190
Hydraulic	Extrusion stroke	mm	20 to 90
	Number of moving cores	Set	3/8"×1
	Moving core port (per solenoid valve)	Set	3/4"×2
	Hydraulic fluid pressure	MPa	15
	Required hydraulic fluid amount	L	450
Dimensions	Hydraulic fluid tank capacity	L	480
	Footprint (with electric clamping)	mm	6335×2346
	Machine height	mm	3076

4 Results and Examples

- 1) Energy-saving effects by installation of electric clamping
⇒Power usage reduction rate: approx. 42%
- 2) Energy-saving effect by installation of servo-hydraulic source
⇒Power usage reduction rate: approx. 34%
- 3) Electric clamping for improved productivity
⇒Cycle time reduced by 1.3 sec
- 4) Increased clamping force and die plate size for improved product appeal and productivity
⇒Improved quality of user molded products
- 5) New controller for improved ease of operation
⇒Larger screen reduces screen-switching time and enables display of the required information on the user's screen for higher work efficiency

5 Conclusion

The DC400R2 is the latest model with features capable of contributing to energy savings and higher productivity. Shibaura Machine will continue to expand its lineup in the future to better meet the needs of our customers.

COLUMN

Language Processing and Internationalization



Masakazu KANEMOTO

Former engineer of Shibaura Machine Co., Ltd.

Once, when I was working in a robot-related project, I went on a business trip to London with Mr. W, a young engineer who loved books. On a holiday during the trip, I visited Foyles book shop in London as he recommended. Foyles Co.

started bookselling in 1903 when the Foyle brothers, after having failed their civil service exams, started selling off a pile of unwanted textbooks they had and received orders which outnumbered the books on hand. It is now one of the largest book shops in England.

I was surprised to see the shop had one floor which was entirely dedicated to English education and was full of books in the field. Looking at the array of English education textbooks for many different countries, including of course those which used to be colonies of Britain, as well as Southeast Asian countries, China, Japan, and Latin American countries, I thought I understood the reason why English has been spreading all around the world as an international language.

In recent years, it has become easier and more convenient for me to read overseas news and articles on the Internet because they can be automatically translated from English into Japanese.

They say the automatic translation system, which has been a success in the artificial intelligence field, is making great contributions. In the automatic translation process, practical sentences are composed by using big data, in combination with techniques such as occurrence probability, to determine the most probable idiom which applies to a certain sentence.

I was surprised at the very rapid pace at which information about COVID-19 in overseas English language articles is distributed to medical experts in Japan. I suppose it is partly due to the help of an automatic translation function provided on the Internet. In addition, the number of young overseas tourists visiting Japan is increasing, which, I think, is largely because they have easy access to information on Japan available on the Internet through an automatic translation system on their smartphones to translate into their own languages.

Introduction of the High-End Model MP-2620(U), a Double-Column 5-Axis Multitasking Machine

1 Overview (Background and Aim of Development)

Recently, the shortage of operators, limited space for machine installation, and higher accuracy for large parts have become issues, and multitasking machines capable of reducing the number of setups are attracting growing attention. As the market moves toward decarbonization; wind power, hydroelectric power, and hydrogen gas turbines are expected to become major industries in the future, and demand for 5-axis multitasking machines is expected to increase as more workpieces will require turning and 5-axis machining. Shibaura Machine has its MP-U series of 5-axis multitasking machines, but more than 10 years have passed since its launch, and there is an urgent need to improve its product value.

In addition to inheriting the superior features of the attachment change function and machining of the entire table-top surface area, which are not found in multitasking machines from other companies, this new machine was also designed with improved performance of its 5-axis head, which further differentiates it from competitor products.

This machine includes the following features.

- Simultaneous 3-axis turning using a swivel head (A-axis)
Extended stroke to enable use of long tools
- Attachment indexing at any angle

The machine appearance is shown in Fig. 1.

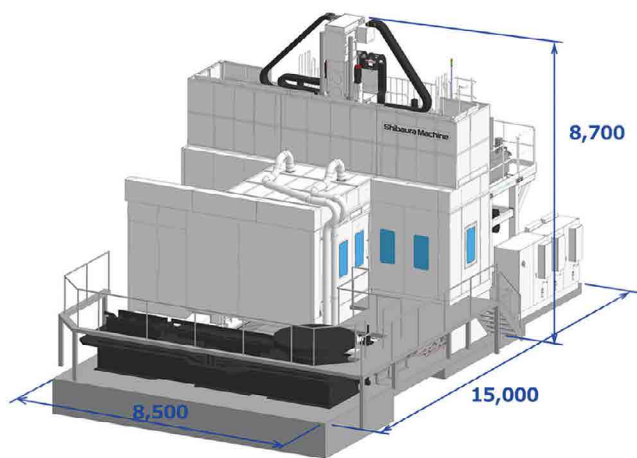


Fig. 1 MP-2623(U) Appearance

2 Features

2.1 | Includes FANUC Numerical Controller

This machine incorporates the FANUC Series 30i-B Plus controller which adds a dialogue function not available in previous models. The machine collision prevention function detects machine collisions in both manual and automatic modes to prevent damage to the machine.

The machine body was designed with a new turning spindle, CT-axis drive assembly, and linear axis feed assembly for maximum FANUC capability.

2.2 | Optimization of Machine Stroke

The X and Z axes have been extended to accommodate a wider range of axis travel when a long tool is used. This also enables workpiece retraction during tool change, attachment change, and tool measurement for improved ease of use.

2.3 | Includes KESSLER 5-axis head

A KESSLER's 5-axis head C-axis is installed in the 650 mm ram, and the swivel head (A-axis) is positioned at the lower end of the ram as shown in Fig. 2. In this 5-axis head, the C-axis and swivel head are separable so the swivel head can be mounted and removed as an attachment.

Furthermore, this 5-axis head has a spindle lock function not found in previous machine models. The A- and C-axis shaft torque and clamping capacity have been improved over those of previous machine models.

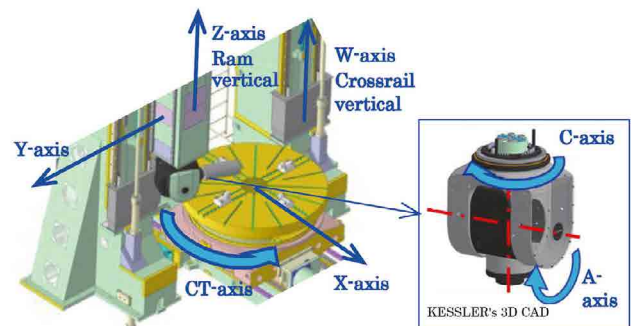


Fig. 2 Machine Coordinate System

2.4 | Use of Attachment Change System

As explained in section 2.3, an attachment mounting/removal system is used. Other than the swivel head, a KESSLER snout, a horizontal turning head, and a vertical turning head are provided as standard. A turning head is used to enable inner diameter machining for small diameters.

2.5 | Tool Interface

Shibaura Machine turning tools had a special shape which prevented interchangeable use with conventional turning tools, but this machine uses the standard HSK-T type tool shank system.

2.6 | Automatic Tool Measurement Device

A laser measuring instrument is used to measure the milling tool length and diameter, and a touch probe is used to measure the turning tool edge. The instrument unit is located at the right-side stroke end of the Y-axis, and the location of the measurement device is changed according to the measurement application.

3 Specifications

The specifications are shown in Table 1.

Table 1 Main Specifications

Item	Main Specifications
X-axis travel (mm)	3,200
Y-axis travel (mm)	3,400
Z-axis travel (mm)	1,500
W-axis travel (mm)	2,000
CT-axis travel	360° (continuous)
A-axis travel (Op.)	±110°
C-axis travel (Op.)	±360°
Distance between columns (mm)	2,600
Column height (5-axis head)	2,040
Table size (mm)	Φ2000
Table maximum loading weight (kg)	10,000
X, Y-axis rapid traverse rate (m/min)	30
Z-axis rapid traverse rate (m/min)	20
CT-axis rapid traverse rate (deg/min)	1,080
A, C-axis rapid traverse rate (deg/min)	14,400
Spindle rotational speed (min ⁻¹)	50 to 6,000
Max. spindle rotation force (Nm)	500
Spindle clamp torque (Nm)	1,400
Table spindle rotational speed (min ⁻¹)	2 to 250
Max. table rotation force (Nm)	20,000
Ram size (mm)	650
A-axis servomotor torque (Nm)	2,200 (S1)
A-axis clamp torque (Nm)	7,400
C-axis servomotor torque (Nm)	2,500 (S1)
C-axis clamp torque (Nm)	12,500

* **Bold type** indicates changes in specifications from the previous model.

4 Results and Examples

4.1 | Simultaneous 3-Axis Turning

The spindle lock function holds the turning tool in place, and simultaneous 3-axis turning including the A-axis enables machining of complex-shaped workpieces with a single tool. (Fig. 3)

4.2 | Machine Strokes Compatible with Swivel Head

The extended X- and Z-axis strokes provide sufficient machining stroke even when a long tool is mounted on the swivel head for increasing the number of workpieces which can be machined, improving ease of use. (Fig. 4)

4.3 | Enables Attachment Indexing at Any Angle

Previously, attachment indexing (AAI) was 1° indexing by curvic coupling, but this machine enables indexing at any selected angle by clamping the C-axis after positioning the attachment on the C-axis. (Fig. 5)

4.4 | NC Functions

NC functions such as a dialogue function, machine collision prevention function, workpiece setup correction, spindle tip point control, and tool measurement function have been enhanced with NC unit FANUC compatibility for improving their ease of use.



Fig. 3 Simultaneous 3-Axis Turning

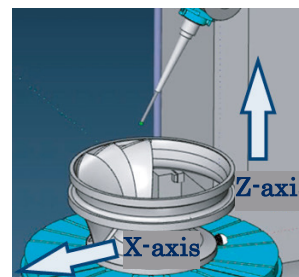


Fig. 4 Use of Long Tool

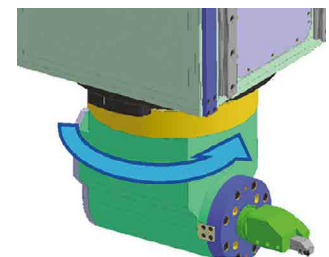


Fig. 5 Attachment Indexing at Any Angle

5 Conclusion

This MP-U model will be a high-function, upper price-range model, but we plan to draw sales interest by using actual machines to demonstrate its new functions not found in previous models and by enhancing our sales promotion materials.

Introduction of the High-Speed Rotating Work Spindle for High-Precision Aspheric Surface Grinders

1 Overview

The ULG/ULC series of high-precision aspheric grinders are lathe-type machine tools mainly used for cutting and grinding of optical lens molds and for direct grinding of glass lenses. From its initial development in the 1980s to the present day, Shibaura Machine has grown its market share by being constantly receptive to market demands.

For example, the ULC-100F(S), which specializes in turning, has an ABC-80MP work spindle on the Z-axis and a tool mounted on the Y-axis column on the X-axis, enabling simultaneous 2-axis control with 0.1 nm control to machine complex aspheric shapes such as smartphone-mounted lenses. Fig. 1 shows the machine configuration of the ULG-100D (5A) 5-axis aspheric grinder. The machine is capable of simultaneous 5-axis control, including 3 linear axes (X, Y, Z) and 2 rotational axes (B, C), and can perform cutting and grinding operations in various setups by changing the tool spindle and tool rest according to the workpiece.

The ABC-80MP, which is mounted as the work spindle of the ULG/ULC series, is suitable for high-precision machining which achieves extremely low vibration rotation and low rotational irregularity by combining an aerostatic bearing with a porous restrictor system and a built-in induction motor with encoder. However, in addition to high accuracy, the machine must also be able to rotate at high speeds to increase productivity. In response to these requirements,

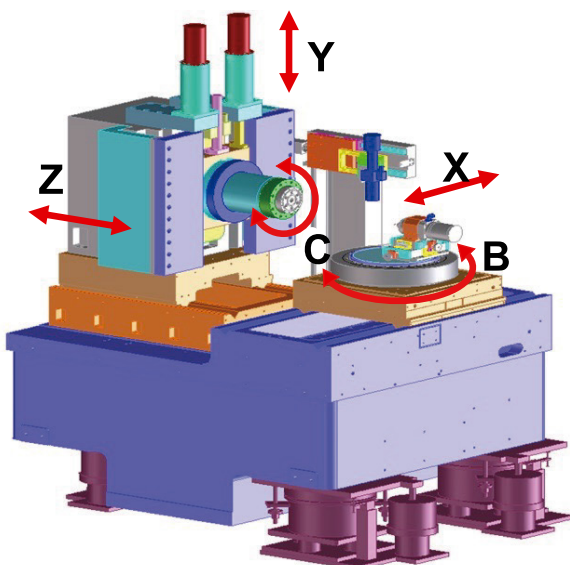


Fig. 1 Mechanical Configuration of ULG-100D (5A)

we have developed a high-speed work spindle capable of achieving up to a maximum speed of 3000 min^{-1} , compared to the previous maximum speed of 1500 min^{-1} , and this work spindle is introduced in this report.

2 Features

Since aerostatic bearings levitate and hold the rotating shaft by the static pressure of compressed air, frictional heat during rotation is minimal compared to standard bearings. However, frictional heat is generated in the bearing clearance at high-speed rotation due to air shear resistance, causing elongation of the spindle. This elongation can be saturated with sufficient warm-up time, but in high-precision machining, elongation of a few microns is critical, and several hours of warm-up time is a significant loss of production opportunity. Therefore, the saturation time was reduced by reviewing the bearing structure and cooling circuit. Fig. 2 shows the temperature change and the amount of elongation as the new structured work spindle rotates, showing the elongation saturates at about 1 hour and the amount of elongation is kept below 1 μm .

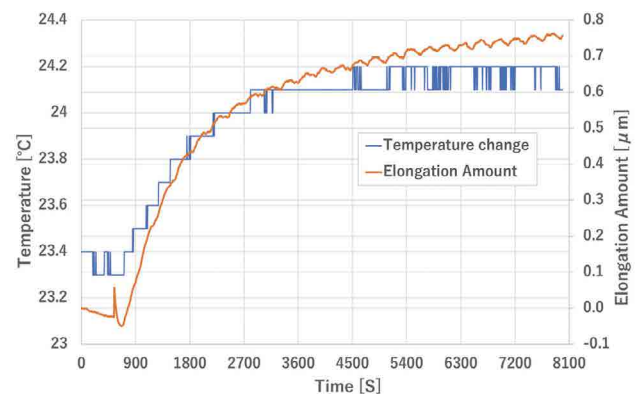


Fig. 2 Temperature Change and Elongation of New Structure Work Spindle

3 Results and Examples

This presents a practical case study of the high-speed ABC-80MP.

First, large-diameter lenses are used in broadcasting lenses for shooting 4K and 8K images and in projection lenses for semiconductor lithography equipment. However, when machining large-diameter workpieces exceeding 100 mm in diameter using standard high-accuracy machine tools, high-quality machining is

often difficult because the load on the workpiece clamping mechanism is large, the grinding wheel size is limited, and the appropriate machining conditions cannot be obtained. In contrast, the ULG-100D (5A) can perform machining by using the ABC-80MP as the grinding spindle and the B-axis (ABC-240MP) as the work spindle, but previously the rotation speed was not sufficient, and machining could not be performed under the appropriate machining conditions. Now, with the higher speed rotation capability, machining can be performed at the proper rotation speed, and the ABC-80MP, which has higher rigidity and torque than the standard grinding spindle, enables stable machining for large-diameter workpieces.

Next, the ULC-100F (S) has been adopted in many cases as a finishing machine for molds for smartphone camera lenses. However, with the increase in the number of lenses produced due to the increasing popularity of smartphones and the growing use of multifocal cameras mounted on them, there is a need to improve machining efficiency. To increase the machining efficiency, the feed rate must be increased, but to maintain surface quality, the workpiece rotation speed must be increased at the same time as the feed rate. Lens molds for smartphone cameras require extremely high machining quality with a shape accuracy of P-V 50 nm or less and a surface roughness of Ra 0.3 nm or less, and the vibration of any mechanical element can affect the surface quality. This machine has extremely low vibration in the normal rotation range, but at high speeds, rotational vibration is caused by various factors and deteriorates the machined surface quality, and so the machine is only operated at work spindle speeds in the range of 800 to 1000 min^{-1} .

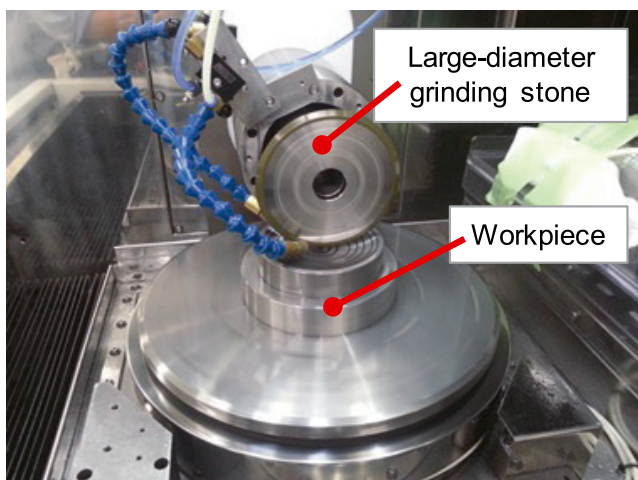


Fig. 3 Machining of a Large Aperture Lens

In addition to the new structure described in section 2, we optimized the motor and its control parameters in the high-speed range. As a verification of the effect, the Z-axis torque values were compared. Rotational vibration of the spindle is transmitted to the Z-axis and vibrates in the Z-axis direction, which is the cutting edge cutting direction, leading to deterioration of the machined surface quality, and so the strength of the vibration can be evaluated by looking at the Z-axis torque value. A spectrogram of frequency analysis of Z-axis torque values (before and after improvement) is shown in Fig. 4. In the improved work spindle, the peak (horizontal stripe) in the 600 to 800 Hz band is weakened, confirming the rotational vibration of the work spindle, which affects the Z-axis vibration, has been reduced. Going forward, through further optimization, Shibaura Machine aims to develop a high-productivity work spindle which can provide high-quality machined surfaces even at high speeds.

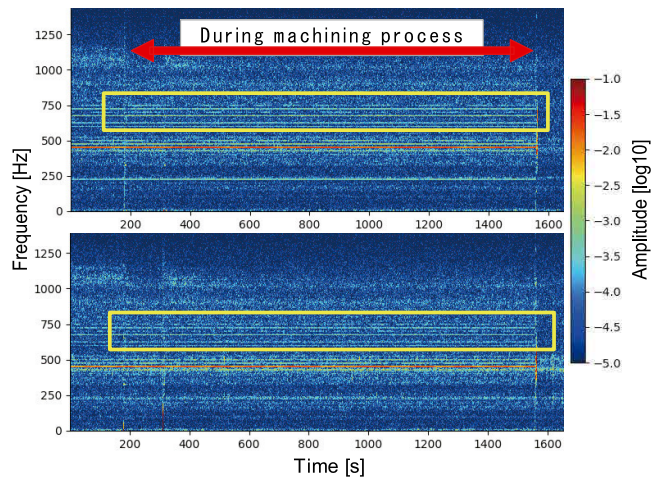


Fig. 4 Spectrogram at 3000 min^{-1}
(Top: Before improvement, Bottom: After improvement)

4 Conclusion

By improving the structure and various conditions of the ABC-80MP work spindle, higher speeds and higher accuracy have been achieved for the work spindle. We will continue to further delve into the application results for this work spindle and expand the scope of its application through further development.

Introduction of the TCmini Series TC11-03 Temperature Control PLC

1 Overview

The TCmini series models feature a combination of a micro-controller board which can be programmed in ladder language (PLC language) with a control device which can provide the optimal functions, size, and cost to match customer needs.

The TC5-03 model has been used as a "temperature control PLC" in a wide range of fields such as industrial equipment and food and kitchen equipment. To meet further market needs, we have developed the new TC11-03 which features even higher performance and expanded functions for temperature control.

A new MCU^{*1} is used to achieve higher control performance and expanded functions while maintaining installation and functional compatibility with the previous TC5-03 model.

*1 MCU (Microcontroller Unit): An embedded microprocessor which incorporates many peripheral functions such as ROM, RAM, and other memory and I/O-related functions in a single integrated circuit.

2 TC11-03 Features

- (1) Improved control performance: Ladder processing time is halved from the previous model;
- (2) Ladder program capacity: 1.3 times that of previous model;
Data register capacity: 4 times that of previous model;
- (3) Enhanced temperature control (temperature input):
Sampling cycle: 4 times faster than previous model;
Reference temperature can be read for each channel (previously common to all channels) for improved noise resistance.
- (4) Enhanced network functionality: Ethernet communication, USB communication;
Ethernet communication: Modbus TCP master/slave support;
- (5) Expanded functionality:
Additional 3 x 4-20 mA inputs and 1 x 4-20 mA output compared to previous model;
Enables one additional RS485 communication port and one additional thermocouple input;
- (6) Fewer mounting parts:
Use of fewer mounting parts enables single-sided mounting (previous model used double-sided mounting).

3 Specifications

Table 1 TC11-03 Main Specifications

Item	TC11-03	TC5-03 (Previous model)
Supply voltage	DC24V	DC24V
Dimensions	150(H)×220(W)	150(H)×220(W)
Ambient operating temperature	-10°C to 60°C	0°C to 60°C
USB communication (for development)	1 port	-
Ethernet communication	1 port	-
Thermocouple input	6 ports	5 ports
Serial communication	3 ports	2 ports
Analog input/output	4 ports/2 ports	1 port/1 port
General-purpose input/output	8 ports/12 ports	8 ports/12 ports
Component mounting surface	Single-sided mounting	Double-sided mounting
Panel interface	1 port	1 port
Processing time	5 ms max. at 4 kW	10 ms max. at 4 kW
Program capacity	32 kilowords	24 kilowords



Fig. 1 TC11-03 Appearance

4 Results and Examples

The TC11-03 has enhanced communication functions such as Ethernet communication and USB communication, which have been requested by customers, as well as improved temperature control performance for supporting smart factory implementation.

Also, the TC11-03 has even fewer parts than the previous model, which was an eco-friendly product.

Application Examples

Industrial equipment: Hot air dryers, die cooling equipment; Food and kitchen equipment: Steam ovens, conveyor oven.

Introduction of the Robot Controller TS5000-EMS

1 Outline

In 2011, we launched the TSL3000, the current mainstay of our robot controller lineup, and have since developed a series of high-power and EU Directive-compliant versions of these controllers. In 2019, we launched the TS5000-MS controller, which is compatible with the high-speed, high trajectory accuracy SCARA robot THE600, with significant improvements in communication functions and programming language from the previous TS3000 series. In 2021, the TS5000-EMS was developed for Europe in compliance with the latest EU directives.

2 Features

The TS5000-EMS is based on the TS5000-MS, and the circuits and components of the safety section have been changed to comply with various safety standards and integrated to minimize the increase in external dimensions. In addition, while securing a motor amplifier capacity which can accommodate large models (THE800/ THE1000) in the future, the new model is fully EU Directive compliant (*Note 1) with no external components and only the main unit. The appearance of TS5000-EMS is shown in Fig. 1.



Fig. 1 Appearance of TS5000-EMS

The TS5000-EMS emergency stop, teach pendant enable switch and safety door signal handling can be enhanced with the addition of a safety relay module to more reliably stop the robot even in the event of component failure.

Table 1 shows the EU Directives to which the TS5000-EMS and the SCARA Robot THE400-E/THE600-E can be combined, and their safety performance is shown in Table 2.

Table 1 EU Directives to which the TS5000-EMS conforms

Machinery Directive 2006/42/EC	Low Voltage Directive 2014/35/EU	EMC Directive 2014/30/EU
EN ISO10218-1:2011 EN ISO12100:2010 EN ISO60204-1:2018 EN ISO13849-1:2015 EN ISO13850:2015	EN61800-5-1 :2007/A1:2017	EN55011 A1:2017 EN61000-6-4:2019 EN61000-6-2:2019 EN61800-3:2018 Emission: PDS of category C2 Immunity: Second environment

Table 2 Safety performance of TS5000-EMS

ISO13849-1:2015 Safety category	ISO13849-1:2015 Performance Level
Category 3	PL=d

For standards compliance, we obtained TÜV Mark certification and safety standard conformance certification from TÜV SÜD, a third-party organization. The certificate is shown in Fig. 2.



Fig. 2 TÜV Mark certification (left) and certificate of conformity (right)

In addition, all components used have been confirmed to be compliant with the RoHS2 directive, making them environmentally friendly products.

The company will gradually conform to the KCs Mark (Korea) and TS Mark (Taiwan) to meet the demands of customers in the global market.

*Note 1: In the case of small controller enclosures, some manufacturers respond by adding external filters and other countermeasure components externally.

3 Specifications

Specifications of TS5000-EMS are shown in Table 3.

Table 3 Specifications of TS5000-EMS

Item	Specifications	
Model	TS5000-EMS	
Number of controlled axes	4 axes	
Servo type	Digital servo	
Position detection method	Absolute type	
Main memory	Controller built-in FlashROM Capacity: 12 MB	
Auxiliary memory	SD card (SD, SDHC) Maximum capacity: 32 GB	
Number of file stores	Main memory : Max. 512 Auxiliary memory : Max. 512	
Maximum number of program lines	Per program Data section 5000 points Program section 5000 lines	
Programming language	SCOL2(Dedicated language)	
Operation command	PTP, CP (line, arc), shortcut, arch	
Speed setting	Override/Speed limit/Program instructions, 1 to 100% for each instruction	
Acceleration setting	Program instruction: 1 to 100%	
Torque Control	Program instruction: 1 to 300%	
Coordinate system	The Base, Workpiece, and Tool coordinates can be set.	
Teaching device (Option)	Teach pendant : TP5000 PC software : TSAssist	
Communication function	Ethernet 1 ch (1 Gbps) Non-protocol communication, Host command communication, Internal PLC communication, etc.	
I/O	General-purpose	8 inputs/8 outputs
	System	13 inputs/9 outputs
	Hand	8 inputs/8 outputs
Dimensions(mm)	410 (W) × 161 (H) × 350 (D)	
Weight	13kg	
Power supply	Single phase 190 to 240 VAC, 50/60 Hz	
Option	External I/O(21 inputs/17 outputs) Fieldbus functions (CC-Link, EtherNet/IP, EtherCAT, PROFINET, DeviceNet, PROFIBUS) Conveyor synchronization function	
Safety standard	Refer to Table.1	
Combinable SCARA Robots	THE400-E,THE600-E (THE800-E,THE1000-E Scheduled to be supported)	

4 Effects

Currently, the conventional THL series of SCARA robots has completed a lineup of various arm lengths (300 mm to 1200 mm) in combination with the TSL3000 series, but the THE-E series, which is compatible in combination with the TS5000-EMS, was launched first with two models of 400 mm and 600 mm (THE400-E and THE600-E), which are in demand in the market.

The appearance of THE400-E and THE600-E is shown in Fig. 3.



Fig. 3 appearance of THE400-E and THE600-E

The major advantage of having obtained certification of conformity to safety standards from Notified Body is that Slers can immediately make a decision on whether to accept or reject our robots, since they can see all the conformity standards of our robots on the TÜV website. We will continue to develop products which meet market requirements by increasing the number of models that are compliant with these standards so that we can respond to the diversifying global market with a sense of speed.

5 Conclusion

We will expand and develop the upper arm length lineup of THE-E series to meet the diverse needs of users.

With the recent emergence of the collaborative robot, customer needs regarding industrial robots are becoming more demanding for safety. We will strive to maximize customer satisfaction by utilizing the knowledge we have gained through this safety standard conformity certification process.

Shibaura Machine NC System Development History



Jun FUJITA

Senior Expert,
Research &
Development Center



Masakazu KANEMOTO

Former engineer
of Shibaura Machine Co., Ltd.

1 Introduction

Shibaura Machine (formerly Toshiba Machine) is one of the few machine tool manufacturers in Japan which develops and produces their own numerical control (NC) systems. The reasons for this are as follows:

- Our business originated in the machine factory of Toshiba Corporation's heavy electric machinery division and we have had close ties with Toshiba Corporation since our establishment which has enabled us to maintain close cooperation in the field of electronics.
- In 1977, when the NC business was transferred from Toshiba Corporation, engineers engaged in NC system development, design, production, and quality inspection at the Toshiba Corporation Fuchu Plant stayed at our Numazu Plant for about two years, giving us an opportunity to inherit the NC technology.
- In 1975, we entered into a technical agreement for machining centers with Kearney & Trecker in the U.S. and, as a result, accumulated utilization technology related to NC-based machine tools.
- We have an affiliate company, Toei Electric Co., Ltd., which specializes in the manufacture of electrical control devices and their electronics production line supports the production of NC systems.
- In addition to the above we made other technological developments which preceded NC systems at the time, such as the development of the POSITION MASTER hardware NC device using Magnescale in 1973.
- The commercial availability of high-performance microcomputers has dramatically improved software control technology.

- Our Control Department also worked on a prototype CNC system using DEC LSI 11 12-bit microcomputer based on a grant from MITI and the basic technical foundation for software to control machine tools in real time had been established.

Many people have been involved in the development of our NC systems. Below is the history of our NC system development, including introductions to the people involved.

2 Transfer of NC business from Toshiba Corporation

The history of our company described herein begins with the transfer of the NC business from Toshiba Corporation in 1977, which contributed greatly to the establishment of the foundation of our NC business.

2.1 Toshiba Corporation's NC business before transfer

Toshiba Corporation produced the following NC systems at their Fuchu Plant before the transfer. TOSNUC^{®(1)}XXX is hereafter described as T-XXX.

1) T-420M

NC system using Toshiba Corporation's TOSBAC40 series 16-bit minicomputer;

2) T-420P

NC system using TOSBAC40 series for punch press manufacturers;

3) T-300M, L

NC system using Toshiba Corporation's 12-bit microcomputer for machining centers and lathes;

Our machining center used the T-300MX at that time.

Among the above NC systems, the manufacturing and testing facilities for T-420M, 420P, and 300M were transferred to our company and our engineers were trained on the details.

A primary reason for the business transfer was Toshiba Corporation's conviction machine tool manufacturers can respond more quickly to customer needs by manufacturing NC systems themselves. Further, the transfer of the NC business to us was appropriate due to our experience using the T-300MX.

2.2 Transfer of NC systems under new development

At the time, the Fuchu Plant was developing a high-performance CNC system using AMD's bit-slice CPU under the supervision of Chief Engineer Mr. Matsumoto.

The bit-slice CPU was used because it was intended to perform complex AC servo calculations at high speed using a microprogram.

This new NC system was intended to be very ambitious using a PDP display, which was still rare at the time, as the display unit and also enabling servo and induction motor control.

Mr. Matsumoto, the Chief Engineer who had been involved in this development, and other project members came to our Numazu Plant as an advance team and started development. Three months later, the people involved in the design and production of NC systems up to that time came to the Numazu Plant and began the transfer of the NC business.

Development members: Mr. Matsumoto, Chief Engineer (Hardware) Mr. Shimada, Mr. Otsuka, Mr. Nagayama

Project transfer members:

(Software design related) Mr. Nakata (300), Mr. Kumagai, Mr. Kikuchi (420)

(Hardware design related) Mr. Nomura, Mr. Hakata, Mr. Meguro

(Hardware and testing) Mr. Fukami, Mr. Horiba, Mr. Ezawa,

Mr. Naraoka, Mr. Ogasawara, Mr. Shidara

(Manufacturing) Mr. Ohki

Mr. Matsumoto, who supervised the development team, had led the development of Toshiba Corporation's NC systems and had a deep knowledge of servo control. We were deeply impressed by his attitude toward development. He was also deeply trusted by the employees transferred from Toshiba Corporation.



Fig. 1 First shipment of T-300 (courtesy of Mr. Goto)

In 1977, in addition to the existing Control Engineering Department 1 which handled electrical control in the division, the Control Department 2 was established to strengthen in-house NC system production, and under the leadership of General Manager Iimura, development, design, testing, and service were strengthened in terms of personnel. The transferred software was taken over by Mr. Adachi for T-420M, Mr. Ozaki for T-300, and Mr. Oashi for T-300PG at our company.

Test equipment for individual boards using jigs, equipment for NC system shipment inspections including thermostatic chambers for continuous temperature testing of the NC system main body before shipment, shipment management systems which keep the result records of shipment tests, etc., were installed in the newly established Electronic Equipment Section at eight plants, where many new members began working.

Fig. 1 shows a photo of the first shipment of the T-300 from the Electronic Equipment Section on April 24, 1978.

Today, the NC shipping-related systems have been transferred to Toei Electric Co., Ltd.

3 Development of T-500MX

We developed the T-500MX for our machining center based on hardware developed by members of Toshiba Corporation. The leader of the development was Mr. Morimoto, and the software was based on a simple multi-tasking real-time OS prototyped by LSI 11 and developed by our company. From this point on the Control Systems Division developed NC systems in two sections: the Control Design Section, which developed the product line centered on the T-500MX, and the Control Development Section 2, which developed

the next-generation NC systems.

Subsequently we have developed various models of TOSNUC®. Fig. 2 shows the chronological transition of the models.

3.1 | Development of T-500MX product line

There were various requests for machining centers from customers and Mr. Yoshida, the Section Chief of the Manufacturing Department, incorporated them all into the NC system.

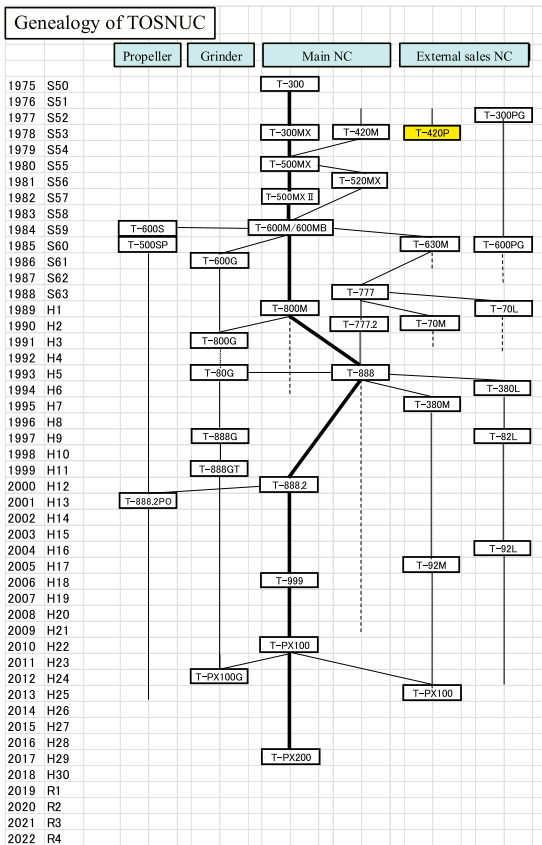


Fig. 2 Transition of TOSNUC® models (courtesy of Mr. Tsuchiya)

One of them is the multi-pallet system in which the machining program corresponding to the pallet code number attached to the pallet is set on the NC screen in advance, and machining continues until all workpieces set on the pallet have been machined to completion. This system allows continuous unmanned machining of workpieces even at night and has been adopted by many users. By using the workpiece setup function it is also possible to change pallets without stopping the machining process.

The T-500MX was able to incorporate these functions relatively easily because the NC, rather than a PLC, directly controlled the sequence. This is an example of a system taking advantage of the machine manufacturer's NC system which enables control through integration of the NC operation screen and the machine's setting

screen.

Additionally, we developed an automatic measuring system which automatically measures hole diameters and workpiece machining surfaces using a touch sensor probe, a tool wear and breakage detection system based on detection of spindle motor load current, and an FMS system which communicates with a higher-order computer to download machining programs, report machining completion, give cycle-start instructions, and exchange various other information.

However, machine sequencing with NC lacked flexibility for application to various machine tools, including large machines, and the size of NC machining programs for die/mold machining was becoming larger and larger, making it necessary to significantly increase memory capacity.

The servo used was a DC servo with a resolver as the position detector and a tachogenerator for speed detection. The velocity control was performed by analog processing from analog velocity commands and analog velocity feedback using an operational amplifier circuit. Therefore, the servo rigidity could be relatively high, but there were error factors such as gain error, zero-point offset, and drift in the analog system.

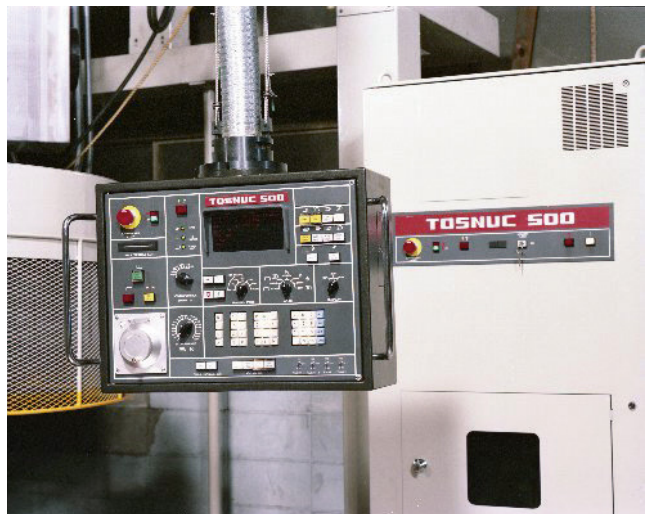


Fig. 3 Operating pendant and main unit of T-500

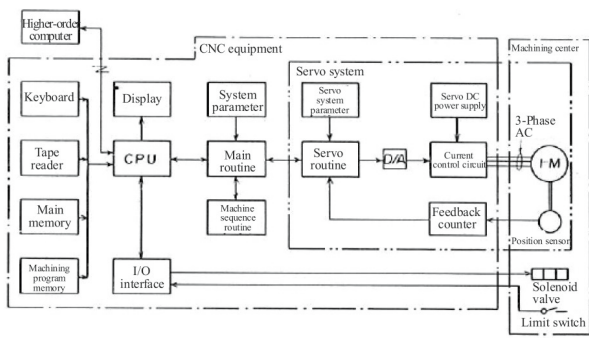


Fig. 4 T-520 block diagram

4 T-520 series (1982)

As can be seen from the block diagram in Fig. 4, the T-520 used a single CPU to perform all processing from I/O interface, display, machine sequence, and servo control, in addition to the NC main routine.

The CRT screen was adopted, the servo was changed to an AC servo using an induction motor, and the speed control was changed from analog hardware control to digital software control. The position detector employed a pulse generator and the velocity was obtained by differential calculation of position feedback. Therefore, errors in the speed control system caused by analog processing were eliminated and control repeatability was improved.

Spindle motor control was also performed with the same hardware as the feed axis but using a different software control method.

The T-520 was mainly used for machining centers such as VMC-6C.

5 T-600 (1984)

The T-600 was a system which formed the basic structure of the subsequent TOSNUC® series. Fig. 5 shows the system configuration of the T-600. The system was configured with multiple CPUs and common RAMs through bus connection and was expandable according to the scale of the system including options, number of axes, and so on. The system employed a menu system with function keys as the operating method.

The T-600 was equipped with a PLC so machine operation was controlled by sequence programs. This allowed the machine division engineer to incorporate machine operation into the system and perform debugging by him/herself, in contrast to earlier NC systems which included machine operation control and thus required changes to the NC software when changes were made to the machine operation.

Further, the additional function of macro-programming allowed the machine division engineer to more flexibly incorporate machine operation.

While paper tapes were previously used for input/output of programs, parameters, etc., this series employed magnetic bubble memory cassettes. This eliminated the need for paper tape readers and punchers which were large and troublesome to handle.

The AC induction motor used in the T-520 had a simple and robust structure, but its current control computation was complex and had difficulty with dynamic braking. Therefore, we developed an AC servo system with a permanent magnet synchronous motor with effective dynamic braking and less current control computation load. The number of axes which could be controlled by a single servo control CPU board was four, and the control of up to twelve axes by three boards was possible.

This system employed Zilog Z8000 series as the CPU. It had just been developed and the formal manuals for the peripheral chips were not yet available, so our development relied on handwritten English copies.

Assembler language was used in the development. To shorten the servo processing time, the number of processing cycles for each instruction words was written as a comment on the right side of the list to minimize execution time.

The position detector employed was an absolute position detector consisting of three resolvers combined via gears. Unfortunately, the effect of resolver phase error appeared on the machined surface, so the sensor used for position control was changed to a pulse encoder and the resolver was used for absolute position detection.

As a control function for high-speed, high-precision machining, we developed a preview control which applied modern control theory which could suppress path errors caused by servo delays to 1/7th of the conventional level.

We developed a sequence axis function which controlled servo motors with a sequence program, allowing servo axes to be used for controlling magazines, AAC, etc.

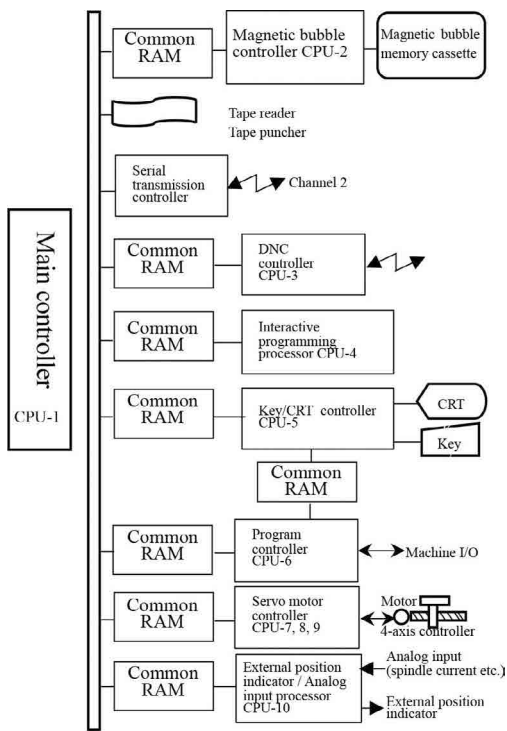


Fig. 5 T-600 system configuration

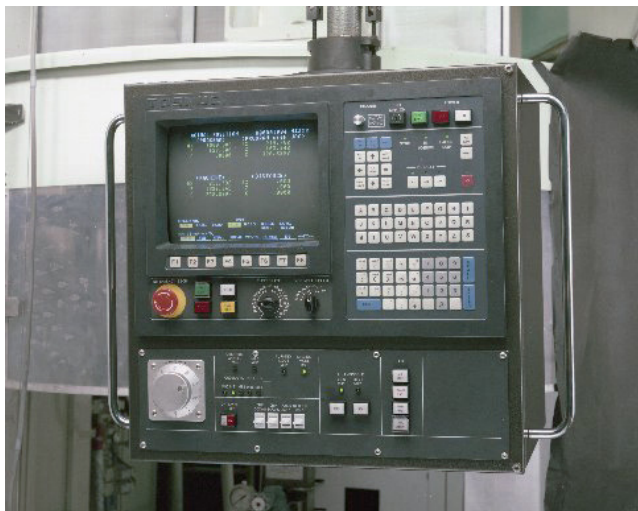


Fig. 6 Operating pendant of T-600

6 T-777 (1987)

The T-777 was the result of close cooperation between the Machine Tool Division and the Control System Division in which the Machine Tool Sales Engineering Section compiled the NC operation specifications best suited for horizontal boring machines and the Control Design Section conducted the development. Features of this system included pop-up menus, help functions, interactive programming, and the use of joysticks for manual operation pendants.

One of the difficulties encountered during development was the HMI developers often had to make corrections when operating the

software on the actual machine, even though it was built according to the prepared specifications, because it was impossible to know how good or bad the HMI really was until it was actually operated.

As a result of these efforts, the operability was dramatically improved and the product became a hit in the market, earning a good reputation.



Fig. 7 T-777 on BTD

7 T-800 (1989)

The T-800 was a product which aimed for high speed, high precision, and high performance by using Motorola 32-bit CPU, MC68020 and a VME bus. We developed a multi-window HMI system with reference to UNIX[®] workstation by using a high-speed processor dedicated to display. However, because flexibly overlaid displays were inconvenient on NC screens which could not be used with a mouse, fixed-position multi-window displays were employed.

As the standard I/O device, a 3.5" floppy disk was used, which made it easier to handle processing programs and parameters.

To achieve a higher-performance servo control system, an absolute encoder with a position detector having a resolution of 160,000 (pulses/rev), the highest at the time, was adopted. This attained standard position control resolution of 0.1 (μm).

In addition, the control cycles attained were at the highest level at that time; position control cycle of 3 (ms) and speed control cycle of 0.5 (ms).

Although assembly language was generally used for development at that time, we adopted C language for the background part of the servo control unit and the HMI part. In addition, for task management of the servo background section, we created our own serial multitasking OS which switches tasks by wait(). This OS was also used in the main control unit and servo control unit of our subsequent controllers such as INJECTVISOR[®](*) and TOSCAST[®](*).

Our development also included an RS232C terminal function and servo graph display for testing functions.

We developed the CNC SHAPE[®](*) function for high-speed, high-precision, high-quality die/mold machining, which is described below.

8 Challenge in die/mold machining

One of the most advanced and difficult-to-realize functions of CNC systems is high-speed, high-precision, high-quality die/mold machining. In the late 1980s, a die/mold machining center named MPD with T-600 was delivered to an automobile manufacturer.

However, the T-600 was an ordinary NC system and did not have the functions of multiple program block prefetching and inter-block acceleration/deceleration, which were common in die/mold machining tools. Therefore, when a short line segment machining program was executed with a 6000 (mm/min) command, a continuous round-shape bite with a bead pattern occurred on the machined surface.

For the T-600, we were able to prevent the bite by implementing symptomatic software countermeasures, but we could not make a modification to increase the number of prefetching blocks. Since the shape could not be recognized, it was difficult to both suppress vibration, which degrades the machined surface, and suppress radius reduction errors, which occur on curved surfaces.

We eventually developed a pre-processor which operated on a PC. It read the customer's program, recognized the shape and output a program with the appropriate speed and acceleration/deceleration for the shape.

This experience made us keenly aware of the need to develop NC functions which could handle die/mold machining so we developed the CNC SHAPE[®] (shape recognition predictive control) function with the T-800 having enhanced processing performance.

The CNC SHAPE[®] function was realized with an optional board. This function buffers the amount of travel per sampling cycle

distributed by the NC according to the machining program and uses this data to recognize the shape. By redistributing the data with the target speed and acceleration/deceleration pattern calculated according to the recognized shape, smooth movement at optimum speed which maintains the specified accuracy could be achieved. Because many numerical operations had to be performed in a short time, Analog Devices ADSP21000 DSP, which was the fastest computing element available at the time, was used.

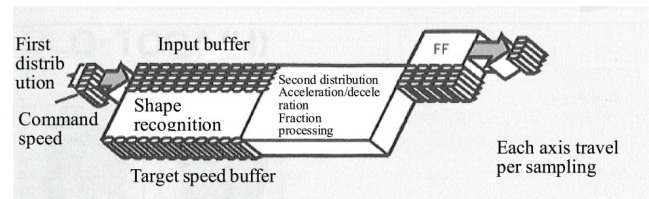


Fig. 8 CNC SHAPE basic configuration

In the first inquiry, the block length in the customer's machining program was about 10 (mm) and they wanted a function to smooth out the machined surface, which was polyhedral, when no countermeasure was taken. In response to this we developed a smoothing function which performs a spline interpolation up to the third order through a commanded point.

The main functions added since then were:

- (1) averaging function as a countermeasure against the disturbance of machined surfaces due to triangular patches in CAM data preparation;
- (2) fluent control to reduce the influence of random disturbances in CAM data;
- (3) NURBS interpolation to deal with NURBS programs;
- (4) SF control to change the spindle speed and feed rate according to the machining point of the ball end mill to suppress tool wear and improve machining efficiency;
- (5) area machining in which the Z-directional offset, S, and F could be varied by specifying an area on the workpiece;
- (6) broadband vibration suppression function to suppress vibration associated with the natural vibration of the machine feed drive mechanism over a wide frequency range; and,
- (7) ShapeAssist to improve machining speed by suppressing path errors caused by acceleration/deceleration after interpolation.

9 T-888 (1994)

The T-888 was developed to combine the best features of the T-777, which focused on operability, and the T-800, which focused

on performance, while covering everything from low-end to high-performance models.

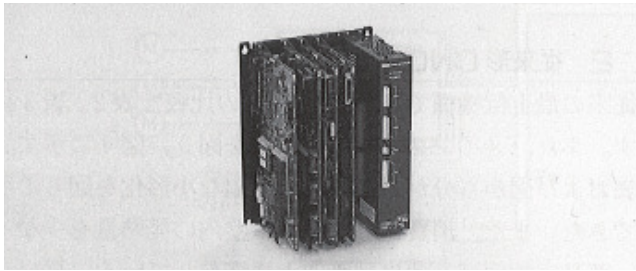


Fig. 9 Main unit of T-888

In terms of hardware, the main unit featured a footprint downsized to 1/5th and a display unit changed from the existing CRT to a 10-inch plasma display (or an optional 10-inch color TFT LCD display) to make the pendant lighter and thinner.

In addition, the bus connection to our general-purpose PLC, the TC200, allowed the system to have a wealth of I/O functions and enabled editing of ladder programs and monitoring of their execution status from the CNC's operation panel.

The processing power of the main CPU was increased to more than twice that of the T-800, enhancing software processing capability. This increased the processing capacity of the CNC SHAPE[®] function which performed high-speed, high-precision, and high-quality die/mold machining.

The servo system employed a high-resolution serial absolute encoder with a resolution of $2^{20}=1,048,576$ (counts/rev).

An example of other developed functions was the UIT (user interface tool). This function changes the form of a UIT program file containing processing procedures such as key processing, screen display, and data input/output on the NC, created on a general-purpose PC using the UIT language, to an executable one which loaded into the NC. This allowed machine-specific NC functions to be created by the machine division engineer.

The T-888 had the orbit boring function developed jointly by the Research Laboratory and the Machine Tool Division. This function allowed the machining center to perform continuous variable radius boring by synchronizing the spindle rotation position and XY-axis circular interpolation motion with a turning tool mounted on the spindle. This function was patented and licensed to other companies in the industry.

The T-888 currently holds the record for the largest number of units produced among our CNC systems.



Fig. 10 Pendant of T-888

10 T-888.2 (2000)

The T-888.2 employed a RISC CPU which was faster and could perform double-precision floating-point operations at a greater speed than the CISC CPUs used in the past. The overall programming language used for the development was unified to C language.

There was a trend in the world to use high-speed serial communication to connect digital amplifiers to facilitate distributed placement of amplifiers and expansion of the number of axes. In line with this trend we developed the T-888.2, a system which connected the T-888 controller and amplifiers via high-speed serial communication, beginning with position commands.

Each amplifier was equipped with a CPU to realize digital control of position, speed, and current. The T-888.2 was the first system in our company to provide software and digital control of even current control.

The position control cycle was 0.5 (ms) and the speed control cycle was 0.25 (ms).

11 T-999 (2006)

We developed a software digital control amplifier for T-888.2, but this method proved to be limited in its ability to achieve even higher performance. Therefore, we decided to develop the world's best current amplifier combining the advantages of digital control with the ease of handling of an analog amplifier.

To improve control performance it was necessary to minimize dead time, but with software sampling control, dead time could not be reduced lower than a few tens (μ s). Therefore, we developed a custom LSI which controlled dead time from the acquisition of current feedback to the output of a voltage command in less than 3 (μ s) by using hardware digital control to receive the current command and electric angle from the speed control section of the controller, and predicting the electric angle at the time of reading the current feedback and outputting the voltage command on the amplifier side (C-engine, shown in Fig. 11). The interface between the speed control section and the current control section employed a high-speed, asynchronous serial communication, achieving easy handling similar to an analog amplifier with the high performance of digital control.



Fig. 11 Developed current control LSI C-engine

This dramatically improved the current control performance and greatly reduced the number of failures of servo amplifiers for machine tools.

12 T-PX100 (2010)

As networking of factories progressed and high-speed data exchange via Ethernet[®] between PCs became commonplace, there was a growing demand for high-speed data communication for CNC systems, such as input/output of machining programs. To cope with a world where PCs were already used as a matter of course we decided to adopt a PC for the HMI and developed a CNC system equipped with a Windows[®] operating system. The HMI was developed using the C# language. Also, the OS of the main control unit adopted the commercially available T-kernel to easily support general-purpose I/O such as USB, etc.

Fig. 12 shows the operation pendant. The display screen used was a 15-inch LCD.

13 T-PX200 (2017)

With the spread of smartphones, smart CNC systems with touch screen panels used for the HMI were released from various competitors. To follow this trend, we developed a CNC system with a 19-inch touch screen panel (Fig. 13).

New integrated screens, instruction manual viewer, etc., were added and, even on conventional screens, the function keys now can be directly touch-operated, which considerably improves operability.

Real-time 3D interference check functionality is realized by interfacing with a PC equipped with CGTech CAS using high-speed Ethernet[®] communication.



Fig. 12 Operation pendant of T-PX100



Fig. 13 Operation pendant of T-PX200

14 Conclusion

The above is a brief history of the development of our CNC systems along with the transition of major milling machine models. We have evolved our CNC systems by incorporating elements available at the time to improve functionality and performance, aiming to contribute to the competitiveness of our machine tools through improved operability, dynamic performance, and cost performance.

Furthermore, elements developed for our CNC systems have been applied to the injection molding machine controller INJECTVISOR®, die-casting controller TOSCAST®, extruder controller EXTVISOR®^(*), and robot controllers. These common elements include not only hardware elements but also software elements such as the HMI operating system, multi-window system, main controller operating system, servo operating system, test terminals, graphic displays, and transfer function measurement function.

In the past, software for built-in controllers was mostly developed independently, but in recent years, with the spread of PCs, the development of networks, peripherals with general-purpose interfaces, and production management tools, it has become

important to efficiently develop functions using platforms with high affinity.

In addition, basic performance, such as CPU processing speed, detector resolution, and control cycle, have become almost the same for all competitors, and no longer serves as a differentiating factor.

In light of this situation it is necessary to carefully consider what we should do with our CNC systems in the future.

*1) "TOSNUC", "INJECTVISOR", "TOSCAST", "CNC SHAPE", and "EXTVISOR" are registered trademarks of Shibaura Machine Co., Ltd.

*2) "UNIX" is a registered trademark of The Open Group in the United States and other countries.

*3) "Ethernet" is a registered trademark of FUJIFILM Business Innovation Corp.

*4) "Windows" is a registered trademark of Microsoft Corporation in the United States and other countries.

Introduction to Patents

One of our company policies is to "respect intellectual property rights". We protect the results of technological development with intellectual property rights and respect the intellectual property rights of third parties. We are focusing on technological development to provide products, systems, and services which satisfy our customers. As a result, we hold approximately 1,700 patents in Japan and overseas. We will herewith introduce patents mainly related to energy and the environment. These patents are highly rated by Patent Score of Patent Result Co., Ltd.

(Patent Score: An index which scores and evaluates the degree of attention attracted by individual patents based on examination progress information)

1 Tool and Machine Tool

Patent number: Japanese Patent No. 5,548,530

Inventors:

Koichi KATO, Makoto SAWAZAKI, Haruhito SUGIYAMA, Yasufumi KAWAGO, Shuhei HOSOYA, Masahiko IIDA, and Yasunori KATO

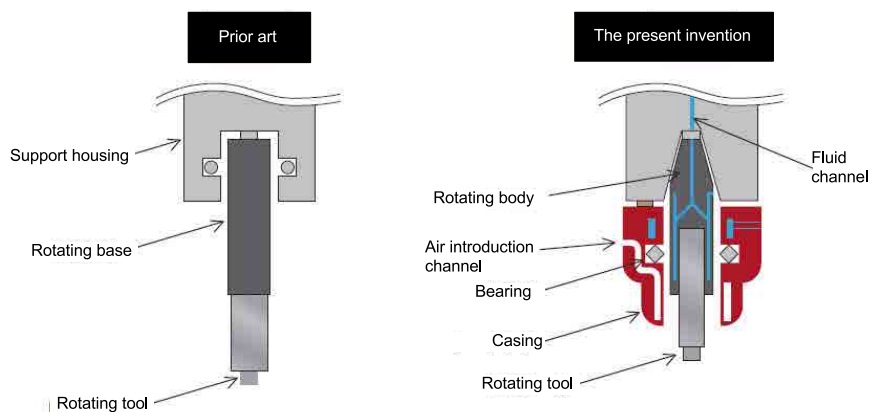
Currently, the manufacturing industry is developing various technologies with the aim of achieving the SDGs and realizing a decarbonized society. Technological developments which contribute to energy saving and productivity improvement are being carried out for machine tools.

The holder of conventional machine tools is provided with a rotating base, a support housing, and a bearing between them. The holder projects the tip of the rotating tool to which a high load is applied. For this reason, when a high load is applied to the rotating tool and the holder, at the joint between the rotating tool and the rotating base, a load concentration and resulting thermal deformation may be generated causing the joint to come loose. Therefore, there is a demand for a design which reduces the effects of a high load.

The tool of this patent has a rotating body and a casing, and between them is a bearing which can receive a load in the thrust and radial directions. Therefore, even when a thrust load is applied to the tool and the spindle, such as when the tool is pressed against

a workpiece during machining, the load can be relieved from the bearing and diverted to the frame. In addition, even if a radial load is applied to the tool, such as when the tool is moved in a direction which intersects the rotation axis, the load can be relieved from the bearing and diverted to the frame. As a result, the high load is not directly applied to the tools, the spindle, and the joint, making it possible to reduce the effect of the load.

Furthermore, the tool of this patent has a fluid channel (light blue in the figure) and an air introduction channel (white in the figure) in the rotating body and casing. Fluid cooling suppresses the transfer of frictional heat generated by the rotating tool to the tool bearing during workpiece machining, thereby reducing the load on the joint and spindle. In addition, the air introduction channel makes it possible to maintain an appropriate temperature so the tool is not cooled too much. As a result, tool performance can be maintained for a long period of time and machining efficiency can be improved, making it possible to contribute to improved productivity.



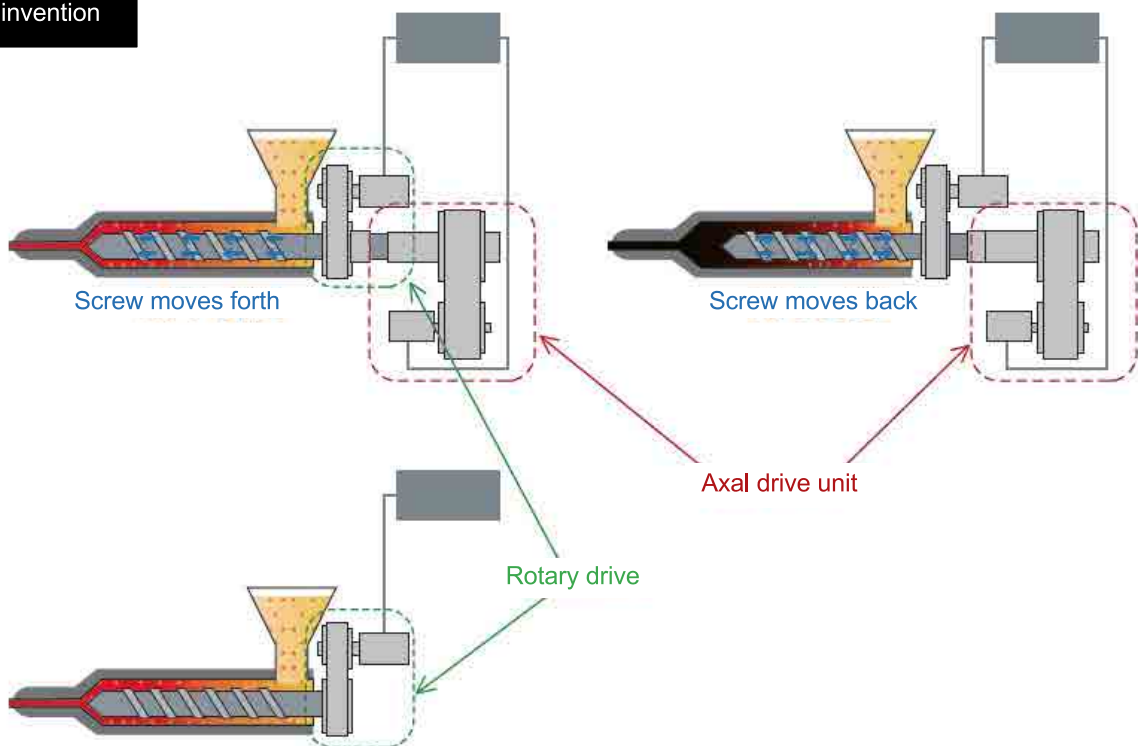
Patent number: Japanese Patent No. 6,186,243
 Inventor: Harumichi TOKUYAMA

Currently, the manufacturing industry is developing various technologies with the aim of achieving the SDGs and realizing a decarbonized society. Technological developments which contribute to energy saving and productivity improvement are being carried out for injection molding machines and other molding machines.

An injection unit is composed of a barrel which holds a material inside, a screw which is placed inside the barrel, and a rotary drive which rotates the screw. During operation, insufficient heating and insufficient melting cause material to adhere to the barrel and screw, increasing the resistance to screw rotation. This results in a decrease in weighing accuracy of the material in the molding process resulting in variations in product quality.

The injection unit of this patent is newly provided with an axial drive unit which moves the screw in the axial direction and applies a shearing force to the inside of the barrel allowing elimination of the adhesion state of the material. When the resistance force which the screw receives from the material exceeds a predetermined value, the screw stops rotating and starts to move back and forth to generate shearing force in the axial direction. As a result, it becomes possible to eliminate the adhesion state of the material, maintain weighing accuracy, and reduce variations in product quality, contributing to improved productivity.

The present invention



Prior art

3 Barrel block for twin-screw extruder

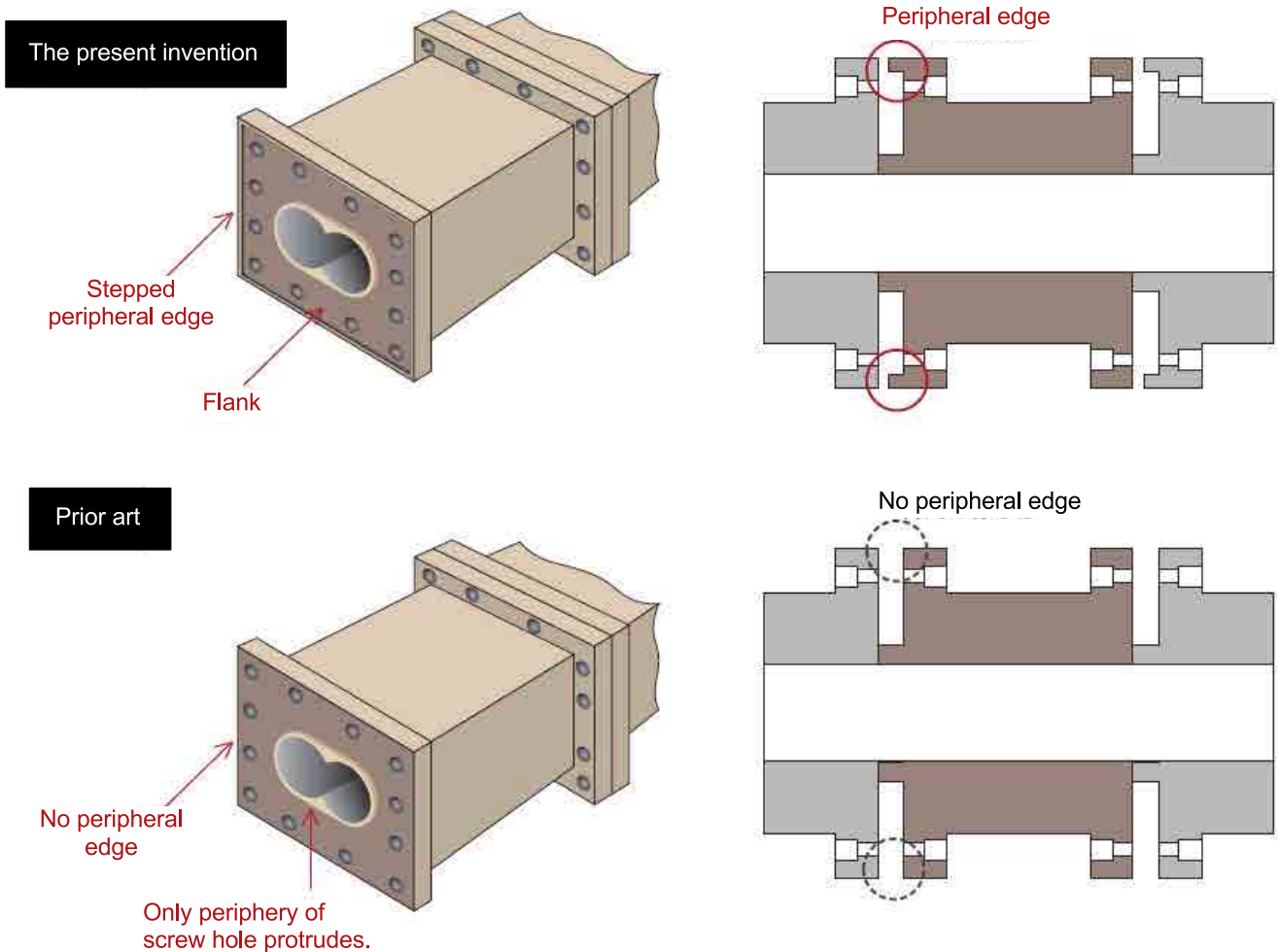
Patent number: Japanese Patent No. 6,348,216
Inventor: Masanobu OISHI

Currently, the manufacturing industry is developing various technologies with the aim of achieving the SDGs and realizing a decarbonized society. Technological developments which contribute to working environment improvement and productivity improvement are being carried out for extruders.

A barrel block installed in a conventional extruder has a shape featuring the joint surface of the block with the protruded periphery of a screw hole. When the barrel blocks are joined to each other, the peripheries of the screw holes are in close contact with each other, preventing leakage of raw material from the joint portion. However, if the tightening bolts during joining are tightened differently from one another, an uneven contact occurs in the periphery of the screw

hole, making it impossible to maintain a uniform contact state. Therefore, raw material leaks through a gap, leading to deterioration of the working environment.

The barrel block of this patent has a stepped edge on the outer periphery of the joint portion on one side. When barrel blocks are joined together with tightening bolts, this outer peripheral edge makes it possible to maintain a uniform contact state in the periphery of the screw holes while limiting the amount of tilting of the joint portion. This can suppress raw material leakage from the gap between the barrel blocks, leading to an improved working environment.



4 Hybrid core drive and molding machine

Patent number: Japanese Patent No. 6,970,730

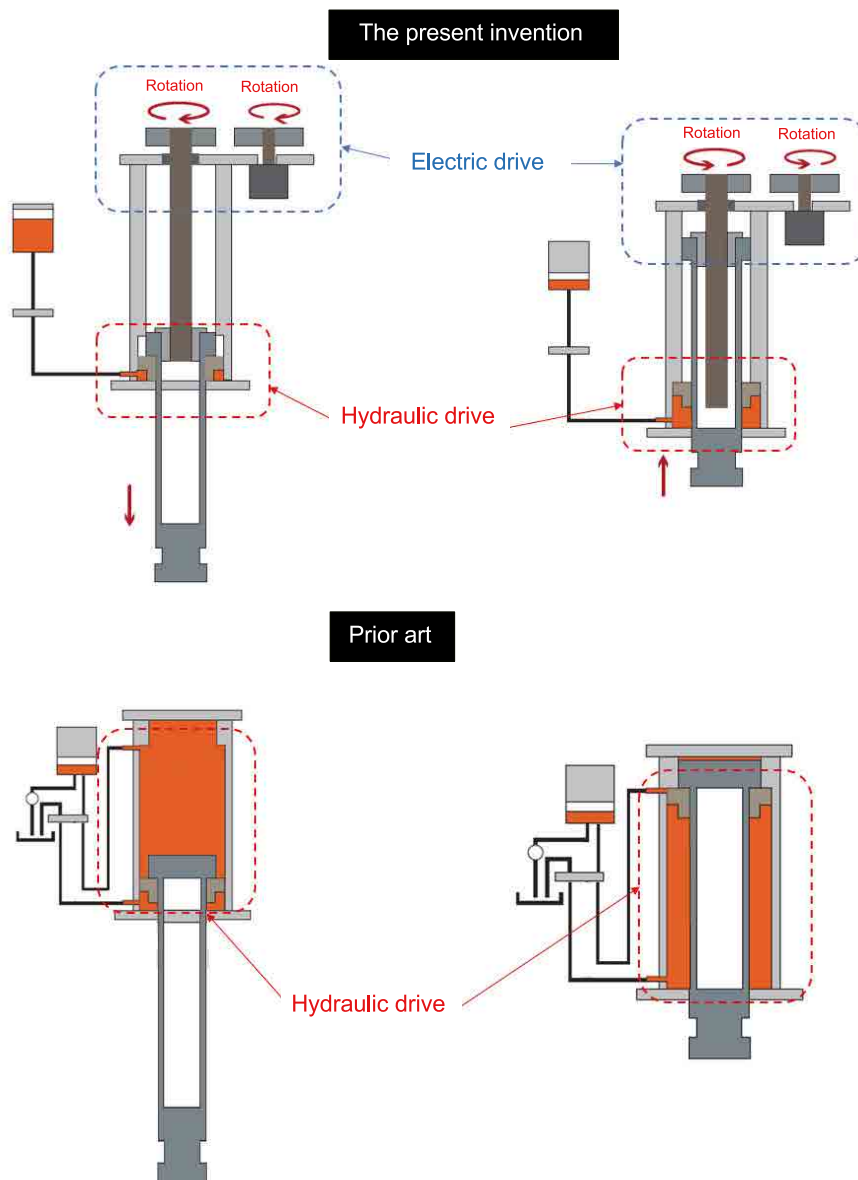
Inventors: Mitsutoshi NAITO, Makoto TSUJI, and Saburo NODA

Currently, the manufacturing industry is developing various technologies with the aim of achieving the SDGs and realizing a decarbonized society. Molding machines such as die casting machines and injection molding machines pour melted materials into molds to manufacture products. Therefore, machine manufacturers need to develop technologies which are related to molds and materials in addition to molding machines.

Conventionally, a hydraulic core cylinder installed in a mold has a large amount of hydraulic oil, potentially causing deterioration of the working environment due to oil contamination. In addition, the clamping unit and core drive of the molding machine share a hydraulic circuit, which can cause failure to simultaneously open and

close the mold when moving the core back and forth. This results in difficulty shortening the cycle time of the molding machine which does not contribute to improved productivity and energy saving.

The device of this patent is a hybrid cylinder device composed of a hydraulic drive operated by a small amount of hydraulic oil and an electric drive operated by a rotary motor. This device not only improves the working environment by reducing the amount of hydraulic oil, but also permits simultaneous opening and closing of the mold when moving the core back and forth by not sharing the hydraulic circuit. Thus, the present invention can shorten the cycle time of the molding machine which contributes to improved productivity and energy saving.





Hidetoshi YOKOI

Emeritus Professor
University of Tokyo

My relationship with Shibaura Machine started as far back as 33 years ago (including the years of Toshiba Machine). At that time, I had just taken up a post at the Institute of Industrial Science, The University of Tokyo. At the newly established laboratory, I chose injection molding as my field of study in which there were only a few researchers, and I started up a project, "Injection molding phenomena visualization experiment and analysis" (commonly called "V project"), to systematically elucidate the molding phenomena by visualizing the inside of the mold and heating cylinder using a unique technology.

Toshiba Machine has been a consistent participant in the; V project which lasted for 10 years, the "Injection molding to pursue 'Cho (ultra)' project (commonly called "U project") for 23 years, and the current "Future-oriented injection molding technology" of Social Cooperation Programs during the last 5 years. I understand the visualization technology was used for Toshiba Machine's development of a large-diameter visualization cylinder, and it must have greatly contributed to the elucidation of the plasticizing process and molding phenomena with various types of screws.

Toshiba Machine has been playing a core role in manufacturing in Japan and has continuously provided fundamental manufacturing technologies and production machines to this day, while flexibly responding to changes in society and the expanding the new sphere of industry as part of its business plan. The origin of its business was the manufacturing of large machine tools which supported the post-war manufacturing industry in Japan. The same DNA has been handed down to the company of today as it places its business focus on; injection molding machines and extrusion machines for plastics, die casting machines for melted metals processing, large machine tools, high-precision machines

for optical parts, etc., which support the precision mold industry in removal processing, robotic technology, fundamental control technology which promotes the systemization of the whole factory and the unmanned factory, and in almost all fields of manufacturing except presses. Furthermore, the company recently launched its new business in additive processing such as AM and additive manufacturing.

To continue to produce high value-added processing machinery with advanced functions, it is necessary to achieve a step-by-step high level of improvements in the individual elemental technologies. Part of those efforts were introduced in the 27 volumes of the Toshiba Machine Engineering Review. In addition to the innovation of these individual elemental technologies, "Shibaura Machine", as a newly established company, promotes the digitalization of the whole process from design to manufacture and sales, with DX based on digital twin. The promotion of DX is a new worldwide trend to innovate the fundamental manufacturing process. I expect the leader of manufacturing, "Shibaura Machine", to become the flag bearer of DX, playing a leadership role in the industry.

Shibaura Machine Engineering Review vol.2 (this issue), featuring the theme of "Energy and Environment", discloses the results of efforts in line with the medium- to long-term plan of "Shibaura Machine", including energy saving of die casting machines, energy saving through die sinking of cemented carbide, elemental technologies for fast spindle development, advancements of foam molding aimed at reducing environmental load, reduction of environmental load by using CAE in SCARA robot development, and DX initiatives for twin-screw extruders.

In addition to the measures to respond to the trends of

digitalization, IoT and DX, the company's activities in relation to corporate governance code and sustainability are introduced. Shibaura Machine is expected to promote new technological innovation and develop new elemental technologies in order to meet the new objectives it should bear, including energy saving, regulation of greenhouse gas emissions, and SDGs. We can find in this issue Shibaura Machine's fresh vitality and determination in its messages to society and the industry.

I understand the most important thing in processing technology is to accurately understand the processing phenomena. High-precision analysis with CAE will only be possible after the machining process is accurately modeled. Likewise, IoT technology will only be useful when it is associated with the phenomenon. It is also the same with digital twin for DX. Multilateral measurements and the visualization technology for the machining process are the essential elemental technologies to model phenomena. For this reason, I highly evaluate the disclosure of those results in this issue as fundamental to manufacturing. I expect "Shibaura Machine", as a newly established company, will make step-by-step efforts to continue improvements of elemental technologies and development of new processing technologies based on the accurate understanding of physical phenomena while leading DX, IoT, and SDGs as a flag bearer.

Publish : March 31, 2023
Not for sale : All Rights Reserved Reproduction or quotation without permission is prohibited.
Publisher : Mitsunori KOKUBO
Press : SHIBAURA MACHINE CO.,LTD.
Research & Development Center
R&D Department
4-29-1,Hibarigaoka,Zama-shi,
Kanagawa-ken,252-0003,Japan

Shibaura Machine Engineering Review Editonal Commission

Chairman	Mitsunori KOKUBO		
Members	Jun FUJITA	Toshihiro IGARASHI	
	Tatsuhiko MARU	Daisuke FUJIMAKI	Shigeyuki FUJII
	Takato BABA	Kazuhiro SEKI	Hiroyuki OCHIAI
	Takuro KAZAMA	Masahiko NAGATA	Katsuhisa TAKEDA
	Yusuke ISHII	Daisuke YAMAGUCHI	
Coordinator	Kazuhito SATO	Masayuki YAMAMOTO	Takafumi OKAWA
	Hiroki AMEZAWA	Takayuki MATSUDA	Itaru SETO

Offices and Manufacturing Sites

Tokyo Headquarters

2-2, Uchisaiwaicho 2-chome, Chiyoda-ku,
Tokyo 100-8503, Japan
TEL: [81]-(0)3-3509-0200
FAX: [81]-(0)3-3509-0333

Numazu Headquarters

2068-3, Ooka, Numazu-shi, Shizuoka-ken
410-8510, Japan
TEL: [81]-(0)55-926-5141
FAX: [81]-(0)55-925-6501

Tohoku Branch

2-11-2, Yaotome, Izumi-ku, Sendai-shi,
Miyagi-ken 981-3112, Japan
TEL: [81]-(0)22-374-6111
FAX: [81]-(0)22-374-6118

Chubu Branch

5-307, Kamiyashiro, Meito-ku, Nagoya-shi,
Aichi-ken 465-0025, Japan
TEL: [81]-(0)52-702-7811
FAX: [81]-(0)52-702-1141

Kansai Branch

11F, Mainichi-Intecio Build., 3-4-5,
Umeda, Kita-ku, Osaka-shi, Osaka
530-0001, Japan
TEL: [81]-(0)6-6341-6181
FAX: [81]-(0)6-6345-2738

Kyusyu Branch

2-3-23, FMT Enokida Build.,
Hakata-ku, Fukuoka-shi,
Fukuoka-ken 812-0004, Japan
TEL: [81]-(0)92-451-2795
FAX: [81]-(0)92-474-1045

Numazu Plant

2068-3, Ooka, Numazu-shi, Shizuoka-ken
410-8510, Japan
TEL: [81]-(0)55-926-5141
FAX: [81]-(0)55-925-6501

Sagami Plant

4-29-1, Hibarigaoka, Zama-shi,
Kanagawa-ken 252-0003, Japan
TEL: [81]-(0)46-258-2801
FAX: [81]-(0)46-258-2900

Gotemba Plant

1-120, Komakado, Gotemba-shi,
Shizuoka-ken 412-0038, Japan
TEL: [81]-(0)550-87-3555
FAX: [81]-(0)550-87-3742

Domestic Group Companies

SHIBAURA MACHINE ENGINEERING CO., LTD.

267-2, Nishi-sawada, Numazu-shi,
Shizuoka-ken 410-0007, Japan
TEL: [81]-(0)55-921-7800
FAX: [81]-(0)55-921-7831
<https://www.shibaura-machine.co.jp/>
smeng

TOEI ELECTRIC CO., LTD.

131, Matsumoto, Mishima-shi,
Shizuoka-ken 411-8510, Japan
TEL: [81]-(0)55-977-4111
FAX: [81]-(0)55-977-4110
[http://www.toei-electric.co.jp/index_](http://www.toei-electric.co.jp/index_J.htm)
J.htm

SHIBAURA SEMTEK CO., LTD.

2068-3, Ooka, Numazu-shi, Shizuoka-ken
410-8510, Japan
TEL: [81]-(0)55-924-3450
FAX: [81]-(0)55-925-6556
<http://www.s-semtek.co.jp/>

SHIBAURA SANGYO CO., LTD.

2068-3, Ooka, Numazu-shi, Shizuoka-ken
410-8510, Japan
TEL: [81]-(0)55-922-0816
FAX: [81]-(0)55-924-5816

< East Asia >

SHANGHAI SHIBAURA MACHINE CO., LTD.

4788, Jin Du Road, Xinzhuang Industry Zone,
Shanghai, 201108, PEOPLE'S REPUBLIC OF
CHINA
TEL: [86]-(0)21-5442-0606
FAX: [86]-(0)21-5866-2450
SHANGHAI*, BEIJING, TIANJIN, DALIAN,
CHONGQING, NINGBO

SHIBAURA MACHINE (SHANGHAI) CO., LTD.

4788, Jin Du Road, Xinzhuang Industry Zone,
Shanghai, 201108, PEOPLE'S REPUBLIC OF
CHINA
TEL: [86]-(0)21-5442-5455
FAX: [86]-(0)21-5442-5466

SHIBAURA MACHINE (SHENZHEN) CO., LTD.

Room 608, Building 2, Animation Park,
Yuehai Road, Nanhai Street, Nanshan
District, Shenzhen, 518054, PEOPLE'S
REPUBLIC OF CHINA
TEL: [86]-(0)755-8625-0599
FAX: [86]-(0)755-8625-0522
SHENZHEN*, GUANGZHOU

SHIBAURA MACHINE TAIWAN CO., LTD.

7F., No.168, Ruiguang Road, Neihu District,
Taipei City, 11491, TAIWAN
TEL: [886]-(0)2-2659-6558
FAX: [886]-(0)2-2659-6381

< South East Asia >

SHIBAURA MACHINE SINGAPORE PTE. LTD.

123 Pioneer Road, Singapore 639596,
SINGAPORE
TEL: [65]-68611455
FAX: [65]-68612023
SINGAPORE*, KUALA LUMPUR, PENANG

SHIBAURA MACHINE (THAILAND) CO., LTD.

127/28 Panjathanee Tower, 23rd Floor,
Nonthree Road, Khwaeng Chong Nonthree,
Khet Yannawa, Bangkok 10120, THAILAND
TEL: [66]-(0)2-681-0158 ~ 61
FAX: [66]-(0)2-681-0162

PT. SHIBAURA MACHINE INDONESIA

Jalan Ciputat Raya No. 1B Unit 1&2,
Desa/Kelurahan Pondok Pinang, Kec.
Kebayoran Lama, Kota Adm. Jakarta Selatan,
Provinsi DKI Jakarta, 12310, INDONESIA
TEL: [62]-(0)21-22761766, 22761770
FAX: [62]-(0)21-2122761624

Major Sites outside Japan

* : HEAD OFFICE

SHIBAURA MACHINE VIETNAM COMPANY LIMITED.

2nd Floor, VIT Tower, No. 519, Kim Ma Street,
Ngoc Khanh Ward, Ba Dinh district, Hanoi,
VIETNAM
TEL: [84]-(0)24-2220-8700,1
FAX: [84]-(0)24-2220-8702
HANOI*, HO CHI MINH

SHIBAURA MACHINE INDIA PRIVATE LIMITED

No. 65 (P.O. Box No. 5), Chennai-Bangalore
Highway, Chembarambakkam, Poonamallee
Taluk, Thiruvallur, Chennai, TN 600123,
INDIA
TEL: [91]-(0)44-2681-2000
FAX: [91]-(0)44-2681-0303
CHENNAI*, DELHI, MUMBAI

SHIBAURA MACHINE MANUFACTURING (THAILAND) CO., LTD.

7/499 Moo 6, Tambol Mabyangporn, Amphur
Pluakdaeng, Rayong 21140, THAILAND
TEL: [66]-(0)38-027313
FAX: [66]-(0)38-027317

< The Americas >

SHIBAURA MACHINE COMPANY, AMERICA

755 Greenleaf Avenue, Elk Grove Village, IL
60007, U.S.A.
CHICAGO*, LOS ANGELES, CHARLOTTE,
ATLANTA, ONTARIO/CANADA
TEL: [1]-847-593-1616
FAX: [1]-847-593-0897

SHIBAURA MACHINE MEXICO, S.A. DE C.V.

Circuito Luxma No. 115, Poligono
Industrial, Milenio, C.P. 37290 Leon,
Guanajuato, MEXICO
TEL: [52]-477-101-8600

SHIBAURA MACHINE DO BRASIL COMERCIO DE MAQUINAS LTDA.

Rua Cubatao, 86 Conjunto 1307, Vila
Mariana, Sao Paulo, SP CEP 04013-000,
BRASIL
TEL: [55]-(0)11-3253-3331
FAX: [55]-(0)11-3586-0138

< Europe >

SHIBAURA MACHINE EUROPE S.R.L.

Via Gaudenzio Fantoli 7, Piano 2, 20138,
Milano, ITALIA
TEL: [39]-02-50041667
FAX: [39]-02-50041668

Shibaura Machine

2-2, Uchisaiwaicho 2-chome, Chiyoda-ku, Tokyo 100-8503, Japan
TEL : [81]-(0)3-3509-0200 FAX : [81]-(0)3-3509-0333

2068-3, Ooka, Numazu-shi, Shizuoka-ken 410-8510, Japan
TEL : [81]-(0)55-926-5141 FAX : [81]-(0)55-925-6501

<https://www.shibaura-machine.co.jp/>



This <Shibaura Machine Engineering Review> is made of LIMEX, a new material made mainly from limestone.
It uses less water and trees.

SM23005-800-TP